THESIS

Development of a 3-meter Fabry-Perot-Michelson Interferometer for Gravitational Wave Detection

Keita KAWABE

Submitted 1998

Contents

The following is a partial list of the symbols used in this paper.

c	=	the speed of light in vacuum
i	=	$\sqrt{-1}$
L	=	the length of a linear optical cavity
l	=	the length between the beam splitter and the mirror
ν, Ω	=	the frequency and the angular frequency of the light, respectively (typically on the order of 10^{14} Hz)
f, ω	=	the frequency and the angular frequency of the audio sidebands, respectively (also used for the RF sidebands)
ϕ, Φ, θ, Θ, ψ, Ψ	=	the phase

Tilde is used to represent either the Fourier transform or the power-spectral-density (PSD) of a time-domain function.

1. Introduction

Gravitational waves are the wave solutions of Einstein's equations under the weak gravitational field. In the long term study of a binary pulsar system which Hulse and Taylor have discovered in 1975 [1], the orbital decay of the binary system has been observed, which has been proved to be in excellent agreement with the general relativistic prediction for the energy losses originating due to the radiation of the gravitational wave [2–5]. The energy carried by gravitational waves is so small that they become detectable only if generated by the large acceleration of the compact objects with the huge masses which can only be observed in astronomical phenomena; the coalescence of various types of binary systems, the asymmetric bursts from supernovae, the pulsars with high eccentricity, and so on. If the waveform of the gravitational waves from such objects are measured, we can not only verify the validity of general relativity but also extract information about the source which is complementary to the knowledge from the optical and radio measurements (see Ref. 6 and references therein). Therefore, though the gravitational wave has not been detected directly so far, it is important to develop the gravitational wave detectors which can be used as the new device for the astronomy.

In the pursuit of the detection of gravitational waves, several kinds of detectors have been studied and developed. Among them, the idea to use a Michelson laser interferometer as the gravitational wave detector originated in 1970's [7, 8]. The wide-band nature of the Michelson interferometer makes it suitable for the extraction of the waveform. The laser technology of today allows us to realize extremely sensitive strain meters by using laser interferometry. In fact, it is believed that the "real" detectors are within the reach of the modern optical and mechanical technologies at present. Several interferometers for gravitational-wave detection are now under construction around the

Group	Site	Scale	Type
LIGO (USA)	Washington, Louisiana	4 km	Power-recycled Fabry-Perot
VIRGO (Italy, France)	Pisa	3 km	Power-recycled Fabry-Perot
GEO (Germany, UK)	Hanover	600 m	Dual-recycled Michelson
TAMA (Japan)	Tokyo	300 m	Power-recycled Fabry-Perot

Table 1.1: *Brief summary of the interferometric gravitational wave detectors which are now being built. The interferometer "types" are described in Chap. 4.*

Sources	Wave form	Amplitude	Frequency (Hz)
NS-NS coalescence (200 Mpc)	Chirp	$10^{-22} \sim 10^{-21}$	10∼1000
BH-BH coalescence (200 Mpc)	Chirp	10^{-21}	10∼1000
SN explosion (15 Mpc)	Burst	10^{-21}	<1000
SN explosion (Our Galaxy)	Burst	10^{-19}	<1000
Pulsar (1 kpc)	Continuous	10^{-25}	1∼500
BH-MACHO coalescence (20 Mpc)	Chirp	10^{-21}	10∼100

Table 1.2: *The possible high-frequency sources of the gravitational waves [6, 15].*

world, which are summarized in Table 1.1 briefly [9 – 14]. Because there is a limitation on the scale of the ground-based system, these detectors will have optimal sensitivity at relatively high frequency like 100 Hz. In fact all of these detectors will aim at the sources in the frequency range from 10 to 1000 Hz, approximately.

Table 1.2 shows the possible "high-frequency" gravitational wave sources and their expected wave amplitude [6, 15]. The amplitude of the gravitational wave is represented by the dimension-less parameter h, which is a strain of the metric of space-time. Because of the extremely small amplitude as shown in Table 1.2, the interferometric detector has to be free from any noise sources; thermally– and seismically–excited vibration of the mirrors of the interferometer, noise of the readout and control electronics, noise of the laser source such as amplitude– and phase–fluctuation etc.

Michelson-based interferometers have a great property of being insensitive to the common-mode noise to their two orthogonal optical paths (often called "arms"), especially to the phase noise (or frequency noise) of the laser source[1]. However, any asymmetry in the real interferometer will make it sensitive to common-mode noise, therefore it is really important to stabilize the frequency of the laser. The sensitivity of the interferometer to common-mode noise is expressed by the parameter called Common-Mode-Rejection Ratio (CMRR). CMRR is a function of asymmetry of the interferometer. Any asymmetry in the system, introduced intentionally or not, will make CMRR worse; on-axis, non-geometrical asymmetry such as difference of the reflectance of the mirrors in the two arms, geometrical asymmetry such as misalignment of the mirrors, and the asymmetry of the control system, for example. Because the requirement for the frequency stabilization of the laser, which depends upon the aimed strain sensitivity and CMRR, is crucial, it is necessary to study the relation between the CMRR and many asymmetries in the interferometer, and to investigate the realistic value of CMRR that is feasible using the current technology, theoretically and experimentally.

For this purpose, a 3m Fabry-Perot-Michelson (FPM) interferometer was built in the campus of The University of Tokyo. The optical components of the interferometer are suspended independently as in the real interferometric detectors. All of the major noise sources have been identified, and the displacement noise level of the interferometer reached $2 \times 10^{-17}\,\mathrm{m}/\sqrt{\mathrm{Hz}}$ at 1 kHz and $1 \times 10^{-17}\,\mathrm{m}/\sqrt{\mathrm{Hz}}$ at the noise floor between 2 kHz and 10 kHz. The floor noise was identified as the shot noise of the light. This was the first demonstration of the all-suspended FPM interferometer [16]. The basic parameters such as the reflectance of the mirrors, finesse of the cavities and so on were measured to estimate the non-geometrical asymmetry. The CMRR of the interferometer was demonstrated to be 1/300 at its best, and the consistency of this value with the measured asymmetry of the interferometer was verified. Also the relation between CMRR and the misalignment of the mirrors was demonstrated.

In this paper, some basics about the gravitational wave and the interferometry are calculated in Chap. 2-6. Because it is necessary to analyze the off-axis asymmetry, the mode-picture is presented in Chap. 5. Using the calculations in the preceding chapters, CMRR of the FPM interferometer is studied in detail in Chap. 7. In Chap. 8,

[1]See Chap. 2 and 3.

the development of the 3-m FPM is described. The control scheme, noise analysis, frequency-stabilization and CMRR analysis, and the demonstrated displacement sensitivity of the interferometer will be discussed. Also some discussions on the full-scale interferometers will be presented in this paper.

2. Gravitational Radiation

In this chapter, the Greek subscripts and superscripts (α, β, μ, *etc.*) represent the space-time coordinates, *i.e.* $0 \cdots 3$, while the Latin (i, j, *etc.*) represent the space-coordinates only. Time coordinate x^0 is defined by $x^0 = c\,t$, where c is the speed of light.

2.1 Linearized Theory

When the gravitational field is weak[1], the geometry is represented by the sum of the metric of the background Minkowski space-time and the small perturbation $h_{\mu\nu}$;

$$g_{\mu\nu} = \eta_{\mu\nu} + h_{\mu\nu} \tag{2.1}$$

$$\eta_{\alpha\beta} \equiv \begin{pmatrix} -1 & 0 & 0 & 0 \\ 0 & 1 & 0 & 0 \\ 0 & 0 & 1 & 0 \\ 0 & 0 & 0 & 1 \end{pmatrix} \tag{2.2}$$

$$|h_{\mu\nu}| \ll 1. \tag{2.3}$$

The Riemann tensor, the Ricci tensor, and the Riemann curvature of the space-time can be expanded to the first order of $h_{\mu\nu}$ as

$$R_{\alpha\beta\mu\nu} = \frac{1}{2}\left(h_{\alpha\nu,\beta\mu} + h_{\beta\mu,\alpha\nu} - h_{\alpha\mu,\beta\nu} - h_{\beta\nu,\alpha\mu}\right) \tag{2.4}$$

$$R_{\mu\nu} = R^{\alpha}{}_{\mu\alpha\nu} \tag{2.5}$$

$$R = R^{\alpha}{}_{\alpha}. \tag{2.6}$$

The trace reverse tensor of $h_{\mu\nu}$, which is represented by $\bar{h}_{\mu\nu}$, is defined as

$$\bar{h}^{\mu\nu} \equiv h^{\mu\nu} - \frac{1}{2}\eta^{\mu\nu} h \tag{2.7}$$

[1] See textbooks and reviews such as references [17– 21] for a fuller discussion.

$$h \equiv h^{\mu}{}_{\mu} \tag{2.8}$$

or,

$$h^{\alpha\beta} \equiv \bar{h}^{\alpha\beta} - \frac{1}{2}\eta^{\alpha\beta}\bar{h} \tag{2.9}$$
$$\bar{h} \equiv \bar{h}^{\mu}{}_{\mu}. \tag{2.10}$$

The Einstein tensor is written as

$$\begin{aligned} G_{\alpha\beta} &\equiv R_{\alpha\beta} - \frac{1}{2}g_{\alpha\beta}R \\ &= -\frac{1}{2}\left(\bar{h}_{\alpha\beta,\mu}{}^{,\mu} + \eta_{\alpha\beta}\bar{h}_{\mu\nu}{}^{,\mu\nu} - \bar{h}_{\alpha\mu,\beta}{}^{,\mu} - \bar{h}_{\beta\mu,\alpha}{}^{,\mu}\right). \end{aligned} \tag{2.11}$$

To simplify the above equation, we require the Lorentz gauge condition

$$\bar{h}^{\mu\nu}{}_{,\nu} = 0. \tag{2.12}$$

In this gauge, the expression for the Einstein tensor is simplified considerably as

$$\begin{aligned} G_{\alpha\beta} &= -\frac{1}{2}\bar{h}_{\alpha\beta,\mu}{}^{,\mu} \\ &= -\frac{1}{2}\Box\bar{h}_{\alpha\beta} \end{aligned} \tag{2.13}$$

where the symbol $\Box$ represents the D'Alembertian operator

$$\Box = -\frac{\partial^2}{c^2\partial t^2} + \triangle\,. \tag{2.14}$$

Thus the Einstein equations of the fields take the simple form in the Lorentz gauge:

$$\Box\bar{h}_{\mu\nu} = -\frac{16\pi G}{c^4}T_{\mu\nu} \tag{2.15}$$

where G is the gravitational constant.

2.2 Gravitational Wave

In vacuum, the weak field Einstein equations reduce to the wave equations,

$$\Box\bar{h}_{\mu\nu} = 0. \tag{2.16}$$

Any solutions to these equations are expressed as the linear combinations of the plane-wave solutions;

$$\bar{h}_{\alpha\beta} = A_{\alpha\beta} \exp(ik_\mu x^\mu), \tag{2.17}$$

where the wave number and the amplitude must satisfy the equations

$$\begin{aligned} k_\alpha k^\alpha &= 0 &(2.18)\\ A^{\alpha\beta} k_\beta &= 0. &(2.19)\end{aligned}$$

Equation 2.19 is derived from the Lorentz gauge condition.

We can use another gauge freedom to impose the conditions,

$$\begin{aligned} A^\alpha{}_\alpha &= 0 &(2.20)\\ A_{\alpha\beta} U^\beta &= 0, &(2.21)\end{aligned}$$

where U^β is an arbitrary time-like unit vector. The above conditions are called the transverse-traceless (TT) gauge conditions. In the TT gauge, the trace reverse tensor $\bar{h}^{\mu\nu}$ is equal to the perturbation of metric tensor $h^{\mu\nu}$ because the trace is equal to zero ($\bar{h}^\mu_\mu = h^\mu_\mu = 0$);

$$\bar{h}_{\alpha\beta} = h_{\alpha\beta}. \tag{2.22}$$

We choose U^β as the time-basis of the background Minkowski space-time. When the space part of the wave number vector k_i is parallel to the z axis (the wave is propagating parallel to the z axis), the perturbation tensor is represented by

$$\begin{aligned} h_{\alpha\beta} &= A_{\alpha\beta} \exp i\omega(t-z) &(2.23)\\ A_{\alpha\beta} &= \begin{pmatrix} 0 & 0 & 0 & 0 \\ 0 & A_+ & A_\times & 0 \\ 0 & A_\times & -A_+ & 0 \\ 0 & 0 & 0 & 0 \end{pmatrix}, &(2.24)\end{aligned}$$

where ω is the angular frequency of the gravitational wave. There are two degrees of freedom, A_+ and $A_\times$. When $A_\times$ is equal to zero, the wave is called plus-polarized, while the wave with $A_+ = 0$ is called cross-polarized in this coordinate system.

Two gravitational waves, which are represented by $h_{\mu\nu}$ and $h'_{\mu\nu}$ and are propagating together, have orthogonal polarization to each other if the metric perturbation satisfies the following equation:

$$h^*_{\mu\nu} h'^{\mu\nu} = 0 \tag{2.25}$$

where h^* indicates the complex conjugate of h. If the ratio of A_+ and $A_\times$ is real, $h_{\mu\nu}(t, z)$ is orthogonalized in a new coordinate system (t, x', y', z) by a simple space-part rotation with the z axis as the center of rotation. Such kind of waves are called linearly polarized. Plus- and cross-polarized waves are examples of the linearly polarized waves which are orthogonal to each other. On the other hand, if A_+ and $A_\times$ satisfy the equation

$$A_+ = \pm i A_\times, \tag{2.26}$$

the wave is called circularly polarized. It is easy to show that circularly polarized waves with opposite signs ($A_+ = iA_\times$ and $A_+ = -iA_\times$) are orthogonal to each other. It is impossible to orthogonalize $h_{\mu\nu}(t, z)$ by a simple space rotation. In general, however, it is still possible to find a new coordinate system $[t, x'(t, z), y'(t, z), z]$ in which $h_{\mu\nu}(t, z)$ is orthogonalized at specific values t and z, by a simple space rotation with the z axis as the center of rotation. A set of new axes $x'(t, z)$ and $y'(t, z)$ for all values of t and z form two surfaces which we call "polarization surfaces" in this paper. In the linearly polarized wave, the polarization surfaces are the two planes which are orthogonal to each other, and we call these the "polarization planes". The polarization planes for the plus- and cross-polarization form an angle of $\pi/4$. In the circularly polarized wave, the surfaces are two helicoidal surfaces that are propagating along the z axis with the wave. The period of the helicoid is equal to that of the gravitational wave. The polarization surface of the two orthogonal circularly polarized waves have the same period, but the rotation directions of the helicoids are opposite (Fig. 2.1).

A more general expression for the wave which is propagating along the z axis is

$$h_{\alpha\beta}(t, z) = \begin{pmatrix} 0 & 0 & 0 & 0 \\ 0 & h_+ & h_\times & 0 \\ 0 & h_\times & -h_+ & 0 \\ 0 & 0 & 0 & 0 \end{pmatrix}. \tag{2.27}$$

Fourier-transform of the wave represented by $\tilde{h}_s$ $(s = +, \times)$ is defined as

$$h_s(t - z) = \int \tilde{h}_s(\omega) e^{i\omega(t-z)} d\omega \quad (s = +, \times) \tag{2.28}$$

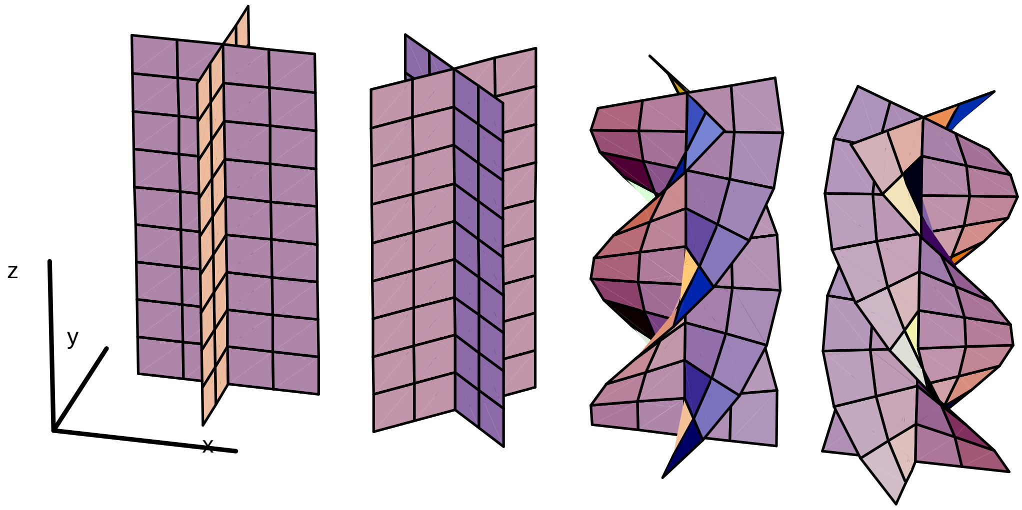

Figure 2.1: *Three-dimensional plot of the "polarization surface" for the linear polarization (left two) and the circular polarization (right two) of the gravitational wave. For the linearly polarized wave, the surfaces are the two orthogonal planes in which the propagation vector lies. For the circularly polarized wave, the surfaces are the two helicoidal surfaces which propagates together with the wave.*

where ω is the angular frequency of the wave.

2.3 Free Particle in the Field of the Gravitational Wave

A "free particle" is a particle free from any forces except for the gravity. Its world-line is determined by the equation of the geodesic,

$$\frac{d}{d\tau}U^{\alpha} + \Gamma^{\alpha}_{\mu\nu}U^{\mu}U^{\nu} = 0, \tag{2.29}$$

where τ and U^{α} represent the proper time and the four-vector of the particle, and $\Gamma^{\alpha}_{\mu\nu}$ represents the Christoffel symbols. We will neglect the gravitational field which is generated by the particle itself, therefore the particle can be used as a probe of the gravitational field. In this sense, the particle is often referred to as the "test" mass.

Suppose that a test mass is in the field of the gravitational wave that is represented by Eqs. 2.27 and 2.28. For simplicity we assume that there is only a "plus" polarization of the gravitational wave field and $h_{\times} = 0$. Since all of the time-time and time-space components of the metric perturbation $h_{0\beta}$ in this field are equal to zero, all of $\Gamma`\mu_{00}$ vanish:

$$\Gamma^{\mu}_{00} = \frac{1}{2}\eta^{\mu\beta}(h_{\beta 0,0} + h_{0\beta,0} - h_{00,\beta}) = 0. \tag{2.30}$$

Thus it is apparent that the time-basis vector

$$\{U^{\alpha}\} = (1, 0, 0, 0) \tag{2.31}$$

satisfies Eq. 2.29. Therefore we can say that a test mass which is initially at rest in the TT coordinate system will be at rest even in the gravitational waves. However, this does not mean that the gravitational wave has no effect on the free particles, because the coordinate itself has no physical meaning. The physical effect of the gravitational wave on the free particles is calculated below.

Suppose that there are two test masses, one at the origin and the other at

$$r_0(\cos\phi, \sin\phi, 0) \equiv r_0(n_x, n_y, n_z) \tag{2.32}$$

in the TT coordinate, where n_i is the constant unit three-vector in the xy plane and r_0 is the distance between the two particles when the space-time is flat. A photon is emitted from the test mass at the origin at the coordinate time t_0. When the photon reaches the other test mass at the coordinate time t_1, it is reflected and returns back to the origin at the coordinate time t_2. The round-trip time of the photon is defined by the difference of the coordinate time, $\Delta t = t_2 - t_0$. Since the test mass is at rest at the origin in this coordinate system, Δt is interpreted as the proper time between the emission and the capture of the photon.

When there is no gravitational radiation, it is apparent that Δt is equal to $2r_0/c$. We define any deviation of Δt from $2r_0/c$ as δt:

$$\delta t \equiv \Delta t - 2r_0/c = O(h). \tag{2.33}$$

where $O(h)$ indicates the first or higher order term(s) of h. Also, the coordinate time t_0 and t_1 are represented by

$$\begin{aligned} t_0 &= t_2 - 2r_0/c + O(h) \quad &(2.34)\\ t_1 &= t_2 - r_0/c + O(h). \quad &(2.35) \end{aligned}$$

The world line of the photon is parametrized by the coordinate time t. The trajectory of the photon is described as

$$x_i(t) = n_i r(t), \tag{2.36}$$

where $r = (x_i x^i)^{1/2}$ is the radial coordinate in TT coordinate system[2]. Under the field of the gravitational wave, $r(t)$ is given by

$$r(t) = \begin{cases} c\,(t - t_0) + O(h) & (t < t_1) \\ c\,(t_2 - t) + O(h) & (t > t_1) \end{cases}, \tag{2.37}$$

where $O(h)$ expresses the first or higher terms of h. The line element along the world line of the photon is calculated as

$$ds^2 = -c^2 dt^2 + (1 + h_+(t,0)\cos 2\phi)\, dr^2 = 0, \tag{2.38}$$

[2]A deviation (if any) of the first order of the gravitational wave field h from Eq. 2.36 produces a second order perturbation in the line element. Therefore such a deviation can be neglected within the first order approximation.

therefore

$$|dr| \simeq \left(1 - \frac{1}{2}h_+(t,0)\cos 2\phi\right) c\,dt. \tag{2.39}$$

Integrating the above equation along the world line of the photon, we obtain the expression

$$\begin{aligned} 2r_0 &= \left[\int_{t_0}^{t_1} + \int_{t_1}^{t_2}\right]\left[1 - \frac{1}{2}\cos 2\phi\, h_+(t,0)\right] c\,dt \\ &= c\,\Delta t - \frac{1}{2}\cos 2\phi \int_{t_0}^{t_2} h_+(t,0)c\,dt \end{aligned} \tag{2.40}$$

thus the expression for δt is written as

$$\delta t = \frac{1}{2}\cos 2\phi \int_{t_0}^{t_2} h_+(t,0)dt. \tag{2.41}$$

By using Eqs. 2.34 and 2.41, δt is written as

$$\delta t = \frac{1}{2}\cos 2\phi \int_{t_2-2r_0/c+O(h)}^{t_2} h_+(t,0)dt. \tag{2.42}$$

The first order term of h which is represented by $O(h)$ in the above equation produce the second order perturbations in δt, thus can be neglected within the first order approximation:

$$\begin{aligned} \delta t &= \frac{1}{2}\cos 2\phi \int_{t_2-2r_0/c}^{t_2} h_+(t,0)dt \\ &= \cos 2\phi \int_{-\infty}^{\infty} \tilde{h}_+(\omega)e^{i\omega(t_2-r_0/c)}\frac{\sin(\omega r_0/c)}{\omega}d\omega\,. \end{aligned} \tag{2.43}$$

One can see that the round-trip time of the photon has a small modulation which is proportional to the amplitude of the gravitational wave. This can be interpreted in two ways: The speed of light (or the absolute refractive index of vacuum) is constant and the distance between the masses changes, or the distance is constant and the speed of light changes[3]. For the plus-polarized wave with the frequency fixed, the amplitude of the modulation is maximized with the opposite signs on the xz and the yz planes;

$$\phi = \begin{cases} n\pi \\ (2n+1)\pi/2 \end{cases} \tag{2.44}$$

[3] In this paper, we will take the interpretation in which the speed of light is constant. However, the choice of the interpretation will not affect the observation of the phenomena.

where n is an integer. Therefore, we can say that the cross section of the polarization surface and the wave front (the plane in which the phase of the wave is constant) indicates “the direction of maximum modulation”. For the cross polarization, the angle ϕ is replaced by $\phi + \pi/4$ (Fig. 2.2). In general, for any linearly polarized gravitational wave that is represented by

$$h_{\mu\nu}(t,z) = h(t-z)\begin{pmatrix} 0 & 0 & 0 & 0 \\ 0 & \cos 2\phi_0 & \sin 2\phi_0 & 0 \\ 0 & \sin 2\phi_0 & -\cos 2\phi_0 & 0 \\ 0 & 0 & 0 & 0 \end{pmatrix}, \tag{2.45}$$

ϕ can be replaced by $\phi - \phi_0$ that represents the angle between one of the polarization planes and the vector that connects the two test masses. The fact that the amplitude of the strain in space has a $\cos 2(\phi - \phi_0)$ dependence reflects the quadrupole nature of the gravitational wave.

To summarize, in the TT coordinate system, free particles which are initially at rest will be at rest, even in the gravitational radiation field. However, the round-trip time of the photon between two free particles is modulated with the amplitude proportional to that of the gravitational wave. If we assume that the speed of light is constant, the modulation is interpreted as the change in the distance. The amplitude of the variation of the distance is proportional to the mean proper distance r_0. The frequency and the polarization of the wave also affect the amplitude of the variation.

2.3.1 Gravitational Wave Detection by the Round-Trip Time Measurement

It has been shown that the round-trip time of the photon between two free particles is modulated with the amplitude proportional to that of the gravitational wave. Therefore, the free particles can be used as a gravitational wave detector. The simplest form of such a detector is shown in Fig. 2.3. There are two free masses in the field of the gravitational wave. Photons are emitted from the observer on the test mass at the origin, and reflected by the other mass. The observer records the round-trip time of the photon repeatedly. When there are no gravitational waves, the observer will always

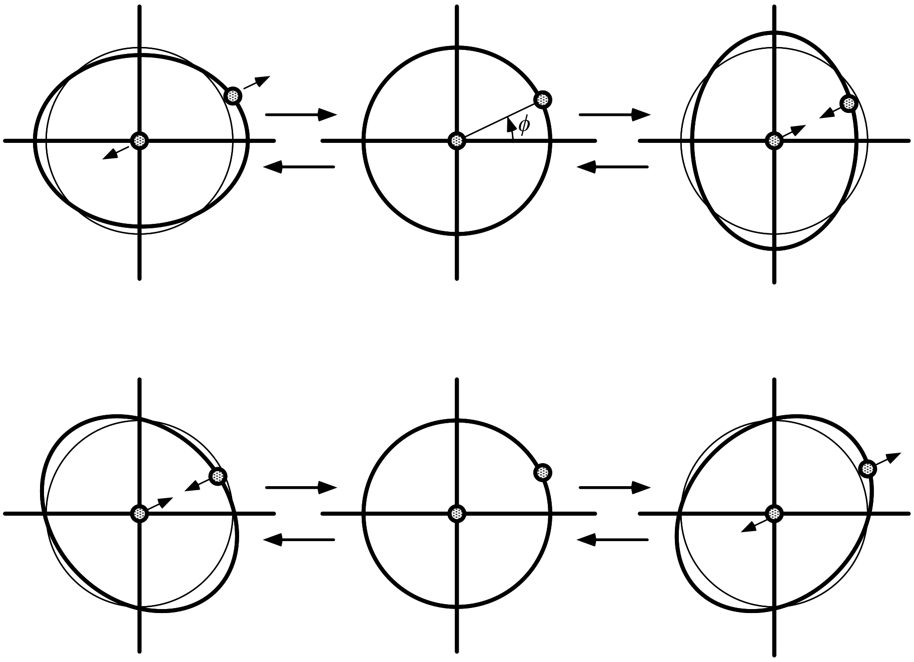

Figure 2.2: *When the gravitational wave passes the two free particles, the proper distance between them varies. These plots show how the distance between two masses is modulated by the linearly polarized gravitational wave that propagates perpendicular to the plane of the figure. In the upper plots, the wave has a plus-polarization, thus the distance has a* $\cos 2\phi$ *dependence. In the lower plots, the wave has a cross-polarization, thus the distance has a* $\cos 2(\phi + \pi/4)$ *dependence.*

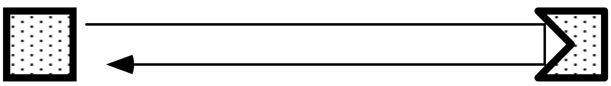

Figure 2.3: *The concept of the two free masses and an observer as a gravitational wave detector. Photons are emitted from the observer and reflected by the other mass. The observer measures the round-trip time by using a clock. The measurements are made repeatedly.*

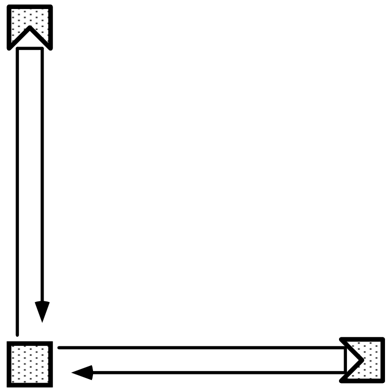

Figure 2.4: *The idea of the differential measurement. Photons are emitted from the apex in two different directions. When there is no gravitational wave passing, the photons in the two paths return to the observer at the same time, thus no pseudo-signal will be generated by a deviation of the clock from the coordinate time.*

obtain the same constant $(2r_0/c)$ as the results of the measurements. Therefore the observer interprets any change in the round-trip time as the effect of the gravitational wave.

Suppose that the clock is not "accurate", *i.e.*, the clock has a deviation from the coordinate time. The round-trip time measured by the observer will have a variation due to the deviation of the clock's time, even if no gravitational wave is passing. The observer cannot distinguish the deviation of the clock's time from the fluctuation of the distance caused by the gravitational wave, therefore the stability of the clock directly determines the accuracy of the measurement.

Differential Detection

The requirement for the stability of the clock can be relaxed, if the observer measures the distance between the masses in two directions simultaneously. Figure 2.4 shows the idea. Three free masses are aligned in an isosceles L-shape. On the "apex" of this L-shape, the observer sends photons to the other two test masses, then the photons are reflected back to the observer. The observer measures the difference of the round-trip time in two orthogonal directions. Any appropriately polarized gravitational wave causes a difference in round trip time in the two directions, which appears as the signal in the measurement. If the wave propagates perpendicular to the plane on which the detector lies[4], and if the two sides of the detector lie on the polarization surfaces, then the changes in the round-trip time have the same amplitude with opposite signs due to the quadrupole nature of the gravitational wave. Therefore the amplitude of the signal is two times larger than that of the two-masses detector. If there is no gravitational wave passing through the detector, the photons from the two directions always reach the observer at the same time. Therefore the observer will obtain no signal even if the clock has a deviation, or an "error", from the coordinate time; thus the signal-to-noise ratio of the detector is considerably better, compared with the detector which measures the round-trip time directly. Michelson interferometers are the optical realization of such a kind of differential detectors.

Let us calculate the angular response of the differential detector to the gravitational waves. At first, for convenience, we choose the coordinate system (x, y, z) in which the masses of the detector are fixed at $(0, 0, 0)$, $(r_0, 0, 0)$, and $(0, r_0, 0)$. The orientation of the linearly polarized gravitational wave is expressed in the spherical coordinates (θ, ϕ). The polarization angle ϕ_0 is defined as the angle between one of the polarization planes and the plane that the z axis and the wave vector forms (Fig. 2.5).

Another coordinate system (x', y', z') is obtained by the three rotations on the original coordinate system; ϕ around the z axis, θ around the y axis, and ϕ_0 around the new z axis. In this coordinate system, it is apparent that the metric perturbation of the gravitational wave is orthogonalized and expressed by Eq. 2.27 with $h_\times = 0$. The observer is still at the origin, but the other two masses are located at

$$r_0\overrightarrow{n_1} = r_0 \begin{pmatrix} \cos\theta\cos\phi\cos\phi_0 - \sin\phi\sin\phi_0 \\ -\cos\theta\cos\phi\sin\phi_0 - \sin\phi\cos\phi_0 \\ \sin\theta\cos\phi \end{pmatrix} \tag{2.46}$$

$$r_0\overrightarrow{n_2} = r_0 \begin{pmatrix} \cos\theta\sin\phi\cos\phi_0 + \cos\phi\sin\phi_0 \\ -\cos\theta\sin\phi\sin\phi_0 + \cos\phi\cos\phi_0 \\ \sin\theta\sin\phi \end{pmatrix} \tag{2.47}$$

[4] We call this plane the detector's plane.

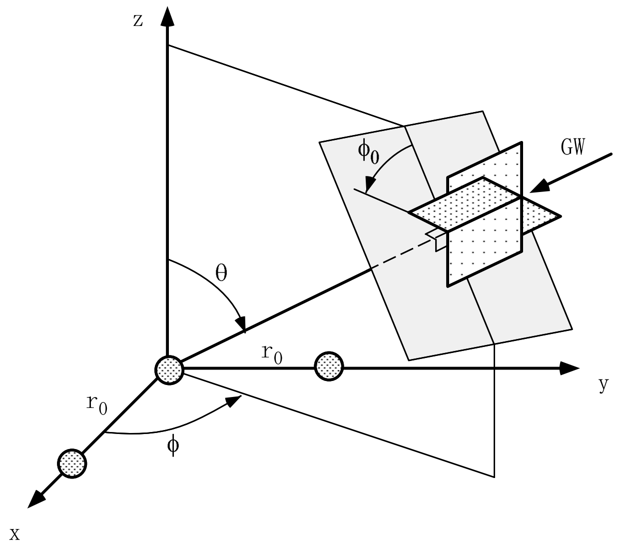

Figure 2.5: *The definitions of the propagation direction and the polarization angle of the gravitational wave. In this figure, the detector is fixed.*

in this (x', y', z') coordinate system. The delay for each path is calculated as

$$\delta t_1(t) = r_0 \left[\cos 2\phi_0(\cos^2\theta\cos^2\phi - \sin^2\phi) - \cos\theta\sin 2\phi\sin 2\phi_0\right] h_+ \quad (2.48)$$

$$\delta t_2(t) = r_0 \left[\cos 2\phi_0(\cos^2\theta\sin^2\phi - \cos^2\phi) + \cos\theta\sin 2\phi\sin 2\phi_0\right] h_+ \quad (2.49)$$

in the low-frequency limit. The signal observed is the difference of the variation of the round-trip time:

$$\delta t_1 - \delta t_2 = -\left[\cos 2\phi_0\cos 2\phi(1+\cos^2\theta) + 2\sin 2\phi_0\sin 2\phi\cos\theta\right] h_+ \quad (2.50)$$

The detector is insensitive to the wave from the following direction, no matter how the polarization of the wave is chosen:

$$(\theta, \phi) = [\pi/2, (2n+1)\pi/4] \quad (2.51)$$

where n is an arbitrary integer. With the propagation direction (θ, ϕ) fixed, the signal takes its maximum

$$|\delta t_1 - \delta t_2|_{\max} = \left\{[\cos 2\phi(1+\cos^2\theta)]^2 + (2\sin 2\phi\cos\theta)^2\right\}^{1/2} h_+ \quad (2.52)$$

when ϕ_0 satisfies the equation

$$\tan 2\phi_0 = \frac{2\sin 2\phi\cos\theta}{\cos 2\phi(1+\cos^2\theta)}. \quad (2.53)$$

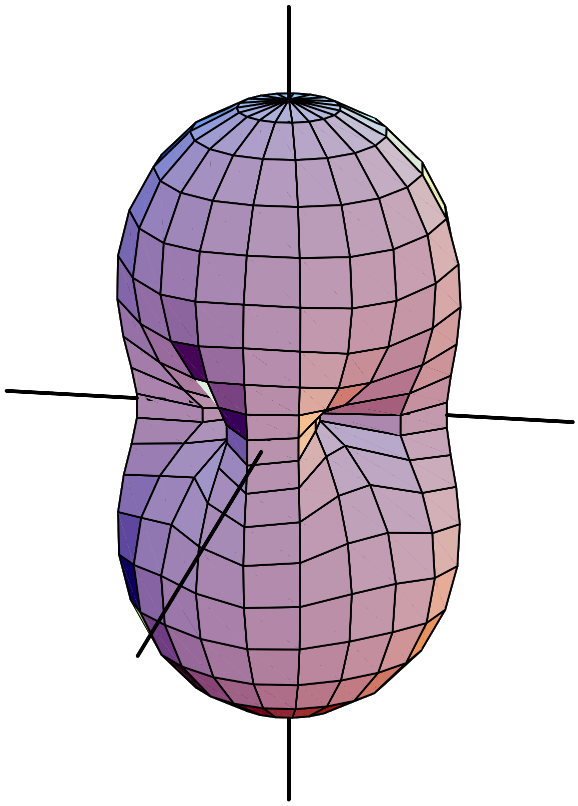

Figure 2.6: *A spherical plot of the angular response of the differential detector when the frequency of the wave is very small ($\omega r_0 << 1$). The polarization of the gravitational wave is chosen to maximize the response.*

Also, the amplitude of the signal is equal to zero when the polarization angle is offset by $\pi/4$ from the above condition, it i.e. for:

$$\tan 2\phi_0 = -\frac{\cos 2\phi(1+\cos^2\theta)}{2\sin 2\phi\cos\theta}. \tag{2.54}$$

Figure 2.6 shows the absolute value of the amplitude of the signal normalized by the amplitude of the wave.

3. Michelson Interferometer

The Michelson interferometer is the simplest differential gravitational wave detector. All of the interferometric gravitational wave detectors are based on the Michelson interferometer, which has been pioneered by Weiss [7] and Forward [8]. As discussed in the previous chapter, a differential detector is insensitive to the inaccuracy of the clock. This is interpreted as the rejection of the common mode noise, especially the frequency noise, in Michelson interferometers.

3.1 Basic Assumptions

Before discussing the interferometers, we must clarify some assumptions and definitions of some quantities that will appear throughout this paper.

3.1.1 Electromagnetic Wave

A general expression for the electric and magnetic field of the light in vacuum is written as:

$$\overrightarrow{E}(t, \overrightarrow{r}) = \int \overrightarrow{\tilde{E}}(\Omega) \exp i\Omega \left[t - \overrightarrow{n}(\Omega) \cdot \overrightarrow{r}/c\right] d\Omega \tag{3.1}$$

$$\overrightarrow{B}(t, \overrightarrow{r}) = \int \overrightarrow{\tilde{B}}(\Omega) \exp i\Omega \left[t - \overrightarrow{n}(\Omega) \cdot \overrightarrow{r}/c\right] d\Omega \tag{3.2}$$

$$\overrightarrow{\tilde{B}}(\Omega) = \frac{1}{c} \overrightarrow{n}(\Omega) \times \overrightarrow{\tilde{E}}(\Omega) \tag{3.3}$$

where Ω is the angular frequency of light, $\overrightarrow{E}$, $\overrightarrow{B}$, $\overrightarrow{\tilde{E}}$, and $\overrightarrow{\tilde{B}}$ represent the electric and magnetic field and their Fourier transform, and $\overrightarrow{n}(\Omega)$ is a unit three-vector which describes the propagation direction. From Eq. 3.3, one can see that either of the electric and the magnetic field describes the electromagnetic wave completely, because one of the fields is calculated from the other. Therefore we will use only the electric field to express the electromagnetic wave. Also, we will neglect the polarization properties of the wave unless it is necessary, therefore the field is represented by the amplitude.

In this paper, the complex amplitude will always be used for the expressions of the electromagnetic fields. For example, consider a monochromatic field which is written as

$$E_{\mathrm{real}}(t) = E_0 \cos(\Omega t + \phi) \tag{3.4}$$

where E_0 and ϕ are the real numbers. In the complex amplitude representation, this is written as

$$E_{\mathrm{cmplx}}(t) = E_0 \exp i(\Omega t + \phi). \tag{3.5}$$

For the conversion from the complex to the real amplitude, simply take the real part of the complex amplitude:

$$E_{\mathrm{real}}(t) = \mathcal{R}e\left[E_{\mathrm{cmplx}}(t)\right]. \tag{3.6}$$

Poynting's vector is defined by

$$\overrightarrow{S}(t) \equiv \frac{1}{\mu_0} \overrightarrow{E}_{\mathrm{real}}(t) \times \overrightarrow{B}_{\mathrm{real}}(t) \tag{3.7}$$

where μ_0 is the magnetic permeability of vacuum. The absolute value of the Poynting's vector represents the flow of the electromagnetic energy per unit time per unit area perpendicular to the propagation direction. A simple calculation shows that the absolute value of the Poynting's vector is proportional to the square of the real amplitude of the electric field as

$$\begin{aligned} \left|\overrightarrow{S}(t)\right| &= \sqrt{\frac{\epsilon_0}{\mu_0}} E_{\mathrm{real}}^2(t) \\ &= \frac{1}{2}\sqrt{\frac{\epsilon_0}{\mu_0}} E_0^2 \left[1 + \cos 2(\Omega\, t + \phi)\right] \end{aligned} \tag{3.8}$$

where ϵ_0 is the dielectric constant of vacuum. The second harmonic term in the above equation, which is rapidly oscillating, has nothing to do with the net flow of energy. Therefore the power density (or the intensity) of the field is defined to represent the net energy-flow as

$$I(t) = \frac{1}{T}\int_t^{t+T} \sqrt{\frac{\epsilon_0}{\mu_0}} E_{\mathrm{real}}^2(t) dt \tag{3.9}$$

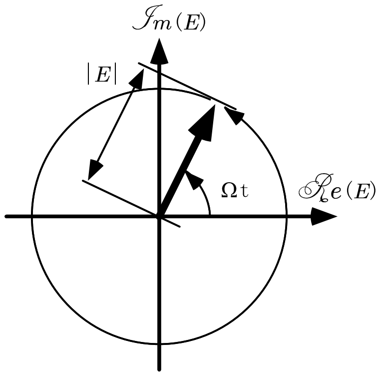

Figure 3.1: *The amplitude of a field is represented by a vector in a complex plane. For a sinusoidal wave with a fixed power, the vector rotates at the same angular frequency as the field.*

where T is a constant which is much larger than the inverse of the angular frequency of the field. In the complex amplitude expression, the integration procedure is not necessary because the absolute value of the complex amplitude does not contain the second harmonics term;

$$I(t) = \frac{1}{2}\sqrt{\frac{\epsilon_0}{\mu_0}}\,|E_{\text{cmplx}}(t)|^2\,. \tag{3.10}$$

In this paper, the factor $(\epsilon_0/\mu_o)^{1/2}/2$ for the intensity will always be omitted for convenience.

The power of a laser beam is defined as

$$P(t) = \int ds\, I(t) \tag{3.11}$$

where ds denotes the surface integration over an arbitrary plane perpendicular to the beam.

In the complex amplitude expression, the amplitude of the field is represented by a vector in a complex plane (Figure 3.1). One of the axes denotes the real part, and the other axis denotes the imaginary part, of the amplitude. The length and the polar angle of the vector represents the absolute value and the phase of the amplitude, respectively. Usually the vector is rotating rapidly with the same frequency as the field.

3.1.2 Interference of the Fields

Two fields which are represented by $E_1(t)$ and $E_2(t)$ interfere with each other if the amplitude of the sum of the fields is not equal to the sum of the amplitude of the respective fields:

$$|E_1(t) + E_2(t)|^2 \neq |E_1(t)|^2 + |E_2(t)|^2, \tag{3.12}$$

or in other words if

$$E_1(t)E_2^*(t) + E_1^*(t)E_2(t) \neq 0. \tag{3.13}$$

If the fields are represented by the vectors $\overrightarrow{E}_1(t)$ and $\overrightarrow{E}_2(t)$ in the complex plane, the above conditions are interpreted as

$$\overrightarrow{E}_1(t) \cdot \overrightarrow{E}_2(t) \neq 0 \tag{3.14}$$

where the 'dot' $(\cdot)$ denotes the inner product of the vectors. Thus, we can say that the fields do not interfere if the vectors are always orthogonal in the complex plot. For example, the two fields which are represented by

$$E_1(t) = E_0 e^{i\Omega t} \tag{3.15}$$

$$E_2(t) = iE_0 e^{i\Omega t} \tag{3.16}$$

do not interfere with each other.

The usual complex plot is inconvenient for seeing the relative phase between the fields, because the vectors are rotating rapidly. Therefore, to eliminate the rapid rotation of the vectors, we will fix the angle of one of the fields in the plot. In other words, we will choose a coordinate system of the complex plane that is rotating with one of the vectors (Fig. 3.2).

3.1.3 Mirror

Figure 3.3 shows a mirror which is illuminated by a beam of light whose field is expressed as E_i. The incident light is partially transmitted (E_t) and partially reflected (E_r). The reflection coefficient r_1 and the transmission coefficient t_1 of one side of the

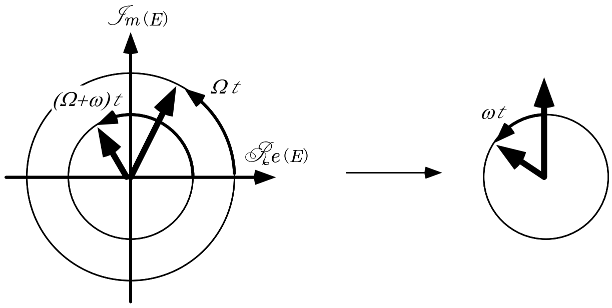

Figure 3.2: *In the complex plot, all of the vectors are rotating rapidly with the optical frequencies of the fields (left). In a relative phase plot (right), the polar angle of one of the vectors is fixed. The phase, or the rotation angle, of the vectors are measured by using the fixed vector as the reference.*

mirror (see the left side of Fig. 3.3) are defined as the ratios of the complex amplitude of the reflected and transmitted field to the incident field,

$$r_1 \equiv \frac{E_\mathrm{r}}{E_\mathrm{i}} \tag{3.17}$$

$$t_1 \equiv \frac{E_\mathrm{t}}{E_\mathrm{i}}\,. \tag{3.18}$$

The reflectance R_1 and the transmittance T_1 are defined as the ratios of the intensity,

$$R_1 \equiv |r_1|^2 = \left|\frac{E_\mathrm{r}}{E_\mathrm{i}}\right|^2 \tag{3.19}$$

$$T_1 \equiv |t_1|^2 = \left|\frac{E_\mathrm{t}}{E_\mathrm{i}}\right|^2\,. \tag{3.20}$$

For the other side of the mirror (see the right side of Fig. 3.3), another set of numbers r'_1, t'_1, R'_1, and T'_1 are defined in the same way.

The reflectance and the transmittance are positive numbers. Also, in this paper, reflection and transmission coefficients are chosen to be real[1]. They are represented by two positive numbers, r and t:

$$\begin{aligned} r_1 = & -r'_1 &= r, \\ t_1 = & \;\; t'_1 &= t. \end{aligned} \tag{3.21}$$

[1]Whether these coefficients are real or complex is a matter of definition: it depends on the definition of a reference plane where the phases of the fields are measured (for a fuller discussion, see Ref. 22).

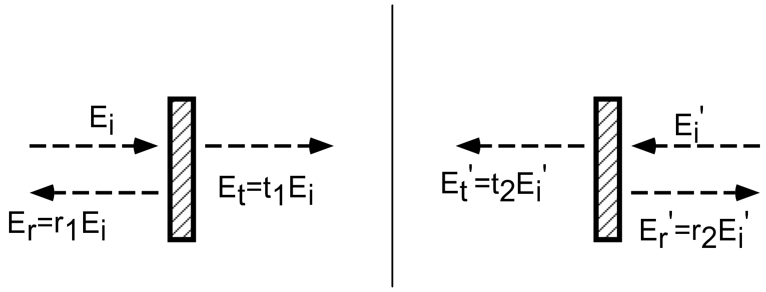

Figure 3.3: *A mirror is illuminated by an incident wave of light which is partially transmitted and partially reflected. As the two figures show, each side of the mirror has its own pair of reflection and transmission coefficients in general.*

For the reflection coefficient and the transmission coefficient of a simple mirror, we use the definition which is represented by the relations shown above. Note that the reflection coefficients of the two sides of a mirror then have opposite signs.

3.2 Michelson Interferometer

A Michelson interferometer comprises a beam splitter and two mirrors (Fig. 3.4). We define that the reflection coefficients of the mirrors represented by r_1 and r_2 have the same sign. The reflection coefficient of the beam splitter is positive on one side which faces Mirror 1 in the figure, and negative on the other side. We place the beam splitter, Mirror 1, and Mirror 2 on $(0, 0)$, $(l_1, 0)$, and $(0, l_2)$, respectively. The incident light, measured at the beam splitter, is expressed as

$$E_{\rm i}(t) = E_0 \exp(i\Omega t). \tag{3.22}$$

The delays of the phase of the field in the two paths are expressed as θ_1 and θ_2. We define the transmission of the interferometer as the field which is once reflected and once transmitted by the beam splitter. The reflection of the interferometer is defined as the field which is propagating toward the light source from the beam splitter. The fields of transmission and reflection are related to the difference of phase of light in two paths as

$$E_{\rm t} \;=\; E_0 t_{\rm b} r_{\rm b} \exp(i\Omega t)\Big[r_1 \exp(-i\theta_1) - r_2 \exp(-i\theta_2)\Big] \tag{3.23}$$

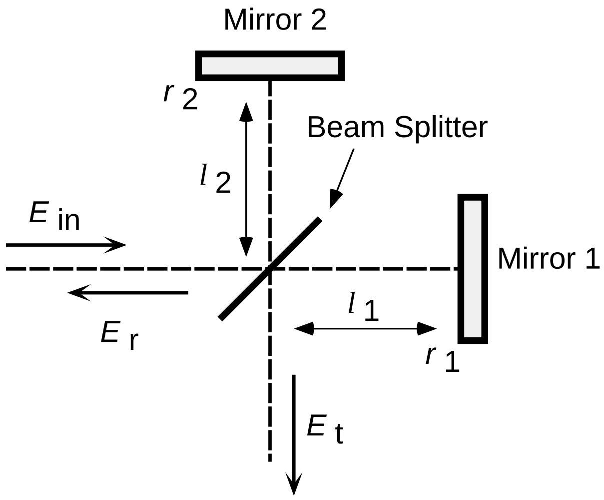

Figure 3.4: *A simple Michelson interferometer comprising a beam splitter and two mirrors. The divided beams are recombined on the beam splitter.*

$$E_{\mathrm{r}} = E_0 \exp(i\Omega t)\Big[T_{\mathrm{b}} r_1 \exp(-i\theta_1) + R_{\mathrm{b}} r_2 \exp(-i\theta_2)\Big], \tag{3.24}$$

where t_{b}, r_{b}, T_{b}, and R_{b} represent the transmission coefficient, the reflection coefficient, the transmittance, and the reflectance of the beam splitter. The intensity of the above fields are easily calculated as

$$\begin{aligned} I_{\mathrm{t}} &\equiv |E_{\mathrm{t}}|^2 \\ &= I_0 T_{\mathrm{b}} R_{\mathrm{b}} \left[R_1 + R_2 - 2 r_1 r_2 \cos\Delta\theta\right] \qquad (3.25) \\ I_{\mathrm{r}} &\equiv |E_{\mathrm{r}}|^2 \\ &= I_0 \left[T_{\mathrm{b}}^2 R_1 + R_{\mathrm{b}}^2 R_2 + 2 T_{\mathrm{b}} R_{\mathrm{b}} r_1 r_2 \cos\Delta\theta\right], \qquad (3.26) \end{aligned}$$

where I_0 is the intensity of the input beam and $\Delta\theta = \theta_1 - \theta_2$ is the difference of phase of the fields E_1 and E_2.

When the interferometer is symmetric, *i.e.* l_1 is equal to l_2 and r_1 is equal to r_2, most of the power of the input light is reflected; there is no transmission at all. Basically the transmission appears when there is any asymmetry. In this sense, the transmission and the reflection are sometimes called the anti-symmetric output and the symmetric output, respectively.

The contrast of a Michelson interferometer is given by

$$C \equiv \frac{I_{\max} - I_{\min}}{I_{\max} + I_{\min}} \tag{3.27}$$

$$= \frac{(r_1 + r_2)^2 - (r_1 - r_2)^2}{(r_1 + r_2)^2 + (r_1 - r_2)^2} \tag{3.28}$$

where $I_{\max}$ and $I_{\min}$ are the maximum and minimum intensity of the anti-symmetric output. The contrast is equal to unity when the optics of the interferometer is symmetric.

One can see that Michelson interferometers are insensitive to any common phase fluctuation in the two arms, because such a kind of phase fluctuation does not affect $\Delta\theta$. On the other hand, Michelson interferometers are sensitive to any differential phase fluctuation. As we have already seen, the gravitational wave modulates the proper distance between the free particles. If the mirrors and the beam splitter are the test masses, the gravitational wave which have a proper polarization will modulate the round-trip phase in the two arms with the same amplitude and the opposite signs, therefore the gravitational wave can be thought as a source of the differential phase modulator. In other words, Michelson interferometers are sensitive to the gravitational waves and thus can be used as a gravitational wave detectors. This idea was originally developed by Weiss [7] and first experimentally explored by Forward [8]. Later in this section we will calculate the frequency response of a simple Michelson interferometer, then more complex interferometer.

3.3 Frequency Response of a Michelson Interferometer

In this section the frequency response of a Michelson interferometer to the gravitational waves and to the motion of the mirrors are studied. In this and the following sections, the propagation direction and the polarization of the gravitational waves are chosen to maximize the response for convenience[2].

[2] One has be careful when one calculates the response to the wave from an arbitrary direction, because not only the sensitivity but the frequency dependence are affected by the propagation direction.

3.3.1 Frequency Response to the Gravitational Waves

We choose the coordinate system in which the metric has the form

$$ds^2 = -c^2 dt^2 + [1 + h(t)]dx^2 + [1 - h(t)]dy^2 + dz^2, \tag{3.29}$$

where $h(t)$ is the dimensionless amplitude of the wave. The field of the input light is given by Eq. 3.22 at the position of the beam splitter. The field of light which is reflected by Mirror 1 is written in the form

$$E_1 = t_{\mathrm{b}} E_0 \exp\Big[i\Omega(t - \Delta t_1)\Big] \tag{3.30}$$

where Ω is the optical frequency of light. We can use the same expression as Eq. 4.10 to obtain Δt_1. The delay of the phase $\Omega \Delta t_1$ is represented by two parts, the static delay $\theta_{\mathrm{o}1}$ and the phase shift caused by the gravitational wave $\delta\theta_1^{\mathrm{GR}}$:

$$\begin{aligned} \theta_1 &\equiv \Omega \Delta t_1 \\ &= \Omega \left(\frac{2l_1}{c} + \frac{1}{2} \int_{t-2l_1/c}^{t} h(t')dt' \right) \\ &\equiv \theta_{\mathrm{o}1} + \delta\theta_1^{\mathrm{GR}}. \end{aligned} \tag{3.31}$$

In other words, the phase of the field of light is modulated by the gravitational waves. In the same way, the field of light reflected by Mirror 2 is given by

$$E_2 = r_{\mathrm{b}} E_0 \exp\Big[i\Omega(t - \Delta t_2)\Big]. \tag{3.32}$$

However, the sign of the effect of the gravitational wave is opposite:

$$\begin{aligned} \theta_2 &\equiv \Omega \Delta t_2 \\ &= \Omega \left(\frac{2l_2}{c} - \frac{1}{2} \int_{t-2l_2/c}^{t} h(t')dt' \right) \\ &\equiv \theta_{\mathrm{o}2} + \delta\theta_2^{\mathrm{GR}}. \end{aligned} \tag{3.33}$$

The difference of the phase of the two fields E_1 and E_2 is expressed as

$$\begin{aligned} \Delta\theta &\equiv \theta_1 - \theta_2 \\ &= \theta_{\mathrm{o}1} - \theta_{\mathrm{o}2} + \delta\theta_1^{\mathrm{GR}} - \delta\theta_2^{\mathrm{GR}} \\ &\equiv \Delta\theta_{\mathrm{o}} + \delta\theta_{\mathrm{MI}}^{\mathrm{GR}} \\ &\equiv \Delta\theta_{\mathrm{o}} + \int \tilde{h}(\omega) H_{\mathrm{MI}}^{\mathrm{GR}}(\omega, \Omega) e^{i\omega t} d\omega, \end{aligned} \tag{3.34}$$

where $\Delta\theta_o$ is the static term and $\delta\theta_{\rm MI}^{\rm GR}$ is the fluctuation produced by the gravitational radiation. By observing the difference of the phase between two beams, the gravitational wave signal is extracted[3]. In the above expression, the frequency response of a Michelson interferometer to the gravitational radiation $H_{\rm MI}^{\rm GR}$ is defined as

$$\begin{aligned} H_{\rm MI}^{\rm GR}(\omega,\Omega) &\equiv \frac{\Omega}{\omega}\left(e^{-i\frac{\omega l_1}{c}}\sin\frac{\omega l_1}{c}+e^{-i\frac{\omega l_2}{c}}\sin\frac{\omega l_2}{c}\right) \\ &= 2\frac{\Omega}{\omega}e^{-i\frac{\omega\bar{l}}{c}}\left(\sin\frac{\omega\bar{l}}{c}\cos^2\frac{\omega l_-}{2c}-i\cos\frac{\omega\bar{l}}{c}\sin^2\frac{\omega l_-}{2c}\right) \\ &= 2\frac{\Omega}{\omega}e^{-i\frac{\omega\bar{l}}{c}}\sin\frac{\omega\bar{l}}{c}+O(\frac{\omega l_-}{2c})^2, \end{aligned} \tag{3.35}$$

where

$$\bar{l} = \frac{l_1+l_2}{2} \tag{3.36}$$

$$l_- = l_1-l_2 \tag{3.37}$$

are the average and the difference of the distance between the beam splitter and the mirrors. When the frequency of the light is thought to be a constant, we will sometimes write $H_{\rm MI}^{\rm GR}(\omega,\Omega)$ as $H_{\rm MI}^{\rm GR}(\omega)$. Figure 3.5 shows the plot of the frequency response of a Michelson interferometer to the gravitational radiation. The absolute value of the frequency response is equal to zero at the angular frequency of $\omega = n\pi c/\bar{l}$ where n is a positive integer. When the frequency is much lower than the zero-response frequency (*i.e.*, $\omega\bar{l}/c \ll 1$), Eq. 3.35 is approximated as

$$H_{\rm MI}^{\rm GR}(\omega,\Omega) = 2\Omega\,\frac{\bar{l}}{c}\,\frac{1}{1+i\frac{\bar{l}}{c}\omega}. \tag{3.38}$$

Therefore the baseline $\bar{l}$ is related with the typical bandwidth $\omega_{\rm MI}$ of the frequency response of the interferometer by

$$\omega_{\rm MI} \sim c/\bar{l}\,. \tag{3.39}$$

On the other hand, at a given angular frequency ω, $|H_{\rm MI}^{\rm GR}|$ takes its maximum value $2\Omega/\omega$ at $l = (2n+1)c\pi/2\omega$. Therefore the optimum baseline $l_{\rm optimum}$ for the target gravitational radiation with the frequency f should be determined to satisfy the

[3]The techniques for the phase detection are discussed later in Sec. 6.2.

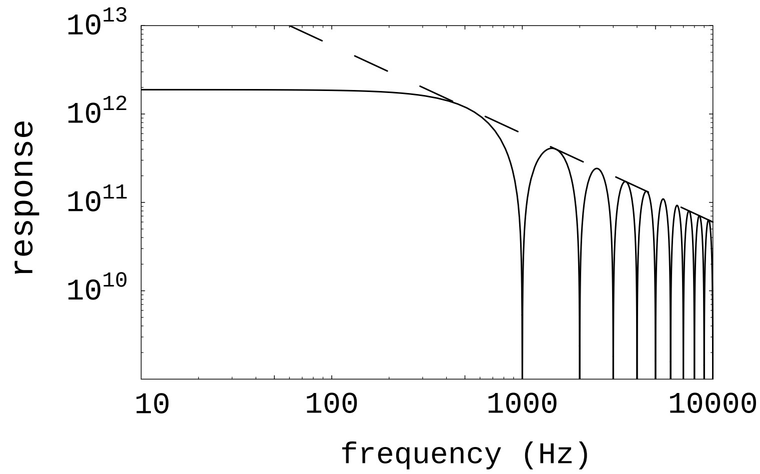

Figure 3.5: *Frequency response of a simple Michelson interferometer with the baseline of 150 km (solid line). Dashed line shows the upper envelope of the Michelson interferometer's response functions.*

equation,

$$l_{\text{optimum}} = c/4f\,. \tag{3.40}$$

For example, in order to detect the sinusoidal gravitational radiation with a frequency of 500 Hz, the optimum baseline is $l = 150\,\text{km}$.

3.3.2 Frequency Response of a Simple Michelson Interferometer to the Motion of the Mirrors

Let us assume that the beam-splitter is fixed at the origin, while the two mirrors are moving along the optical axis. The distance between the beam-splitter and the mirrors are expressed as $l_i + \delta l_i$ $(i = 1, 2)$. The field of light which is reflected by Mirror 1 or 2 in Fig. 3.4 is represented in the same way as Eq. 3.30. However, here the origin of the fluctuation of the delay is the motion of the mirrors, not the gravitational waves:

$$\Delta t_i = \frac{2}{c}\left[l_i + \delta l_i(t - \frac{1}{2}\Delta t_i)\right] \qquad (i = 1, 2). \tag{3.41}$$

To the first order of $\Delta l_i/c$, the expression for the delay Δt_i is written as

$$\Delta t_i \simeq \frac{2}{c}\left[l_i + \delta l_i\left(t - \frac{l_i}{c}\right)\right] \qquad (i = 1, 2). \tag{3.42}$$

Thus the delay of the phase Ωt_i $(i = 1, 2)$ is represented by

$$\begin{aligned}\theta_i &\equiv \Omega \Delta t_i \\ &= \Omega \left[\frac{2l_i}{c} + \frac{2}{c}\delta l_i \left(t - \frac{l_i}{c} \right) \right] \\ &\equiv \theta_{oi} + \delta\theta_{li}. \end{aligned} \tag{3.43}$$

We define the difference and the sum of the motion of the mirrors as

$$\delta l_+ = \delta l_1 + \delta l_2 \tag{3.44}$$

$$\delta l_- = \delta l_1 - \delta l_2. \tag{3.45}$$

The difference of the phase of the fields E_1 and E_2 is expressed as

$$\begin{aligned}\Delta\theta &= \theta_1 - \theta_2 \\ &\equiv \theta_{o1} - \theta_{o2} + \delta\theta_{l1} - \delta\theta_{l2} \\ &\equiv \Delta\theta_o + \delta\theta^l_{\rm MI}, \end{aligned} \tag{3.46}$$

where

$$\begin{aligned}\delta\theta^l_{\rm MI} &\equiv \delta\theta^{l-}_{\rm MI} + \delta\theta^{l+}_{\rm MI} \\ &\equiv \int \tilde{\delta l}_-(\omega) H^{l-}_{MI}(\omega) e^{i\omega t} d\omega + \int \tilde{\delta l}_+(\omega) H^{l+}_{MI}(\omega) e^{i\omega t} d\omega. \end{aligned} \tag{3.47}$$

In the above equation, the frequency response of a simple Michelson interferometer to the difference and the sum of the motion of the mirrors are represented by

$$H^{l-}_{\rm MI}(\omega) \equiv \frac{2\Omega}{c} \exp(\frac{-i\omega \bar{l}}{c}) \cos\frac{\omega l_-}{2c} \tag{3.48}$$

$$H^{l+}_{\rm MI}(\omega) \equiv -i\frac{2\Omega}{c} \exp(\frac{-i\omega \bar{l}}{c}) \sin\frac{\omega l_-}{2c}. \tag{3.49}$$

When the optical paths of the interferometer are equal to each other $(l_1 = l_2)$, the fluctuation of the phase difference $\delta\theta^l_{\rm MI}$ is insensitive to the common motion δl_+.

On the condition $\omega l_i/c \ll 1$ $(i = 1, 2)$ and $|l_-| \ll \bar{l}$, one can expand Eqs. 3.35 and 3.48 to the first order of $\omega\bar{l}/c$ as

$$\begin{aligned}H^{l-}_{\rm MI}(\omega) &\simeq \frac{2\Omega}{c}\left(1 - i\frac{\omega\bar{l}}{c}\right) + O(\frac{\omega l_-}{2c})^2 \\ H^{\rm GR}_{\rm MI}(\omega) &\simeq \frac{2\Omega\bar{l}}{c}\left(1 - i\frac{\omega\bar{l}}{c}\right) + O(\frac{\omega l_-}{2c})^2 \simeq \bar{l} H^{l-}_{\rm MI}(\omega). \end{aligned} \tag{3.50}$$

4. Fabry-Perot Cavities

In this chapter, the Fabry-Perot cavities as the parts of the interferometer are studied.

4.1 Fabry-Perot Cavity as a Device to Fold the Optical Path

As described in the preceding chapter, the optimum baseline of a Michelson interferometer is the order of 100km for the gravitational radiations from the astronomical sources. However, it is unrealistic to build such a large detector on the ground. Therefore, to obtain the optimum optical path length in the interferometer which can be built on the ground, the optical paths of the interferometer are folded by using delay-lines (DL) or Fabry-Perot (FP) cavities (Fig. 4.1). We will call the interferometer which has folded optical path in each of its arms as the delay-line-Michelson (DLM) or Fabry-Perot-Michelson (FPM) interferometer, depending on the device used to fold the paths.

A delay-line comprises two mirrors, and one of them has a small hole to inject the laser beam in it. The injected light is multiply bounced on the different point of the mirrors, then ejected through the hole (in the figure, the light is reflected three times in the delay-line, therefore the optical path length is $4L$ where L is the distance between the mirrors). A delay-line functions as a simple folded optical path, thus the frequency response of a DLM interferometer to the gravitational wave is just the same as the simple Michelson interferometer.

A Fabry-Perot cavity is a pair of the mirrors, but there is no hole on the mirrors. A fraction of the input light is transmitted by the front mirror, reflected many times inside

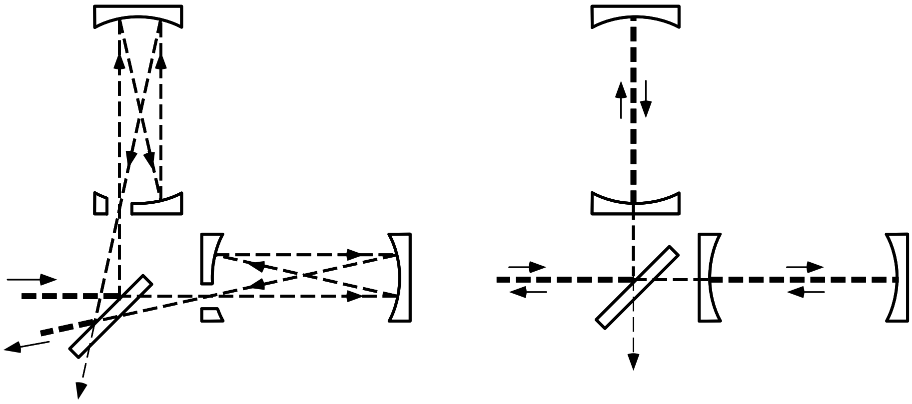

Figure 4.1: *Conceptual view of the Michelson interferometers whose optical paths are folded. A delay-line type interferometer (left) has an optical delay-line in each of its arms. A Fabry-Perot-Michelson interferometer (right) has optical resonators (Fabry-Perot cavities) instead of the delay-lines.*

the cavity (on the same point of the mirrors), and then transmitted again by the front mirror. When the direct reflection from the front mirror and the transmission from the inside interfere destructively, the effective optical path-length is much larger than the length of the cavity. Because an FP cavity is an interferometric device itself, the frequency response of a FPM interferometer is different from that of a simple Michelson interferometer.

Among the several medium-to-large scale detectors which are now being developed, the interferometers of the LIGO project, the VIRGO project, and the TAMA project will employ the FPM configuration. Though both DLM and FPM interferometer have their own advantages and disadvantages, to discuss their difference is beyond the scope of this paper. Rather, we will try only to discuss the optical properties of the FPM interferometers in the following discussion.

4.2 Frequency Response of a Fabry-Perot Cavity

In this section, the response of a Fabry-Perot cavity to the incident field of light and the gravitational radiation is briefly described.

4.2.1 Response to Light

The simplest case is considered here. Two mirrors are placed parallel to each other at a distance of L (Fig. 4.2). A plane wave of light which is traveling in the z direction is illuminating the mirrors. Let us call the mirror which is illuminated directly by the input beam the "front mirror", and the other mirror the "end mirror" [1]. The field of light is expressed as

$$E_{\rm i}(t,z) = E_0 \exp\Big[i(\Omega t - Kz)\Big] \tag{4.1}$$

where Ω is the angular frequency of the light and $K = \Omega/c$ is the wave number. This input field which has the single frequency is sometimes called the "carrier". The propagating direction of the wave is perpendicular to the mirrors. The reflection coefficient and the transmission coefficient of the mirrors are represented by $(r_{\rm f}, t_{\rm f})$ and $(r_{\rm e}, t_{\rm e})$. The signs of the reflection coefficient of both of the mirrors are chosen to be plus inside the cavity. We define the capitalized symbols $R_i = r_i^2$, $T_i = t_i^2$ $(i = {\rm f}, {\rm e})$, $R_{\rm fe} = r_{\rm f} r_{\rm e}$, and $T_{\rm fe} = t_{\rm f} t_{\rm e}$. The fields of the reflected and transmitted light outside the cavity are given by

$$\begin{aligned} E_{\rm r} &= E_0 \left[-r_{\rm f} + r_{\rm e} T_{\rm f} e^{-i\Phi_{\rm o}} \sum_{n=0}^{\infty} \left(r_{\rm f} r_{\rm e} e^{-i\Phi_{\rm o}} \right)^n \right] \exp\Big[i(\Omega t + Kz)\Big] \\ &= E_0 \left[-r_{\rm f} + r_{\rm e} T_{\rm f} \frac{\exp(-i\Phi_{\rm o})}{1 - R_{\rm fe} \exp(-i\Phi_{\rm o})} \right] \exp\Big[i(\Omega t + Kz)\Big] \end{aligned} \tag{4.2}$$

$$\begin{aligned} E_{\rm t} &= E_0 t_{\rm f} t_{\rm e} \sum_{n=0}^{\infty} \left(r_{\rm f} r_{\rm e} e^{-i\Phi_{\rm o}} \right)^n \exp\Big[i(\Omega t - Kz)\Big] \\ &= E_0 \frac{T_{\rm fe}}{1 - R_{\rm fe} \exp(-i\Phi_{\rm o})} \exp\Big[i(\Omega t - Kz)\Big] \end{aligned} \tag{4.3}$$

where $\Phi_{\rm o} = 2\Omega L/c$ is a round-trip phase of light inside the cavity. Note that the Mirror 1 in Fig. 4.2 is placed at $z = 0$ in these expressions. If the field of reflection and that of transmission are measured at $z = 0$ and $z = L$, respectively, the reflection coefficient and the transmission coefficient of the cavity are defined from Eqs. 4.1, 4.2, and 4.3 as

$$r_{\rm c}(\Phi_{\rm o}) = -r_{\rm f} + r_{\rm e} T_{\rm f} \frac{\exp(-i\Phi_{\rm o})}{1 - R_{\rm fe} \exp(-i\Phi_{\rm o})} \tag{4.4}$$

[1] The terms "front mirror" and "end mirror" will often be used throughout this paper, although they are not well-recognized technical terms.

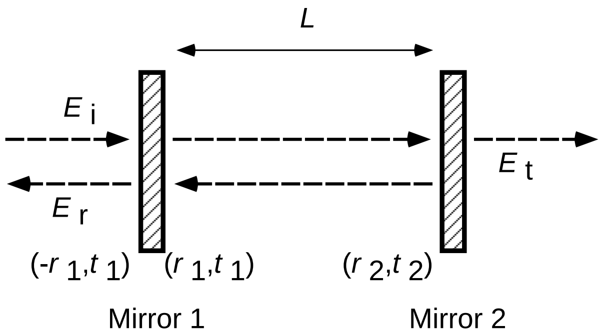

Figure 4.2: *A simple Fabry-Perot cavity. Two mirrors are placed parallel to each other at a distance of L. We will call Mirror 1, which is illuminated directly by the input light, the "front mirror", and Mirror 2 the "end mirror".*

$$t_{\rm c}(\Phi_{\rm o}) \quad = \quad \frac{T_{\rm fe}}{1 - R_{\rm fe}\exp(-i\Phi_{\rm o})}\exp(-i\frac{\Phi_{\rm o}}{2}). \tag{4.5}$$

These coefficients represent the frequency response of a Fabry-Perot cavity to light. Sometimes we will write $r_{\rm c}(\Phi_{\rm o})$ and $t_{\rm c}(\Phi_{\rm o})$ as $r_{\rm c}(\Omega)$ and $t_{\rm c}(\Omega)$, or $r_{\rm c}(L)$ and $t_{\rm c}(L)$, when either L or Ω is considered as a constant.

A plot of the amplitude and the phase shift of the reflected and the transmitted light from the FP cavity versus round-trip phase is shown in Fig. 4.3. There are a resonance peak of the absolute value when the round-trip phase is $2n\pi$, where n is an integer. The phase curve is very steep around the peak. Thus, around the resonance, only the phase of the field changes to the first order approximation. The finesse of the cavity $\mathcal{F}$ is defined by the ratio of the spacing of the two near-by peaks and the full-width of half-maximum (FWHM) of the intensity of transmission,

$$\begin{aligned} \mathcal{F} &\equiv \frac{2\pi}{\rm FWHM} \\ &= \frac{\pi\sqrt{R_{\rm fe}}}{1 - R_{\rm fe}}. \end{aligned} \tag{4.6}$$

The reflection and the transmission coefficient of the cavity are simplified when $\Phi_{\rm o} \ll 1$ and $\mathcal{F} \gg 1$;

$$\begin{aligned} r_{\rm c}(\Phi_{\rm o}) &\sim -r_{\rm f} + T_{\rm f}\frac{\mathcal{F}}{\pi}\frac{1}{1 + i\frac{\mathcal{F}}{\pi}\Phi_{\rm o}} \\ &= -r_{\rm f} + T_{\rm f}\frac{\mathcal{F}}{\pi}\frac{1}{1 + i\frac{\omega}{\omega_{\rm c}}} \end{aligned} \tag{4.7}$$

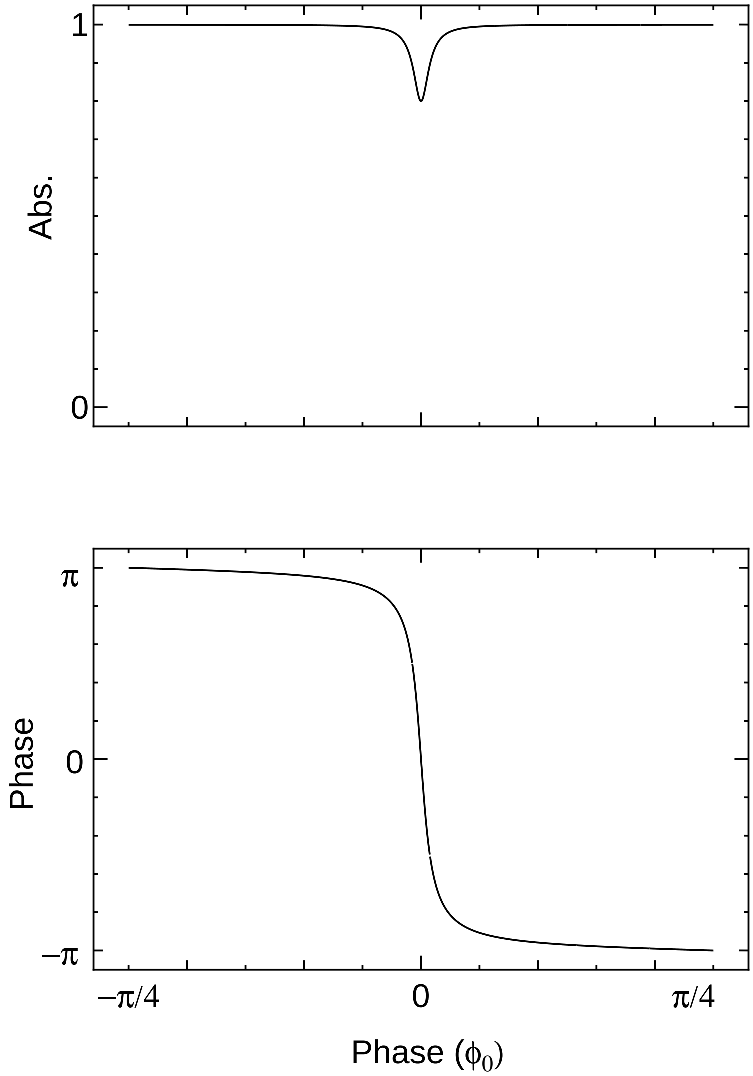

Figure 4.3: *The response of a Fabry-Perot cavity to the round-trip phase ϕ_0. The reflectance of the mirrors are chosen to be 82.64% for the front mirror and 98% for the end, thus the finesse is about 30.*

Quantity	Symbol	Definition
Finesse	$\mathcal{F}$	$\frac{\pi\sqrt{R_{\mathrm{fe}}}}{1-R_{\mathrm{fe}}}$
Free Spectral Range (FSR)	ν_{FSR}	$\frac{c}{2L_0}$
Cut-Off Frequency	f_{c}	$\frac{c}{4\mathcal{F}L_0} = \frac{\nu_{\mathrm{FSR}}}{2\mathcal{F}}$
Cut-Off Angular Frequency	ω_{c}	$2\pi f_{\mathrm{c}}$
Storage Time	τ_{s}	$\frac{2\mathcal{F}L_0}{c\pi} = \omega_{\mathrm{c}}^{-1}$

Table 4.1: *Table of some quantities related to FP cavities.*

$$\begin{aligned} t_{\mathrm{c}}(\Phi_{\mathrm{o}}) &\sim T_{\mathrm{fe}}\frac{\mathcal{F}}{\pi}\frac{1}{1+i\frac{\mathcal{F}}{\pi}\Phi_{\mathrm{o}}} \\ &= T_{\mathrm{fe}}\frac{\mathcal{F}}{\pi}\frac{1}{1+i\frac{\omega}{\omega_{\mathrm{c}}}}. \end{aligned} \tag{4.8}$$

Table 4.1 shows the definition of ω_{c} (the inverse of the storage time τ_{s}) in the above equation, together with the definitions of other quantities about FP cavities. We will not try to discuss the physical implications of such quantities, because there are many good textbooks such as Ref. 22.

4.2.2 Response to Gravitational Waves

An incident gravitational wave is propagating in the z direction. We choose the coordinate system in which the metric is given by Eq. 3.29. One mirror of a Fabry-Perot cavity is placed at $x = 0$ and the other is placed at $x = L$. The optical axis of the cavity and that of the illuminating laser beam lie exactly on the x axis. We assume that the mirrors are free masses, therefore they will not move in this coordinate system even though there is an incident gravitational wave. However, the incident gravitational wave affects the proper-length of the cavity, thus affects the round trip phase of light.

The reflected field at the input mirror is represented by

$$E_{\mathrm{r}} = E_0 e^{i\Omega t}\left[-r_{\mathrm{f}} + r_{\mathrm{e}}T_{\mathrm{f}}\sum_{n=1}^{\infty}(r_{\mathrm{f}}r_{\mathrm{e}})^{n-1}\exp(-i\Omega\,\Delta t_n)\right], \tag{4.9}$$

where Δt_n is a delay for the wave front which arrived at $x = 0$ after n-round trip inside the cavity. By using the same approximations as used in Eqs. 2.39–2.43, we can obtain the expression for Δt_n:

$$\Delta t_n = \frac{2Ln}{c} + \frac{1}{2}\int_{t-2Ln/c}^{t} h(t')dt' \,. \tag{4.10}$$

After some calculation using Eqs. 4.4, 4.9, and 4.10, we obtain the field of the reflected light written as

$$\begin{aligned} E_{\rm r} &= E_0 e^{i\Omega t} r_{\rm c}(\Omega)\left[1 - i\int \tilde{h}(\omega) H_{\rm FP}^{\rm GR}(\omega,\Omega) e^{i\omega t} d\omega\right] \\ &\equiv E_0 e^{i\Omega t} r_{\rm c}(\Omega)\left[1 - i\delta\Psi_{\rm FP}^{\rm GR}(t,\Omega)\right]. \end{aligned} \tag{4.11}$$

The complex function $H_{\rm FP}^{\rm GR}(\omega,\Omega)$ represents the frequency response of a FP cavity to the gravitational radiation, which is defined as follows;

$$H_{\rm FP}^{\rm GR}(\omega,\Omega) \equiv \frac{\Omega}{2i\omega}\frac{r_{\rm c}(\Omega) - r_{\rm c}(\omega+\Omega)}{r_{\rm c}(\Omega)}. \tag{4.12}$$

This is apparently the function of the angular frequency ω and the round-trip phase of the carrier inside the cavity $\Phi_{\rm o}$, therefore we will sometimes write $H_{\rm FP}^{\rm GR}(\omega,\Omega)$ and $\delta\Psi_{\rm FP}^{\rm GR}(t,\Omega)$ as $H_{\rm FP}^{\rm GR}(\omega,\Phi_{\rm o})$ and $\delta\Psi_{\rm FP}^{\rm GR}(t,\Phi_{\rm o})$ when it is convenient. We can see that there are the carrier (the first term in Eq. 4.11) and the additional field (the integral term). The additional field is sometimes called the 'sidebands' which is produced by the gravitational radiation.

When the frequency of light is tuned to the resonance of the cavity (i. e. $\Omega L/c = n\pi$), it is easy to show that the term $\delta\Psi_{\rm FP}^{\rm GR}(t,\Omega)$ in Eq. 4.11 is a real number. Therefore $\delta\Psi_{\rm FP}^{\rm GR}(t,\Omega)$ is interpreted as a phase shift of the carrier which is produced by the gravitational wave. In this case, the expression for Eq. 4.12 is simplified. we will write $\delta\Psi_{\rm FP}^{\rm GR}(t,\Omega)$ as $\delta\Psi_{\rm FP}^{\rm GR}(t)$ in this paper, in order to denote that this is in this special case;

$$\begin{aligned} \delta\Psi_{\rm FP}^{\rm GR}(t) &\equiv \delta\Psi_{\rm FP}^{\rm GR}(t,\Omega)\Big|_{\Omega L/c = n\pi} \\ &= \int \tilde{h}(\omega) H_{\rm FP}^{\rm GR}(\omega) e^{i\omega t} d\omega \end{aligned} \tag{4.13}$$

where

$$\begin{aligned} H_{\rm FP}^{\rm GR}(\omega) &\equiv H_{\rm FP}^{\rm GR}(\omega,\Omega)\Big|_{\Omega L/c = n\pi} \\ &\sim \frac{\Omega}{2\omega_{\rm c}}\frac{1}{r_{\rm c}(0)}\frac{\mathcal{F}T_{\rm f}}{\pi}\frac{1}{1 + i\frac{\omega}{\omega_{\rm c}}}. \end{aligned} \tag{4.14}$$

The last approximation comes from Eq. 4.7. Figure 4.4 shows the response function $H_{\rm FP}(\omega)$.

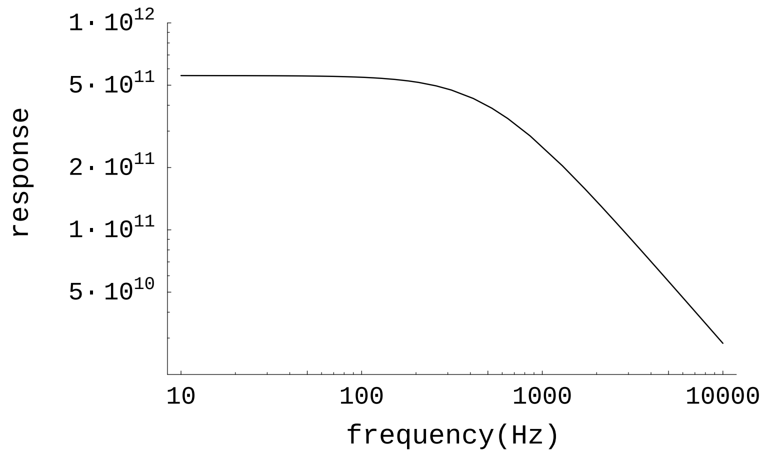

Figure 4.4: *The absolute value of the response function* $H_{\rm FP}^{\rm GR}$ *of a FP cavity to the gravitational radiation versus frequency. In this plot, the finesse and the length are chosen to be* 50 *and* 3 km*, respectively.*

4.2.3 Response to the Motion of the Mirrors

The phase of the reflected light from the FP cavity can be disturbed by the motion of the mirrors along the optical axis (also the frequency of the light is changed by the Doppler-shift caused by the motion of the mirror, but we will ignore this effect). Let us assume that the front mirror is fixed at the origin while the end mirror is moving along the optical axis with a small amplitude $\delta L(t)$. The length of the cavity is represented by

$$L(t) = L_0 + \delta L(t), \tag{4.15}$$

where L_0 is the mean length of the cavity. After a n-round trip inside the cavity, a part of the input field gets out of the cavity at the time t with a time delay of T_n which is given by

$$\begin{aligned} T_n &= \frac{2}{c}nL_0 + \frac{2}{c}\sum_{l=1}^{n}\delta L\left[t - \frac{1}{c}(2n-1)L_0\right] \\ &= \frac{2}{c}nL_0 + \frac{2}{c}\int \widetilde{\delta L}(\omega)e^{i(\omega t - kL_0)}\frac{1-e^{-2iknL_0}}{1-e^{-2ikL_0}}d\omega \end{aligned} \tag{4.16}$$

to the first order of the fluctuation, where $\widetilde{\delta L}(\omega)$ is the Fourier transform of $\delta L(t)$ and k is defined by $k = \omega/c$. When the input field is defined by Eq. 4.1, the expression for the reflected field is obtained by using Eq. 4.16 after some calculation as

$$
\begin{aligned}
E_{\mathrm{r}}(t) &= E_0 e^{i\Omega t}\left[-r_{\mathrm{f}} + r_{\mathrm{e}}T_{\mathrm{f}}\sum_{n=1}^{\infty}(r_{\mathrm{f}}r_{\mathrm{e}})^{n-1}e^{-i\Omega T_n}\right] \\
&= E_0 e^{i\Omega t} r_{\mathrm{c}}(\phi_0)\left[1 - i\int \widetilde{\delta L}(\omega)e^{i\omega t}\frac{\Omega}{ic\sin\frac{\omega L_0}{c}}\frac{r_{\mathrm{c}}(\phi_0) - r_{\mathrm{c}}(\phi_0+\phi)}{r_{\mathrm{c}}(\phi_0)}d\omega\right] \\
&= E_0 e^{i\Omega t} r_{\mathrm{c}}(\phi_0)\left[1 - i\int \widetilde{\delta L}(\omega)H^{L}_{\mathrm{FP}}(\omega,\Omega)e^{i\omega t}d\omega\right], \qquad (4.17)
\end{aligned}
$$

where $\phi_0 = 2Kl_0$ is the mean round-trip phase inside the cavity. In the above equation, the complex function $H^L_{\mathrm{FP}}(\omega,\Omega)$, which represents the frequency response of a FP cavity to the length-fluctuation, is defined as

$$
\begin{aligned}
H^L_{\mathrm{FP}}(\omega,\Omega) &\equiv \frac{\Omega}{ic\sin\frac{\omega L_0}{c}}\frac{r_{\mathrm{c}}(\phi_0) - r_{\mathrm{c}}(\phi+\phi_0)}{r_{\mathrm{c}}(\phi_0)} \\
&= \frac{\Omega}{ic\sin\frac{\omega L_0}{c}}\frac{r_{\mathrm{c}}(\Omega) - r_{\mathrm{c}}(\omega+\Omega)}{r_{\mathrm{c}}(\Omega)}. \qquad (4.18)
\end{aligned}
$$

The delay of the phase $\delta\Psi^L_{\mathrm{FP}}$ which is caused by the motion of the mirror is defined in the same way as Eq. 4.13 by

$$
\delta\Psi^L_{\mathrm{FP}}(t) = \int \widetilde{\delta L}(\omega)\ H^L_{\mathrm{FP}}(\omega,\Omega)\Big|_{(\Omega L_0/c)=n\pi} e^{i\omega t}d\omega. \qquad (4.19)
$$

By comparing Eqs. 4.12 and 4.18, it is apparent that the gravitational radiation of the amplitude h has the same effect as the length fluctuation of the amplitude $\frac{h}{2}L_0$ (this value is equal to the change of the proper distance between the mirrors), when the frequency of the motion is small compared to the free spectral range. In other words,

$$
H^{\mathrm{GR}}_{\mathrm{FP}}(\omega,\Omega) \simeq \frac{L_0}{2}H^L_{\mathrm{FP}}(\omega,\Omega) \qquad (4.20)
$$

when

$$
\omega L_0/c << 1. \qquad (4.21)
$$

When the cavity is tuned to the resonance, the frequency response is approximated as

$$
\begin{aligned}
H^{\mathrm{L}}_{\mathrm{FP}}(\omega) &\equiv H^{\mathrm{L}}_{\mathrm{FP}}(\omega,0) \\
&\sim \frac{2\Omega}{cr_{\mathrm{c}}(0)}\frac{\mathcal{F}^2T_{\mathrm{f}}}{\pi^2}\frac{1}{1+i\frac{\omega}{\omega_{\mathrm{c}}}}. \qquad (4.22)
\end{aligned}
$$

4.2.4 Response to the Fluctuation of the Phase of Light

In the discussion presented above, it is assumed that the phase of light has no fluctuation. However, in a more realistic situation, the phase of light $\phi(t)$ has a small fluctuation term $\delta\phi(t)$,

$$\begin{aligned}\phi(t) &= \Omega t + \delta\phi(t) \\ &= \Omega t + \int \widetilde{\delta\phi}(\omega) e^{i\omega t} d\omega,\end{aligned} \tag{4.23}$$

where $\widetilde{\delta\phi}(\omega)$ is a Fourier transform of $\delta\phi(t)$. Assuming that $|\delta\phi(t)| << 1$, the incident field is expanded in terms of $\delta\phi$ to the first order as

$$\begin{aligned}E_{\rm i}(t) &= E_0 \exp\Big[i\left(\Omega t + \delta\phi(t)\right)\Big] \\ &\simeq E_0 e^{i\Omega t}\Big[1 + i\delta\phi(t)\Big] \\ &= E_0 e^{i\Omega t}\left[1 + i\int \widetilde{\delta\phi}(\omega) e^{i\omega t} d\omega\right].\end{aligned} \tag{4.24}$$

Let us assume that the length of the cavity is not fluctuating, $L = L_0$. Now the reflected field is related with the reflection coefficient of the cavity as

$$\begin{aligned}E_{\rm r}(t) &= E_0 e^{i\Omega t}\left[r_{\rm c}(\Omega) + i\int r_{\rm c}(\Omega+\omega)\widetilde{\delta\phi}(\omega) e^{i\omega t} d\omega\right] \\ &= E_0 e^{i\Omega t} r_{\rm c}(\Omega)\left[1 + i\delta\phi(t) - i\int \frac{r_{\rm c}(\Omega) - r_{\rm c}(\omega+\Omega)}{r_{\rm c}(\Omega)}\widetilde{\delta\phi}(\omega) e^{i\omega t} d\omega\right].\end{aligned} \tag{4.25}$$

We introduce the frequency fluctuation $\widetilde{\delta\nu}(\omega)$ which is defined by

$$\widetilde{\delta\nu}(\omega) \equiv i\omega\frac{\widetilde{\delta\phi}(\omega)}{2\pi}. \tag{4.26}$$

Using this frequency fluctuation, the reflected field is expressed as

$$E_{\rm r}(t) = E_0 e^{i\Omega t} r_{\rm c}(\Omega)\left[1 + i\delta\phi(t) - i\int H^{\phi}_{\rm FP}(\omega,\Omega)\widetilde{\delta\nu}(\omega) e^{i\omega t} d\omega\right], \tag{4.27}$$

where $H^{\phi}_{\rm FP}$, which represents the frequency response of a FP cavity to the frequency fluctuation, is defined as

$$H^{\phi}_{\rm FP}(\omega,\Omega) = \frac{2\pi}{i\omega}\frac{r_{\rm c}(\Omega) - r_{\rm c}(\omega+\Omega)}{r_{\rm c}(\Omega)}. \tag{4.28}$$

By comparing Eqs. 4.12, 4.18, and 4.28, one can see that the frequency response of a FP cavity to the gravitational radiation, the motion of the mirror, and the frequency fluctuation is related to each other;

$$H^{\phi}_{\mathrm{FP}}(\omega,\Omega) = \frac{2}{\nu_{\mathrm{o}}} H^{(GR)}_{\mathrm{FP}}(\omega,\Omega) \tag{4.29}$$

$$\simeq \frac{L_0}{\nu_{\mathrm{o}}} H^{L}_{\mathrm{FP}}(\omega,\Omega), \tag{4.30}$$

where $\nu_{\mathrm{o}} \equiv \Omega/2\pi$.

When the center frequency of light is tuned to the cavity, the third term in Eq. 4.27 is interpreted as an additional phase shift which is caused by the FP cavity. This phase shift is defined by

$$\delta\Psi^{\phi}_{\mathrm{FP}}(t) \equiv \int H^{\phi}_{\mathrm{FP}}(\omega,0)\widetilde{\delta\nu}(\omega)e^{i\omega t}d\omega, \tag{4.31}$$

just in the same way as Eq. 4.13. Equation 4.28 is then simplified as

$$H^{\phi}_{\mathrm{FP}}(\omega,0) = \frac{2}{\omega_{\mathrm{c}}}\frac{\mathcal{F}T_{\mathrm{f}}}{r_{\mathrm{c}}(0)}\frac{1}{1+i\frac{\omega}{\omega_{\mathrm{c}}}}. \tag{4.32}$$

4.2.5 Pound-Drever-Hall Technique

We have seen that the gravitational radiation, the motion of the mirror, and the phase fluctuation of the light produce the shift in the phase of the reflected light from a FP cavity. Such phase-shifts can be sensed by the Pound-Drever-Hall (P-D-H) technique [28]. Though there are many papers in which the P-D-H technique is discussed, it is still useful to present some ideas and calculations here. The basic concept of the technique is to use the radio-frequency sidebands as the reference of the phase which are not affected by the FP cavity.

Suppose that the field is phase-modulated so it is written in the form

$$E_{\mathrm{i}} = E_0 \exp\left[i(\Omega t + m\sin\omega_{\mathrm{m}} t)\right], \tag{4.33}$$

where m is the modulation index and ω_{m} is the angular frequency of the modulation. Such a field is generated by using an Electro-Optical-Modulator (EOM). Assuming that the modulation index is much smaller than 1, the field is expanded to the first order of the modulation index as

$$\begin{aligned} E_{\mathrm{i}} &= E_0 \exp(i\Omega t)(1 + im \sin \omega_{\mathrm{m}} t) \\ &= E_0 \exp(i\Omega t)\left[1 + \frac{m}{2}(e^{i\omega_{\mathrm{m}} t} - e^{-i\omega_{\mathrm{m}} t})\right]. \end{aligned} \tag{4.34}$$

(There is a mathematical formula [31]

$$\exp(im \sin \omega_{\mathrm{m}} t) = \sum_{n=-\infty}^{+\infty} J_n(m) e^{in\omega_{\mathrm{m}} t}, \tag{4.35}$$

where J_n is the set of Bessel functions. Therefore we can expand the input field to the n-th order of m, though this is not essential to the calculation presented below.) Now the field comprises a carrier and two sidebands. The frequency of the sidebands is equally shifted from the carrier, in the opposite sign.

Next, suppose that the input field has a phase fluctuation which is represented by Eq. 4.24. We modulate the phase of this field, therefore the field is written as

$$E_{\mathrm{i}} = E_0 e^{i\Omega t}\left[1 + i\int \widetilde{\delta\phi}(\omega) e^{i\omega t} d\omega\right]\left[1 + \frac{m}{2}(e^{i\omega_{\mathrm{m}} t} - e^{-i\omega_{\mathrm{m}} t})\right]. \tag{4.36}$$

This input field is reflected from a FP cavity which is resonant with the carrier. The cavity is interacting with the gravitational radiation and the mirror of this cavity is moving with a small amplitude. The frequency of the phase-modulation is assumed to be in the radio-frequency range, therefore the modulation sidebands are off the resonance and approximately all of them are reflected. Combining the above assumption with Eqs. 4.11,4.13, 4.17,4.19, 4.27, and 4.31, we obtain the following expression of the reflected field to the first order of the perturbation;

$$\begin{aligned} E_{\mathrm{r}} &= E_0 e^{i\Omega t}\Big\{ r_{\mathrm{c}}(0)\left[1 + i\left(\delta\phi(t) - \delta\Psi_{\mathrm{FP}}^{\mathrm{GR}}(t) - \delta\Psi_{\mathrm{FP}}^{L}(t) - \delta\Psi_{\mathrm{FP}}^{\phi}(t)\right)\right] \\ &\quad - \left[1 + i\delta\phi(t)\right]\frac{m}{2}(e^{i\omega_{\mathrm{m}} t} - e^{-i\omega_{\mathrm{m}} t})\Big\}. \end{aligned} \tag{4.37}$$

The intensity of the field is measured by a photo-detector and only the terms that are proportional to $\exp(\pm i\omega_{\mathrm{m}} t)$ are lock-in detected by mixing the intensity signal with the local oscillator which is used for the phase modulation (Fig. 4.5). Thus, the output of the mixer is proportional to the phase shift caused by the gravitational radiation, motion of the mirror, and the phase fluctuation;

$$v_{\mathrm{mix}} = R\frac{e\eta I_0}{\hbar\Omega} m r_{\mathrm{c}}(0)\left[\delta\Psi_{\mathrm{FP}}^{\mathrm{GR}}(t) + \delta\Psi_{\mathrm{FP}}^{L}(t) + \delta\Psi_{\mathrm{FP}}^{\phi}(t)\right], \tag{4.38}$$

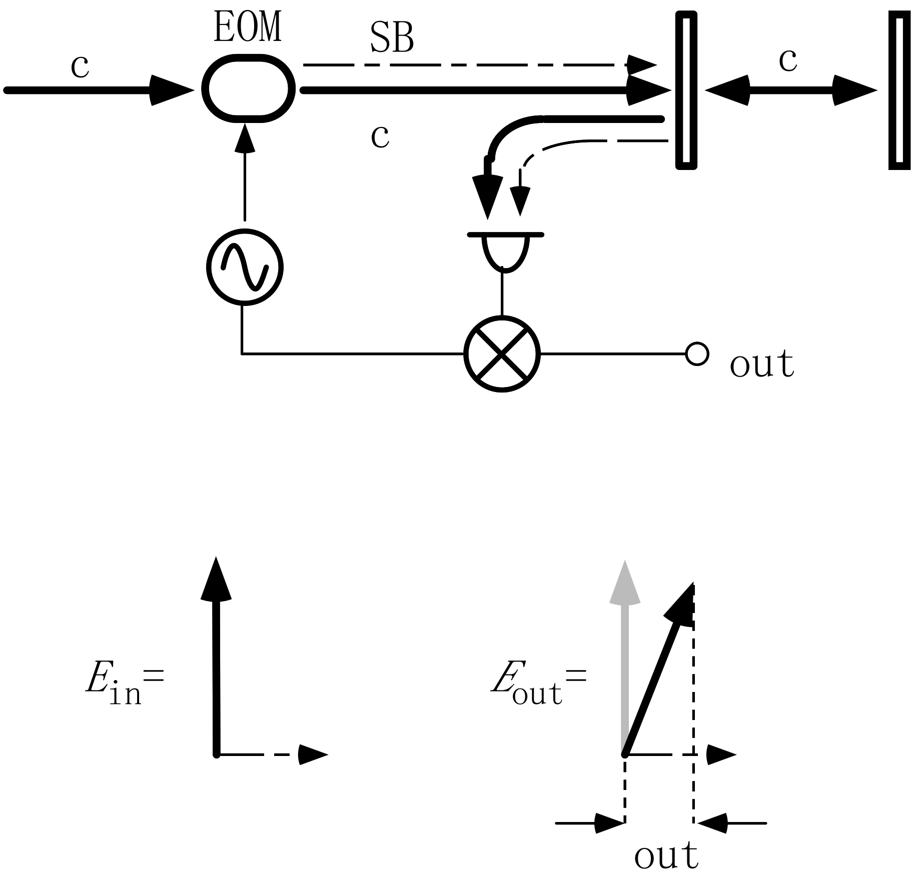

Figure 4.5: *A FP cavity is illuminated by phase-modulated light. The intensity of the light is sensed by a photo-detector. The signal of the photo-detector is mixed with a local oscillator signal which is used for the phase modulation. Because only the carrier ("c" in the figure) is resonant with the cavity, any change of the cavity length will cause a rotation of the carrier in the phase diagram while sidebands ("SB" in the figure) are not affected. The inner product of the carrier vector and the sideband vector is proportional to the motion of the cavity.*

where R, e, η, I_0, and $\hbar$ are the effective resistance of the photo-detector plus the mixer, the elementary electronic charge, the quantum efficiency of the photo-detector, the power of the light, and Planck's constant divided by 2π, respectively.

5. Modal Analysis

So far, the laser beams and the field inside the interferometer were treated as the plane wave. However, if we want to make a quantitative discussion about the coupling between the beam and the cavity, we have to take account of the fact that the wavefront of the beam is curved. Here we will study how the misalignment of the mirrors couple to the deformation of the mode of the input light.

5.1 Hermite-Gaussian Field

The field of the laser beams and the eigenmodes of the optical resonators are well approximated by a set of the Hermite-Gaussian fields [22, 32], which are represented by

$$
\begin{aligned}
E_{lm+}(x,y,z,t) &= U_{lm+}(x,y,z)\exp(i\Omega t) &(5.1)\\
U_{lm+}(x,y,z) &\equiv U_{l+}(x,z)U_{m+}(y,z)\exp i\Big[-Kz+(l+m+1)\eta(z)\Big] &(5.2)\\
U_{l+}(x,z) &\equiv \left(\frac{2}{\pi w^2(z)}\right)^{1/4}\left(\frac{1}{l!2^l}\right)^{1/2}H_l\left(\frac{\sqrt{2}x}{w(z)}\right)\exp\left[-\frac{x^2}{w^2(z)}-i\frac{Kx^2}{2R(z)}\right], &(5.3)
\end{aligned}
$$

where K represents the wavenumber of the field. In the above equations, the beam radius $w(z)$, the radius of curvature of the wavefront $R(z)$, the Gouy phase $\eta(z)$, and the Hermite-polynomial H_l are defined as follows:

$$
\begin{aligned}
w(z) &\equiv w_0\sqrt{1+(z/z_0)^2} &(5.4)\\
R(z) &\equiv \left(z^2+z_0^2\right)/z &(5.5)\\
\eta(z) &\equiv \arctan\frac{z}{z_0} &(5.6)\\
z_0 &\equiv \frac{Kw_0^2}{2} &(5.7)
\end{aligned}
$$

$$H_l(x) \;=\; (-1)^l\, e^{x^2} \frac{d^l}{dx^l} e^{-x^2}. \tag{5.8}$$

The point at which the beam radius takes its minimum is called the waist of the beam, and the minimum value w_0 is called the waist radius. From Eqs. 5.4 and 5.7, one can see that the far-field divergence angle α_0 is written as

$$\alpha_0 = \left(\frac{K w_0}{2}\right)^{-1}. \tag{5.9}$$

A set of the Hermite-Gaussian fields of a single frequency is completely characterized by the propagation axis (the z axis in Eq. 5.2), the position of the waist ($z = 0$ in Eq. 5.2), and the waist radius w_0. Each field in the set is numbered by the two positive integer l and m. The sum of these integers $l + m$ is sometimes called the order of the field. Two fields of the same order have the same Gouy phase shift $(l + m + 1)\eta(z)$.

Inverting the sign of the K-vector (and other related parameters such as z_0), the expression for the Hermite-Gaussian mode which is inversely propagating along the z axis is written as

$$E_{lm-}(x, y, z, t) \;=\; U_{lm-}(x, y, z) \exp(i\Omega t) \tag{5.10}$$

$$U_{lm-} \;=\; U^*_{lm+} \tag{5.11}$$

$$U_{l-} \;=\; U^*_{l+}. \tag{5.12}$$

A set of the Hermite-Gaussian modes is ortho-normal, i.e.,

$$\int_{-\infty}^{+\infty}\int_{-\infty}^{+\infty} U_{lm\pm}(x, y, z) U^*_{pq\pm}(x, y, z) dxdy = \delta_{lp}\delta_{mq}. \tag{5.13}$$

Also, a set of $\{U_{l\pm}\}$ is ortho-normal;

$$\int_{-\infty}^{+\infty} U_{l\pm}(x, z) U^*_{m\pm}(x, z) dx = \delta_{lm}. \tag{5.14}$$

5.2 Eigenmodes of a Fabry-Perot Cavity

A Fabry-Perot cavity has a set of Hermite-Gaussian fields $\{U_{lm}\}$ as its eigenmodes[1]. The propagation axis of the eigenmodes is the one which is perpendicular to both of

[1] In a Fabry-Perot cavity, the field is reflected many times by the two mirrors. Only the fields with the wavefronts that are not deformed by the reflection can remain stable in the cavity, thus we call a set of the stable fields in the cavity the eigenmodes of the cavity.

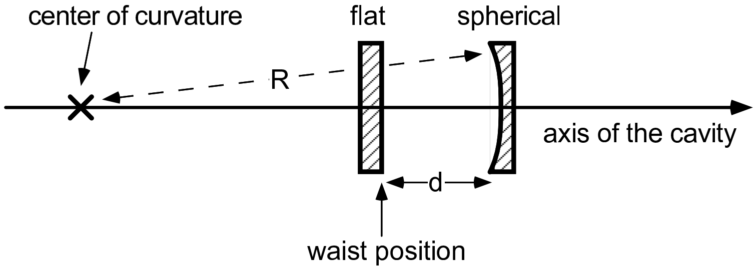

Figure 5.1: *An axis of the eigenmodes of a Fabry-Perot cavity which comprises a flat mirror and a spherical mirror. The axis is perpendicular to both of the mirrors and intersects the center of curvature of the spherical mirror.*

the two mirrors. When the cavity comprises a flat mirror and a spherical mirror, the axis intersects the center of curvature of the spherical mirror. The waist of the cavity is located at the flat mirror (Fig.5.1). The waist radius of the cavity is determined by

$$w_0^2 = \frac{\lambda}{\pi}\sqrt{d(R-d)}, \tag{5.15}$$

where d is the distance between the two mirrors and R is the radius of curvature of the concave mirror. Due to the Gouy phase shift, the modes of the different order have the different resonant frequencies. The resonant condition for the $(l+m)$th order mode is written as

$$\begin{aligned} \nu_{\mathrm{o}} &= \nu_{\mathrm{FSR}}\Big\{n + (l+m+1)\frac{1}{\pi}\left[\eta(z_1) - \eta(z_2)\right]\Big\} \\ &\equiv n\nu_{\mathrm{FSR}} + (l+m+1)\nu_{\mathrm{G}} \end{aligned} \tag{5.16}$$

where n, z_1 and z_2 are a positive integer and the positions of the mirrors, respectively. Especially, the Gouy phase contribution ν_{G} is expressed as

$$\nu_{\mathrm{G}} = \frac{\nu_{\mathrm{FSR}}}{\pi}\arccos\sqrt{1-\frac{d}{R}} \tag{5.17}$$

when the mirrors of the cavity are flat and concave (radius of curvature R), or

$$\nu_{\mathrm{G}} = \frac{\nu_{\mathrm{FSR}}}{\pi}\arccos\left(1-\frac{d}{R}\right) \tag{5.18}$$

when the cavity comprises the mirrors with the same radius of curvature R.

5.3 The Vector Representation of the Paraxial Field

Any paraxial field which is written as $E(x, y, z)\exp(i\Omega t)$ can be expanded by a set of Hermite-Gaussian modes (Refs. 22). If the field is paraxial around the z axis in the positive direction, it is expanded as

$$\begin{aligned} E(x, y, z) &= \sum_{lm} < lm|E > U_{lm+}(x, y, z) && (5.19) \\ < lm|E > &\equiv \int_{-\infty}^{+\infty} \int_{-\infty}^{+\infty} U^*_{lm+}(x, y, z) E(x, y, z)\, dx\, dy. && (5.20) \end{aligned}$$

It is natural to look at the coefficients $\{< lm|E >\}$ as the components of the vector that represent the field:

$$[E] = \begin{pmatrix} < 00|E > \\ < 01|E > \\ < 10|E > \\ < 20|E > \\ < 11|E > \\ \vdots \end{pmatrix} \tag{5.21}$$

Any operation that affects the modes of the field (beam transformation by a lens, for example) is represented by a matrix.

5.4 Matrix Representation of the Transmission and Reflection Coefficient

An optical component is characterized by its transmission and reflection coefficient, which are defined as the ratio of the amplitude of the transmitted and reflected field to the input. However, not only the amplitude, but also the beam characteristics are changed by the optical components. The concept of the beam characteristics and the transmission and reflection coefficient can be combined by using the modal expansion.

The input, the reflection, and the transmission field are expanded in terms of the modes defined on a reference axis (the z axis in this case[2])(Fig. 5.2). The fields are

[2] We can choose an arbitrary coordinate system, so far as the beams can be considered as paraxial.

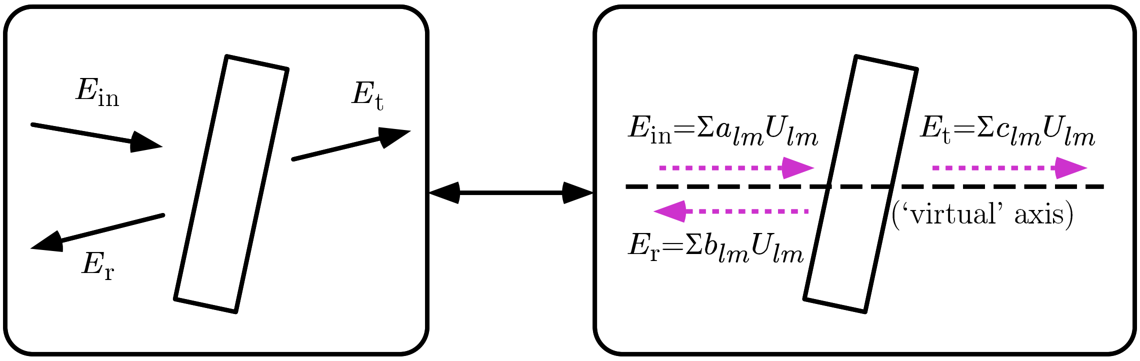

Figure 5.2: *A beam is illuminating the optical component (left). The fields can be expanded on a reference axis (right), thus the reflection and the transmission coefficient are matrices in this case.*

written as the vectors,

$$[E_{\rm in}] = [< lm + |E_{\rm in} >] \tag{5.22}$$

$$[E_{\rm r}] = [< lm - |E_{\rm r} >] \tag{5.23}$$

$$[E_{\rm t}] = [< lm + |E_{\rm t} >] \,. \tag{5.24}$$

The fields are related to each other by the linear transformations:

$$< ij - |E_{\rm r} > = \sum_{kl} r_{[ij,kl]} < kl + |E_{\rm in} > \tag{5.25}$$

$$< ij + |E_{\rm t} > = \sum_{kl} t_{[ij,kl]} < kl + |E_{\rm in} > \,. \tag{5.26}$$

The coefficients $r_{[ij,kl]}$ and $t_{[ij,kl]}$ are interpreted as the components of the matrices which have $\{lm\}$ and $\{pq\}$ as their row- and column-indices. Thus the coefficients of the optical components are represented as matrices [33]. These transmission and reflection matrices depend on the alignment and the matching.

5.5 Misalignment and Mismatching

As we have seen, a set of Hermite-Gaussian modes is characterized by a certain set of parameters, namely the propagation axis, the position of the waist, and the waist diameter. The difference of these parameters between the two modes is classified in two categories: the misalignment and the mismatching.

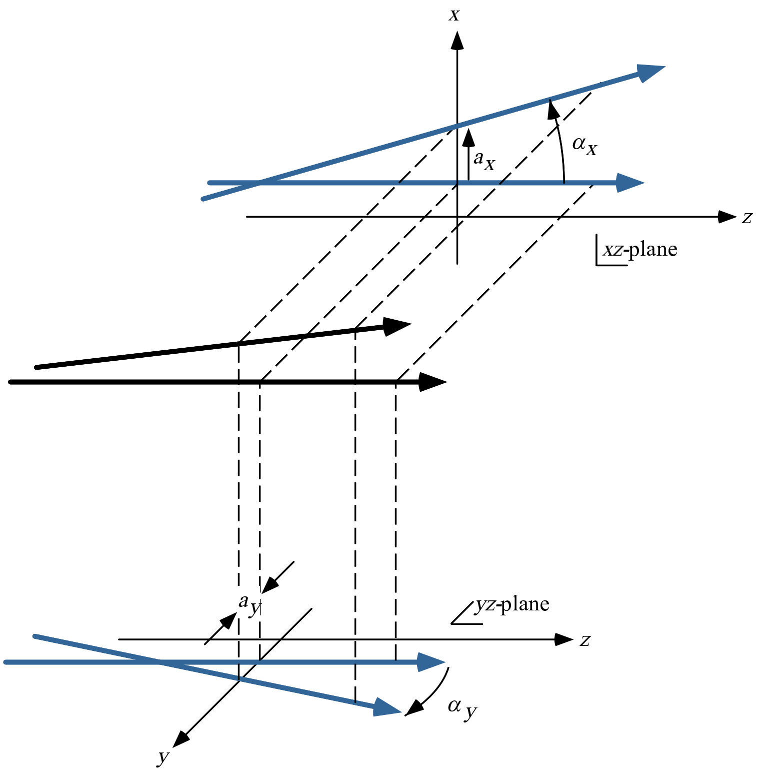

Figure 5.3: *Four parameters which characterize the misalignment. Two are defined as the distance of the waists and the angle between the axes which are projected on the xz plane. The other two are defined similarly in the yz plane.*

Alignment is related to the off-axis difference between the two Gaussian fields. When the propagation axis of one of the fields has a parallel displacement (perpendicular to the propagation direction) or an angular tilt to the axis of the other, the two fields are misaligned. There are four parameters that represent the misalignment. Suppose that the fields are paraxial along the z axis. Consider the projection of the two axes on the xz plane (Fig. 5.3). The first parameter is the distance between the waists of the projected axes, and the second is their angle. The other two parameters are defined similarly in the yz plane.

Mode-matching is related to the on-axis difference between the two Gaussian fields. When the two fields have different waist radii or different waist positions along the axis, they are mismatched[3]. The difference of the waist radius δw, and the difference

[3]Even if they are aligned completely.

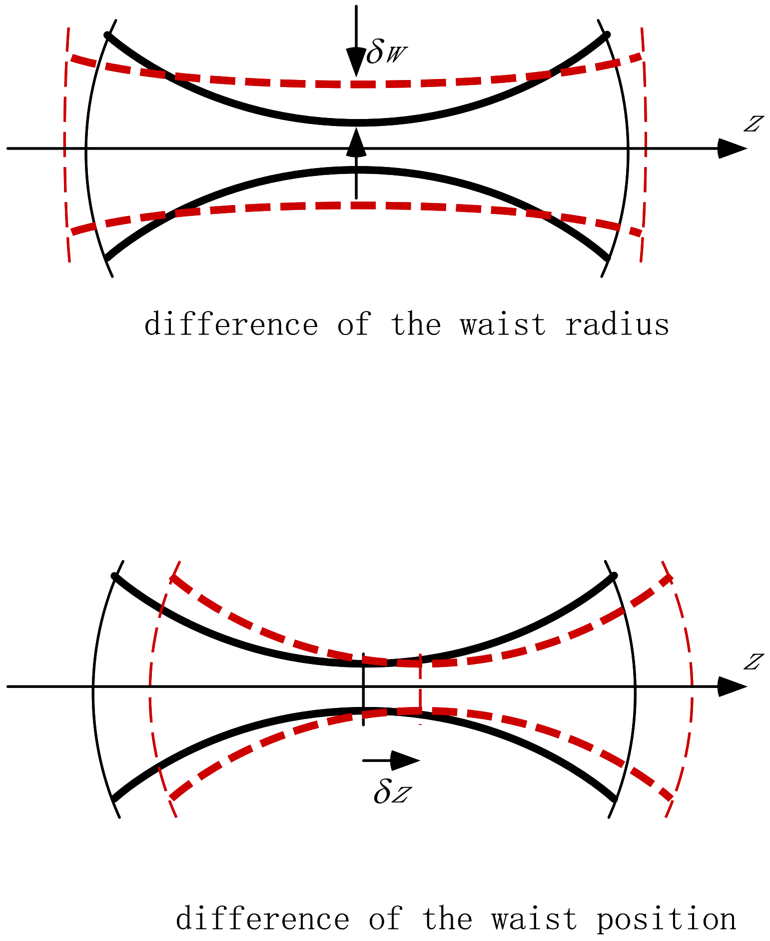

Figure 5.4: *Two parameters which characterize the mismatching. One is the difference of the waist radius δw, and the other is the difference of the position of the waist along the axis.*

of the waist position along the axis δz, are the parameters which describe the matching (Fig. 5.4). In a more general expression than Eqs. 5.2 and 5.3, it is possible that the projections of the mode profile on the xz and the yz planes have different waist positions and beam radii. Therefore the number of parameters that describe the matching are four.

In this paper, only the misalignment will be taken into account.

5.6 Modal Expansion of the Misaligned Beam

Any paraxial field is expanded by a set of Hermite-Gaussian modes. Therefore an Hermite-Gaussian field can be expanded by another set of modes with different parameters [35–38]. Especially, a misaligned Gaussian beam is expanded by a set which is completely mode-matched to the misaligned field. We will discuss how the misaligned beam couples to the higher-order modes by means of the modal-expansion. We follow the calculation by Anderson [36] and Vinet [33], but in our case the second-order expansion is required. This will give the basis to evaluate the coupling between the laser beam and the cavity, or the two beams which are recombined in the Michelson type interferometer. Only the results are shown in this section to avoid overburdening the text with derivations of complicated equations. The detailed calculations are shown in Appendix A.

5.6.1 Lateral Displacement

Consider the two coordinate systems, (x, y, z) and (x', y', z'), which are related to each other by a small parallel displacement a_x:

$$(x', y', z') = (x - a_x, y, z). \tag{5.27}$$

A set of Hermite-Gaussian fields in (x, y, z) coordinate system are defined by Eqs. 5.2 and 5.3. Let us consider an Hermite-Gaussian beam on the z' axis, which is represented by $\{U'_{lm+}\}$ (Fig. 5.5). The prime symbol will always be used to specify the coordinate system in this paper:

$$U'_{lm+} \equiv U_{lm+}(x', y', z'). \tag{5.28}$$

If the displacement a_x is much smaller than the waist radius w_0, we can expand the beam U'_{lm} by the set $\{U_{lm}\}$ to the second order of the displacement as

$$\begin{aligned} U_{lm+}(x', y', z') &= U_{lm+}(x - a_x, y, z) \\ &\simeq U_{lm+}(x, y, z) - \frac{d}{dx} U_{lm+}(x, y, z) a_x + \frac{1}{2}\frac{d^2}{dx^2} U_{lm+}(x, y, z) a_x^2 \\ &\equiv \sum_{pq} < pq + | lm+' > U_{pq+} \end{aligned} \tag{5.29}$$

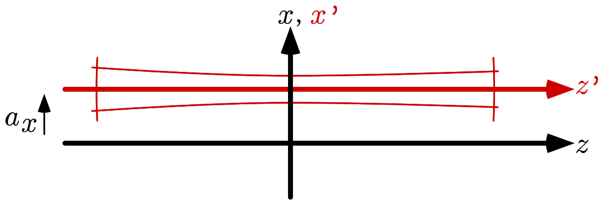

Figure 5.5: *Parallel displacement of the beam.*

where the expansion coefficient $< pq + |lm+' >$ is defined by

$$
\begin{aligned}
< pq + |lm+' > &\equiv \iint U^*_{pq+}(x,y,z) U_{lm+}(x',y',z') dxdy \\
&\simeq \iint \left[U_{lm+} + \frac{d}{dx} U_{lm+} a_x + \frac{1}{2} \frac{d^2}{dx^2} U_{lm+} a_x^2 \right] U^*_{pq+} dxdy \quad (5.30)
\end{aligned}
$$

On the assumption that $1 >> a_x/w_0$ and the input beam is the fundamental Gaussian beam in an arbitrary coordinate system, we can neglect the power translation to the modes higher than first off-axis mode (see Appendix A). After carrying out the above expansion, we obtain the expression for the laterally misaligned modes as

$$
P_x(a_x) * U_{00+}(x,y,z) \simeq \left[1 - \frac{1}{2} \left(\frac{a_x}{w_0} \right)^2 \right] U_{00+} + \frac{a_x}{w_0} U_{10+} \quad (5.31)
$$

$$
P_x(a_x) * U_{10+}(x,y,z) \simeq \left[1 - \frac{3}{2} \left(\frac{a_x}{w_0} \right)^2 \right] U_{10+} - \frac{a_x}{w_0} U_{00+} \quad (5.32)
$$

From the above expressions, we can see that $(a_x/w_0)^2$ is the order of the optical power that is transferred from one mode to others by the parallel transport.

5.6.2 Angular Tilt

Suppose that there is an angular tilt α_x between the beam and the z axis (Fig. 5.6). In this case, the two coordinate systems are related to each other as

$$
\begin{pmatrix} x' \\ z' \end{pmatrix} = \begin{pmatrix} \cos\alpha_x & -\sin\alpha_x \\ \sin\alpha_x & \cos\alpha_x \end{pmatrix} \begin{pmatrix} x \\ z \end{pmatrix} \quad (5.33)
$$

$$
y' = y. \quad (5.34)
$$

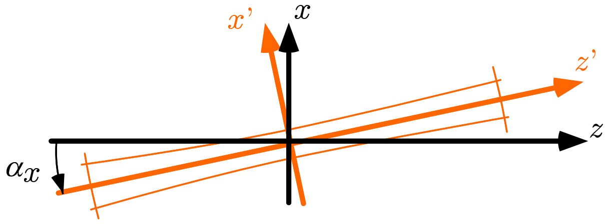

Figure 5.6: *Angular tilt of the beam.*

In the same way as the parallel displacement, we can neglect the modes higher than the first off-axis mode on condition that the inequality $1 >> \alpha_x/\alpha_0 >> \alpha_0$ is satisfied. The misaligned beams are expanded by the Hermite-Gaussian modes of the tilted coordinates to the second order of the perturbation as

$$R_x(\alpha_x) * U_{00+}(x, y, z) \simeq \left[1 - \frac{1}{2}\left(\frac{\alpha_x}{\alpha_0}\right)^2\right] U_{00+} - i\frac{\alpha_x}{\alpha_0} U_{10+} \tag{5.35}$$

$$R_x(\alpha_x) * U_{10+}(x, y, z) \simeq \left[1 - \frac{3}{2}\left(\frac{\alpha_x}{\alpha_0}\right)^2\right] U_{10+} - i\frac{\alpha_x}{\alpha_0} U_{00+} \tag{5.36}$$

For the angular tilt, $(\alpha_x/\alpha_0)^2$ is the order of the optical power which is transferred from one mode to others.

5.6.3 Parallel Displacement Along the Optical Axis

The parallel displacement along the optical axis has the first-order coupling to the $n = 2$ or higher order modes (Refs. 36, 39, and 40):

$$\begin{aligned} P_z(\delta z) * U_{00+}(x, y, z) &\equiv U_{00+}(x, y, z - \delta z) \\ &= U_{00+}(x, y, z) \exp iK\delta z + O\left(\frac{\delta z}{z_0}\right) \times (l + m = 2 \text{ terms}) \\ &\quad + O\left(\frac{\delta z^2}{z_0^2}\right) \end{aligned} \tag{5.37}$$

$$\begin{aligned} P_z(\delta z) * U_{10+}(x, y, z) &\equiv U_{10+}(x, y, z - \delta z) \\ &= U_{10+}(x, y, z) \exp iK\delta z + O\left(\frac{\delta z}{z_0}\right) \times (l + m = 3 \text{ terms}) \\ &\quad + O\left(\frac{\delta z^2}{z_0^2}\right). \end{aligned} \tag{5.38}$$

Here we do not take the mismatching effect into account. In such cases, the displacement δz is the second-order term of a_x and α_x. Therefore we do not have to make the second-order perturbation calculation.

5.6.4 Matrix Representation of a Misalignment-Operator

We have seen that the field which propagates the forward direction can be considered as the linear combination of only U_{00+} and U_{10+} modes, so far as we do not take the mismatching effect into account. Thus any paraxial field is represented as the two-rows vector as

$$[E_+] = \begin{pmatrix} <00+|E+> \\ <10+|E+> \end{pmatrix}. \tag{5.39}$$

The operators we have calculated are written in the matrix form as:

$$[P_x(a_x)]_+ = \begin{pmatrix} 1-\frac{1}{2}\left(\frac{a_x}{w_0}\right)^2 & -\frac{a_x}{w_0} \\ \frac{a_x}{w_0} & 1-\frac{3}{2}\left(\frac{a_x}{w_0}\right)^2 \end{pmatrix} \tag{5.40}$$

$$[R_x(\alpha_x)]_+ = \begin{pmatrix} 1-\frac{1}{2}\left(\frac{\alpha_x}{\alpha_0}\right)^2 & -i\frac{\alpha_x}{\alpha_0} \\ -i\frac{\alpha_x}{\alpha_0} & 1-\frac{3}{2}\left(\frac{\alpha_x}{\alpha_0}\right)^2 \end{pmatrix} \tag{5.41}$$

$$[P_z(\delta z)]_+ = e^{iK\delta z}\begin{pmatrix} 1 & 0 \\ 0 & 1 \end{pmatrix} \tag{5.42}$$

From Eqs 5.10, 5.11, and 5.12, it is apparent that the matrices for the back-propagating fields are defined as

$$[P_x(a_x)]_- = [P_x(a_x)]_+^* \tag{5.43}$$

$$[R_x(\alpha_x)]_- = [R_x(\alpha_x)]_+^* \tag{5.44}$$

$$[P_z(\delta_z)]_- = [P_z(\delta_z)]_+^* . \tag{5.45}$$

5.7 Matrices of the Misaligned Optical Components

We will calculate the expression for the matrices of the misaligned optical components to the second order of the perturbation. We confine ourselves to the two-dimensional

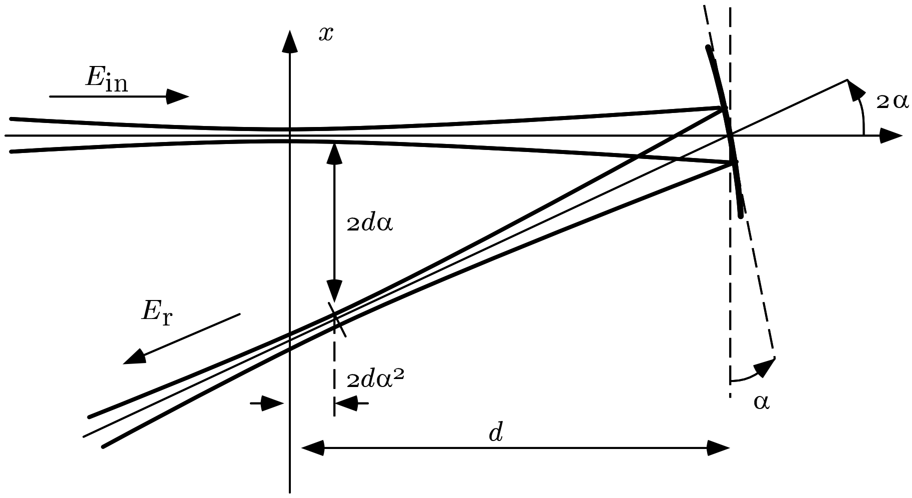

Figure 5.7: *A mirror is reflecting the incoming beam. Because the radius of curvature of the mirror is completely matched to the wavefront, the waist radius is conserved.*

case for simplicity. In such a situation, it is possible to take into account only the fundamental and first off-axis mode (see Appendix A for the details). The transmission and reflection coefficient are the 2×2 matrices, and the field is expressed as the vector which has two rows.

5.7.1 Modal Expansion

To calculate the transmission and the reflection coefficient of the optical components, it is necessary to expand the misaligned beam by a set of the Hermite-Gaussian modes. Here only the results of the expansions are shown. For the detailed calculations, see Appendix A.

5.7.2 Misalignment of the Mirror

Suppose that a mirror is reflecting an incoming laser beam whose field is the $(l+m)$th order Hermite-Gaussian field, $E_{\mathrm{in}} = U_{lm+}$. We will neglect the mismatching effect, *i.e.*, the radius of curvature of the mirror and the wavefront are equal to each other at the reflection point (Fig. 5.7). Thus the reflected beam is the $(l+m)$th order Hermite-

Gaussian field on another axis with the same waist radius as the input, which is written as U'_{lm-}. When the mirror has an angular rotation α, the reflected field is expressed as

$$\begin{aligned} E_{\rm r} &= rU'_{lm-}\exp 2i[-Kd+(l+m+1)\eta(d)] \\ &= r\left\{P_z[d(1-\cos 2\alpha)] * P_x(-d\sin 2\alpha) * R_x(2\alpha) * U_{lm-}\right\} \\ &\quad \times \exp 2i[-Kd+(l+m+1)\eta(d)] \end{aligned} \tag{5.46}$$

where r is the reflection coefficient of the mirror, d is the distance between the waist and the mirror, and P_z is a parallel displacement operator along the z axis. Since the phase of the field must be continuous[4], the phase factor $\exp 2i[-Kd+(l+m+1)\eta(d)]$ appears in the above expression.

By using Eqs. 5.43, 5.44, 5.45, and 5.46, the following equation is obtained:

$$\begin{aligned} [E_{\rm r}] &= re^{2i[-Kd+\eta(d)]}\begin{pmatrix} 1 & 0 \\ 0 & e^{2i\eta(d)} \end{pmatrix}[P_z(2\alpha^2 d)]_-[P_x(-2d\alpha)]_-[R_x(2\alpha)]_-[E_{\rm in}] \\ &= re^{2i[-Kd+\eta(d)-2d\alpha^2/z_0\alpha_0^2]}\begin{pmatrix} 1 & 0 \\ 0 & e^{2i\eta(d)} \end{pmatrix} \\ &\quad \times \begin{bmatrix} 1-2\frac{\alpha^2}{\alpha_0^2}\left(1+\frac{d^2}{z_0^2}-2i\frac{d}{z_0}\right) & 2i\frac{\alpha}{\alpha_0}\left(1-i\frac{d}{z_0}\right) \\ 2i\frac{\alpha}{\alpha_0}\left(1+i\frac{d}{z_0}\right) & 1-2\frac{\alpha^2}{\alpha_0^2}\left(3+3\frac{d^2}{z_0^2}+2i\frac{d}{z_0}\right) \end{bmatrix}[E_{\rm in}]\,. \end{aligned} \tag{5.47}$$

The imaginary part in the diagonal terms can be neglected, because it does not affect the power of the field $I_{\rm r} = |E_{\rm r}|^2$ to the second order of perturbation. The reflection coefficient is thus approximated as

$$\begin{aligned} [r] &= re^{2i[-Kd+\eta(d)-2d\alpha^2/z_0\alpha_0^2]}\begin{pmatrix} 1 & 0 \\ 0 & e^{2i\eta(d)} \end{pmatrix} \\ &\quad \times \begin{bmatrix} 1-2\frac{\alpha^2}{\alpha_0^2}\left(1+\frac{d^2}{z_0^2}\right) & 2i\frac{\alpha}{\alpha_0}\left(1-i\frac{d}{z_0}\right) \\ 2i\frac{\alpha}{\alpha_0}\left(1+i\frac{d}{z_0}\right) & 1-2\frac{\alpha^2}{\alpha_0^2}\left(3+3\frac{d^2}{z_0^2}\right) \end{bmatrix} \end{aligned} \tag{5.48}$$

The transmitted beam is not affected by the mirror (we neglect the lens effect of the mirror), therefore the transmission coefficient of the mirror is represented as the

[4]All of the phase discontinuity between the input and the reflected field must be from the reflection coefficient of the amplitude of the field.

unit matrix times the conventional transmission coefficient:

$$[t] = t \begin{pmatrix} 1 & 0 \\ 0 & 1 \end{pmatrix}. \tag{5.49}$$

Sometimes it is convenient to neglect the Gouy phase shift for the fundamental mode, therefore we will write Eq. 5.47 as

$$[r] = re^{-2id[K+2\alpha^2/z_0\alpha_0^2]} \begin{pmatrix} 1 & 0 \\ 0 & e^{2i\eta(d)} \end{pmatrix} \begin{bmatrix} 1 - 2\frac{\alpha^2}{\alpha_0^2}\left(1 + \frac{d^2}{z_0^2}\right) & 2i\frac{\alpha}{\alpha_0}\left(1 - i\frac{d}{z_0}\right) \\ 2i\frac{\alpha}{\alpha_0}\left(1 + i\frac{d}{z_0}\right) & 1 - 2\frac{\alpha^2}{\alpha_0^2}\left(3 + 3\frac{d^2}{z_0^2}\right) \end{bmatrix}. \tag{5.50}$$

5.7.3 Misalignment of the Fabry-Perot Cavity

It is possible to get the reflection coefficient matrix of the Fabry-Perot cavity by using Eq. 5.47 or Eq. 5.50 directly. However, it is simpler to use the reflection coefficients for the respective modes to build the matrix. The reflection coefficient for the fundamental mode of the cavity is

$$r_{\mathrm{c}0}(\Omega) \equiv r_{\mathrm{c}}(\Omega), \tag{5.51}$$

where Ω is the frequency of the field and r_{c} is defined by Eq. 4.4. For the first off-axis mode, the reflection coefficient is

$$r_{\mathrm{c}1}(\Omega) \equiv r_{\mathrm{c}}(\Omega - 2\pi\nu_{\mathrm{G}}), \tag{5.52}$$

where ν_{G} is represented by Eq. 5.17. Therefore, in the coordinate system where the cavity axis lies on the z axis, the reflection matrix is written as

$$[r_{\mathrm{c}}]_{\mathrm{aligned}} = \begin{pmatrix} r_{\mathrm{c}0} & 0 \\ 0 & r_{\mathrm{c}1} \end{pmatrix}. \tag{5.53}$$

To obtain the reflection coefficient matrix in a general coordinate system, first we have to expand the input beam in terms of the cavity modes. Equation 5.53 is used to get the reflection field in the cavity's coordinate system. Finally the reflected field is expanded in terms of the modes on the desired coordinate system. By comparing the input and the reflected field, we will get the elements of the matrix.

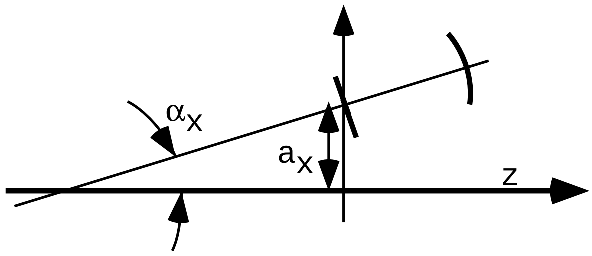

Figure 5.8: *Misalignment of the cavity. The angle between the cavity axis and the z axis is α_x.*

Suppose that the angle between the cavity axis and the reference is α_x, and the waist of the cavity is on $(a_x, 0)$ in the xz-coordinate. The cavity axis is on the z' axis in the $x'z'$ coordinate. If the cavity comprises the flat mirror and the concave mirror, the axis of the cavity is perpendicular to the flat mirror, and it lies on the center of curvature of the concave mirror. The radius of curvature of the mirrors are well matched to the wavefront, thus the reflected beam has the same waist radius as the input (Fig. 5.8). The input field $E_{\rm in}$ is expressed in the $x'z'$-coordinate as

$$[E_{\rm in}]' = [R'_x(-\alpha_x)]_+[P'_x(-a_x)]_+[E_{\rm in}] \tag{5.54}$$

where $[E_{\rm in}]$ and $[E_{\rm in}]'$ are the vector representation of the field in the xz- and $x'z'$-coordinate, and R'_x and P'_x are the rotation and the displacement operator in the $x'z'$-coordinate system, respectively. The reflection field is then written by using Eq. 5.53 as

$$\begin{aligned}[E_{\rm r}]' &= [r_{\rm c}]_{\rm aligned}[E_{\rm in}]' \\ &= [r_{\rm c}]_{\rm aligned}[R'_x(-\alpha_x)]_+[P'_x(-a_x)]_+[E_{\rm in}]. \end{aligned} \tag{5.55}$$

In the xz coordinate system, this is represented as

$$\begin{aligned}[E_{\rm r}] &= [P_x(a_x)]_-[R_x(\alpha_x)]_-[E_{\rm r}]' \\ &= [P_x(a_x)]_-[R_x(\alpha_x)]_-[r_{\rm c}]_{\rm aligned}[R'_x(-\alpha_x)]_+[P'_x(-a_x)]_+[E_{\rm in}]. \end{aligned} \tag{5.56}$$

The reflection matrix in the xz coordinate is defined as

$$[r_{\rm c}(\omega)] \equiv [P_x(a_x)]_-[R_x(\alpha_x)]_-[r_{\rm c}(\omega)]_{\rm aligned}[R'_x(-\alpha_x)]_+[P'_x(-a_x)]_+$$

$$\equiv \begin{bmatrix} M_{00} & M_{01} \\ M_{10} & M_{11} \end{bmatrix} \tag{5.57}$$

with

$$M_{00} \equiv r_{c0} - \frac{a_x^2}{w_0^2}(r_{c0} - r_{c1}) - \frac{\alpha_x^2}{\alpha_0^2}(r_{c0} + r_{c1}) - 2i\frac{a_x}{w_0}\frac{\alpha_x}{\alpha_0}(r_{c0} + r_{c1}) \tag{5.58}$$

$$M_{01} \equiv \frac{a_x}{w_0}(r_{c0} - r_{c1}) + i\frac{\alpha_x}{\alpha_0}(r_{c0} + r_{c1}) \tag{5.59}$$

$$M_{10} \equiv \frac{a_x}{w_0}(r_{c0} - r_{c1}) + i\frac{\alpha_x}{\alpha_0}(r_{c0} + r_{c1}) \tag{5.60}$$

$$M_{11} \equiv r_{c1} - \frac{a_x^2}{w_0^2}(3r_{c1} - r_{c0}) - \frac{\alpha_x^2}{\alpha_0^2}(3r_{c1} + r_{c0}) + 2i\frac{a_x}{w_0}\frac{\alpha_x}{\alpha_0}(r_{c0} + r_{c1})\,. \tag{5.61}$$

The imaginary part in the diagonal terms ($2ia_x\alpha_x/w_0\alpha_0$ term) can be neglected, because it does not affect the power of the field $|E_{\mathrm{r}}|^2$ to the second order of perturbation. Thus, the reflection matrix is simplified as

$$[r_{\mathrm{c}}(\omega)] = \begin{bmatrix} r_{c0} - \frac{a_x^2}{w_0^2}(r_{c0} - r_{c1}) - \frac{\alpha_x^2}{\alpha_0^2}(r_{c0} + r_{c1}) & \frac{a_x}{w_0}(r_{c0} - r_{c1}) + i\frac{\alpha_x}{\alpha_0}(r_{c0} + r_{c1}) \\ \frac{a_x}{w_0}(r_{c0} - r_{c1}) + i\frac{\alpha_x}{\alpha_0}(r_{c0} + r_{c1}) & r_{c1} - \frac{a_x^2}{w_0^2}(3r_{c1} - r_{c0}) - \frac{\alpha_x^2}{\alpha_0^2}(3r_{c1} + r_{c0}) \end{bmatrix}. \tag{5.62}$$

Note that the matrix has the different dependence on the angle- and the displacement-misalignment. For example, if the length of the cavity is tuned to the fundamental mode of the field, $r_{c0}(\omega)$ is the positive real number. In this case, the first off-axis mode is out of resonance, thus $r_{c1}(\omega)$ is approximately equal to -1. The cavity is more sensitive to the misalignment of the lateral displacement which is proportional to $r_{c0} + 1$ than the angular misalignment which is proportional to $r_{c0} - 1$.

On the other hand, if neither the fundamental nor the off-axis mode is resonant with the cavity, both r_{c0} and r_{c1} are approximately equal to -1. Therefore the cavity is sensitive to the angular misalignment, and insensitive to the misalignment of the lateral displacement.

5.8 The Frequency Noise and the Misalignment of the Cavity

Suppose that the input field has a frequency fluctuation. The field is expressed by the sum of the carrier and the sidebands of the frequency noise with a vector form as

$$\begin{aligned} [E_{\mathrm{in}}(t)] &= e^{i\Omega t}\left[1+i\phi(t)\right][E_0] \\ &= e^{i\Omega t}\left[1+i\int\frac{2\pi\delta\tilde{\nu}(\omega)}{i\omega}e^{i\omega t}d\omega\right][E_0] \end{aligned} \tag{5.63}$$

where $[E_0]$ is a constant vector. The reflected field is written by using Eq. 5.62 as

$$\begin{aligned} [E_{\mathrm{r}}] &= e^{i\Omega t}\left\{[r_{\mathrm{c}}(\Omega)]+i\int\frac{2\pi\delta\tilde{\nu}(\omega)}{i\omega}e^{i\omega t}\left[r_{\mathrm{c}}(\Omega+\omega)\right]d\omega\right\}[E_0] \\ &\equiv e^{i\Omega t}\left[A(t)\right][E_0] \end{aligned} \tag{5.64}$$

where $[A]$ is a matrix which represents the effects of the misalignment and the frequency noise. Suppose that only the fundamental mode is resonant with the cavity, thus the reflection coefficient for the off-axis mode is approximated as a constant:

$$r_{\mathrm{c}1}(\omega)\simeq r_{\mathrm{c}0}(-2\pi\nu_{\mathrm{G}})\simeq -1 \tag{5.65}$$

Under this assumption, each of the elements of the matrix $[A]$ is calculated as follows:

$$\begin{aligned} A_{00}(t) &= r_{\mathrm{c}0}(0)\left(1-\frac{a_x^2}{w_0^2}-\frac{\alpha_x^2}{\alpha_0^2}\right)\left[1+i\phi(t)-i\Psi_{\mathrm{FP}}^{\phi}(t)\right]-\left(\frac{a_x^2}{w_0^2}-\frac{\alpha_x^2}{\alpha_0^2}\right)\left[1+i\phi(t)\right] \\ &= r_{\mathrm{c}0}(0)\left[1-\frac{a_x^2}{w_0^2}\left(1+\frac{1}{r_{\mathrm{c}0}(0)}\right)-\frac{\alpha_x^2}{\alpha_0^2}\left(1-\frac{1}{r_{\mathrm{c}0}(0)}\right)\right] \\ &\quad\times\left\{1+i\phi(t)-i\Psi_{\mathrm{FP}}^{\phi}(t)\left[1+\frac{1}{r_{\mathrm{c}0}(0)}\left(\frac{a_x^2}{w_0^2}-\frac{\alpha_x^2}{\alpha_0^2}\right)\right]\right\} \end{aligned} \tag{5.66}$$

$$\begin{aligned} A_{01}(t) &= A_{10}(t) \\ &= r_{\mathrm{c}0}(0)\left\{\begin{array}{l}\left[\left(1+\frac{1}{r_{\mathrm{c}0}(0)}\right)\frac{a_x}{w_0}-\left(1-\frac{1}{r_{\mathrm{c}0}(0)}\right)\frac{\alpha_x}{\alpha_0}\phi(t)+\frac{\alpha_x}{\alpha_0}\Psi_{\mathrm{FP}}^{\phi}(t)\right] \\ +i\left[\left(1+\frac{1}{r_{\mathrm{c}0}(0)}\right)\frac{a_x}{w_0}\phi(t)+\left(1-\frac{1}{r_{\mathrm{c}0}(0)}\right)\frac{\alpha_x}{\alpha_0}-\frac{a_x}{w_0}\Psi_{\mathrm{FP}}^{\phi}(t)\right]\end{array}\right\} \end{aligned} \tag{5.67}$$

$$\begin{aligned} A_{11}(t) &= -\left[1-\frac{a_x^2}{w_0^2}\left(3+r_{\mathrm{c}0}(0)\right)-\frac{\alpha_x^2}{\alpha_0^2}\left(3-r_{\mathrm{c}0}(0)\right)\right] \\ &\quad\times\left[1+i\phi(t)+i\Psi_{\mathrm{FP}}^{\phi}(t)r_{\mathrm{c}0}(0)\left(\frac{a_x^2}{w_0^2}-\frac{\alpha_0^2}{\alpha_0^2}\right)\right] \end{aligned} \tag{5.68}$$

where $\Psi^{\phi}_{\mathrm{FP}}(t)$ is the additional phase shift caused by the cavity which is defined by Eq. 4.31. Comparing Eqs. 4.27 and 4.31 with Eqs. 5.64 and 5.66, one can see that not only the amplitude but also the phase of the fundamental mode in the reflected field is changed by the misalignment. This is because the cavity have the different responses to the fundamental and off-axis mode when it is tuned to the fundamental mode.

On the other hand, when both the fundamental and first off-axis mode are off-resonant with the cavity, the reflection coefficient of the cavity for the two modes are considered as constant;

$$r_{\mathrm{c0}}(\omega)\Big|_{\mathrm{off-resonant}} \simeq r_{\mathrm{c1}}(\omega)\Big|_{\mathrm{off-resonant}} \simeq -1\,. \tag{5.69}$$

The matrix $A(t)$ is written as

$$[A(t)]\Big|_{\mathrm{off-resonant}} \simeq -\left\{1+i\phi(t)\right\}\begin{bmatrix} 1-2\frac{\alpha_x^2}{\alpha_0^2} & 2i\frac{\alpha_x}{\alpha_0} \\ 2i\frac{\alpha_x}{\alpha_0} & 1-2\frac{a_x^2}{w_0^2}-4\frac{\alpha_x^2}{\alpha_0^2} \end{bmatrix}. \tag{5.70}$$

Because the response of the cavity for the two modes are the same, only the amplitude of the reflected field is changed by the misalignment.

6. Fabry-Perot-Michelson Interferometer

We will study a Fabry-Perot-Michelson interferometer as an example of the realistic detector.

6.1 Fabry-Perot-Michelson Interferometer Used as a Gravitational Wave Detector

A Fabry-Perot-Michelson (FPM) interferometer is a Michelson interferometer which has a Fabry-Perot cavity in each of its arms to fold the optical path (Fig. 6.1). We will call the FP cavity which is placed along the input beam as the parallel cavity, and the cavity which is set perpendicular to the input beam as the perpendicular cavity. To distinguish the physical quantities of the parallel and the perpendicular cavity, we will attach the index "1" to the former and "2" to the latter ($r_{\rm f2}$ represents the reflection coefficient of the front mirror of the perpendicular cavity, for example) [1]. The sign of the reflection coefficients of the mirrors of the cavity are chosen to be plus inside the cavity. The reflection coefficient of the beamsplitter is plus on the side which faces the parallel cavity.

When the gravitational radiation passes the interferometer, it produces the phase shifts in the fields in the two optical paths, which have the same amplitude and the opposite sign. In general, the reflected field from the parallel and the perpendicular

[1] Most of the symbols used here have been defined in the preceding sections; $t_{\rm b}$ represents the transmission coefficient of the beamsplitter, *etc.* We will not write down their definition again. Only the definition of the newly introduced symbols will be presented.

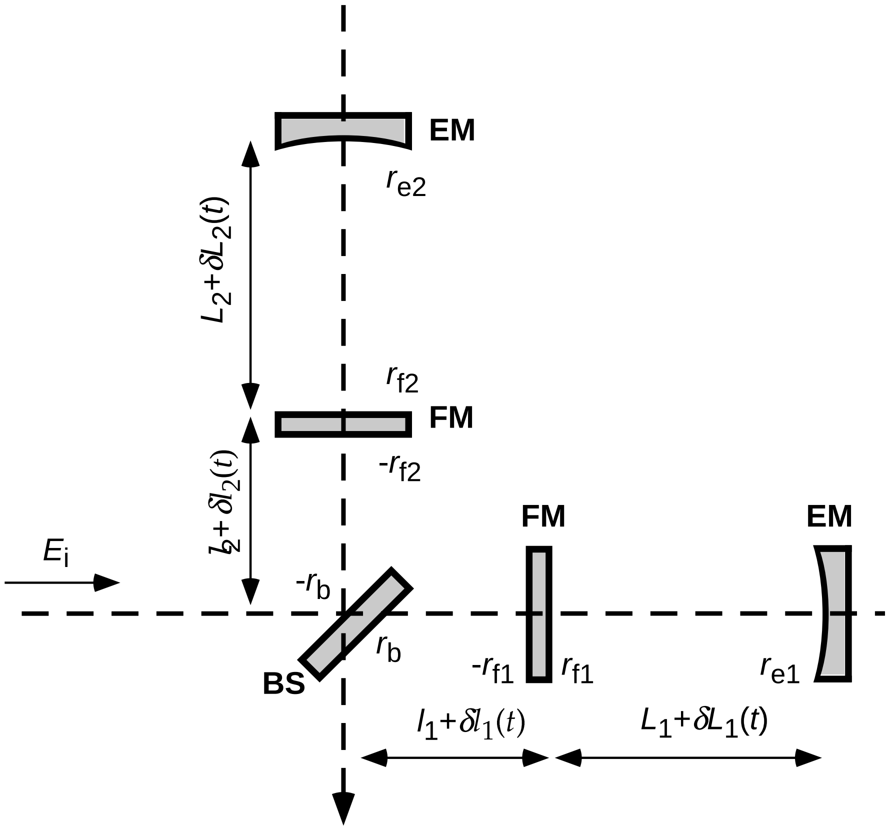

Figure 6.1: *A conceptual view of a Fabry-Perot-Michelson interferometer. BS, beamsplitter; FM, front mirror; EM, end mirror. The signs of the transmission coefficient of the mirrors and the beamsplitter are defined in this figure.*

arm are written as

$$\begin{aligned}
E_1(t) &= E_0 t_{\mathrm{b}} r_{\mathrm{c1}}(\Omega) \exp i\Big[\Omega t - \theta_{\mathrm{o1}} + \delta\phi(t - 2l_1/c) - \delta\theta_{\mathrm{GR1}}(t) - \delta\theta_{l1}(t) \\
&\quad -\delta\Psi^{\mathrm{GR}}_{\mathrm{FP1}}(t - l_1/c) - \delta\Psi^{\mathrm{L}}_{\mathrm{FP1}}(t - l_1/c) - \delta\Psi^{\phi}_{\mathrm{FP1}}(t - l_1/c)\Big] \\
&= E_0 t_{\mathrm{b}} r_{\mathrm{c1}}(\Omega) \exp i(\Omega t - \theta_{\mathrm{o1}} - \delta\theta_1(t) - \delta\Psi_1(t)) \qquad (6.1) \\
E_2(t) &= E_0 r_{\mathrm{b}} r_{\mathrm{c2}}(\Omega) \exp i\Big[\Omega t - \theta_{\mathrm{o2}} + \delta\phi(t - 2l_2/c) - \delta\theta_{\mathrm{GR2}}(t) - \delta\theta_{l2}(t) \\
&\quad -\delta\Psi^{\mathrm{GR}}_{\mathrm{FP2}}(t - l_2/c) - \delta\Psi^{\mathrm{L}}_{\mathrm{FP2}}(t - l_2/c) - \delta\Psi^{\phi}_{\mathrm{FP2}}(t - l_2/c)\Big] \\
&\equiv E_0 r_{\mathrm{b}} r_{\mathrm{c2}}(\Omega) \exp i(\Omega t - \theta_{\mathrm{o2}} - \delta\theta_2(t) - \delta\Psi_2(t)) \qquad (6.2)
\end{aligned}$$

in front of the beamsplitter, where $\theta_{\mathrm{o}i}$ $(i = 1, 2)$ are the static phase delay, $\delta\theta_i$ are the phase fluctuations which are produced in the paths between the beamsplitter and the front mirrors, and $\delta\Psi_i$ represent the fluctuations which are produced in the cavities. Other symbols in the above equation are defined in the preceding sections. It is possible to detect the effect of the gravitational radiation by measuring the phase of the two field precisely.

6.2 Extraction of the Signal

To extract the signal from the interferometer, various kind of techniques have been developed. Let us assume that we want to measure the phase of the field which has the fluctuation of the amplitude and the phase at the same time. When the fluctuation is small enough, the field is written as

$$\begin{aligned}
E_{\mathrm{sig}}(t) &= [1 + \delta a(t)] \exp i\,[\Omega t + \delta\phi(t)] \\
&\simeq [1 + \delta a(t) + i\delta\phi(t)] \exp i\Omega t \qquad (6.3)
\end{aligned}$$

to the first order of the fluctuations, where $\delta a(t)$ and $\delta\phi(t)$ represent the small fluctuation in the amplitude and the phase, respectively. We call this field as the 'target field' tentatively, because the aim of the measurement is to detect the phase of this field.

The phase of the target field is measured by using another oscillator as the phase-reference. Without losing generality, the field of the reference oscillator is written as

$$E_{\mathrm{ref}}(t) = b_{\mathrm{ref}}(t) \exp i\,[\Omega t + \phi_{\mathrm{ref}}(t)] \qquad (6.4)$$

where $b_{\rm ref}(t)$ and $\phi_{\rm ref}(t)$ are the arbitrary real functions.

The idea of the phase detection is to 'mix' the target field and the reference field to correct the cross-terms of these fields. For this purpose, the field of the target and the reference are added to give the intensity;

$$\begin{aligned} I(t) &= |E_{\rm sig}(t) + E_{\rm ref}(t)|^2 \\ &= |E_{\rm sig}(t)|^2 + |E_{\rm ref}(t)|^2 + [E_{\rm sig}(t)E^*_{\rm ref}(t) + \text{c.c.}] \,. \end{aligned} \tag{6.5}$$

By using some techniques which will be described later, only the cross-terms are selected as the signal;

$$\begin{aligned} I_{\rm cross}(t) &= E_{\rm sig}(t)E^*_{\rm ref}(t) + \text{c.c.} \\ &= 2b_{\rm ref}(t)\Big\{ [1+\delta a(t)]\cos\phi_{\rm ref}(t) + \delta\phi(t)\sin\phi_{\rm ref}(t)\Big\}. \end{aligned} \tag{6.6}$$

When the relative phase of the reference and the signal field are quadrature, *i.e.*

$$\phi_{\rm ref}(t) = \left(n + \frac{1}{2}\right)\pi \tag{6.7}$$

where n is an integer, it is apparent that only the term which is proportional to the phase of the signal field is detected;

$$I_{\rm cross}(t) = (-1)^n 2b_{\rm ref}(t)\delta\phi(t). \tag{6.8}$$

Since we know the waveform of the reference, it is possible to reconstruct the waveform of the phase $\delta\phi(t)$ from the above expression in principle.

To summarize, for the phase measurement of the target field, we have to introduce a reference which have the quadrature phase to the target. The field of the target and the reference are added and detected as the intensity. Only the cross-terms of the target and the reference are selected as the signal which is proportional to the phase of the target field. Even if the target has the amplitude fluctuation, it will not be detected.

If the frequency of the target and the reference are the same (*i.e.* $b_{\rm ref}(t)$ is a constant), the detection procedure is called the homodyne detection. If we use a frequency-shifted field as the reference (for example, $b_{\rm ref}(t) \propto \sin\omega_{\rm ref}t$), it is called the heterodyne detection. First we will study the pre-modulation as an example of the heterodyne detection.

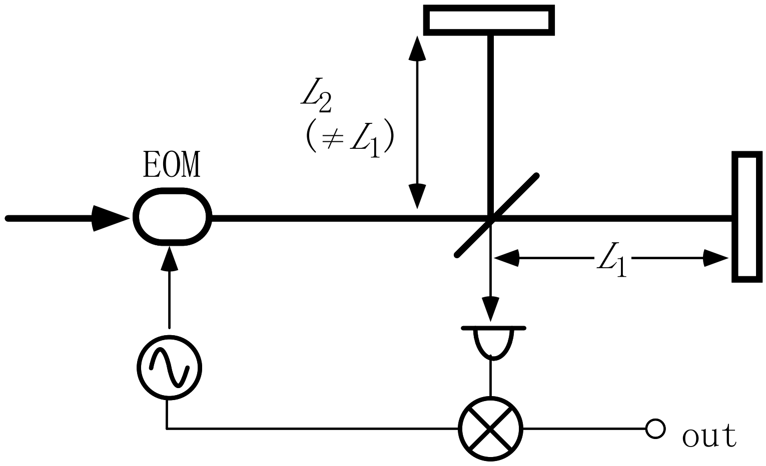

Figure 6.2: *A simple Michelson interferometer using the pre-modulation technique. There is a difference in two optical lengths which is large enough for the sidebands to be transmitted to the anti-symmetric port. The optical power in the anti-symmetric port is detected and mixed with the local oscillator to produce the signal which is proportional to the fluctuation of the phase-difference in two paths. Most of the optical power is reflected from the interferometer.*

6.2.1 Signal Extraction by Pre-Modulation

It is possible to sense the phase-difference between two optical paths by monitoring the anti-symmetric output of the interferometer using RF modulation technique, in the same way as Pound-Drever technique (see Sec. 4.2). The RF sidebands are used as the reference to measure the phase of the carrier. Several scheme have been developed (Refs. 41, 42) for this purpose, but we will study only the pre-modulation scheme. Phase modulation is applied to the input field of the interferometer. However, as one can see from Eq. 3.23, there will be no modulation sidebands as well as the carrier in the anti-symmetric port if the length between the beamsplitter and the front mirrors are equal to each other. In the pre-modulation configuration, the difference of the length between the two optical paths is large enough for the modulation sidebands to be transmitted to the anti-symmetric port of the interferometer even if there is no carrier transmitted (Fig. 6.2).

The phase-modulated input field is expressed in Eq. 4.34. The modulation frequency is chosen so that the sidebands are far from the resonance. The field of the anti-symmetric output is written in the form

$$E_{\rm anti} = E_0 t_{\rm b} r_{\rm b} e^{i\Omega t}\Big\{ e^{-i[\theta_{\rm o1}+\delta\theta_1(t)]}\Big[r_{\rm c1}(0)e^{-i\delta\Psi_1(t)} + imr_{\rm c}^{\rm SB}\sin(\omega_{\rm m}t - \theta_{\rm m1})\Big] - e^{-i[\theta_{\rm c2}+\delta\theta_2(t)]}\Big[r_{\rm c2}(0)e^{-i\delta\Psi_2(t)} + imr_{\rm c}^{\rm SB}\sin(\omega_{\rm m}t - \theta_{\rm m2})\Big]\Big\}, \quad (6.9)$$

where $\theta_{{\rm m}i}$ $(i = 1, 2)$ are the difference between the phase shift of the carrier and the sidebands which are produced between the beamsplitter and the near mirrors and $r_{\rm c}^{\rm SB}$ is the reflection coefficient of the cavity for the sidebands, respectively. The sidebands are out of resonance, therefore $r_{\rm c}^{\rm SB}$ is almost equal to unity and no phase fluctuation is added by the cavity:

$$r_{\rm c}^{\rm SB} \simeq -1. \quad (6.10)$$

The phase shift $\theta_{{\rm m}i}$ comprises the static term $2k_{\rm m}l_i$ and the fluctuation. However, $|\theta_{{\rm m}i}/\omega_{\rm m}|$ is about the same order of $|\theta_i/\Omega|$. This means that the fluctuation in $\theta_{{\rm m}i}$ has the same order of amplitude as $\theta_i\omega_{\rm m}/\Omega \sim 10^{-7}\theta_i$, assuming that the optical frequency and the modulation frequency are the order of several hundreds terahertz and several tens megahertz, respectively. Therefore we will neglect the fluctuation in $\theta_{{\rm m}i}$;

$$\theta_{{\rm m}i} \simeq 2k_{\rm m}l_i \, (i = 1, 2). \quad (6.11)$$

When we define the mean and the difference of the static part of the phase delay as

$$\overline{\theta}_{\rm o} \equiv \frac{\theta_{\rm o1}+\theta_{\rm o2}}{2} \quad (6.12)$$

$$\Delta\theta_{\rm o} \equiv \theta_{\rm o1}-\theta_{\rm o2} \quad (6.13)$$

and the common- and the differential-fluctuation of the phase as

$$\delta\theta_+ \equiv \delta\theta_1+\delta\theta_2 \quad (6.14)$$

$$\delta\theta_- \equiv \delta\theta_1-\delta\theta_2, \quad (6.15)$$

equation 6.9 is re-written as

$$E_{\rm anti} = E_0 t_{\rm b} r_{\rm b} e^{i(\Omega t-\overline{\theta}_{\rm o}-\delta\theta_+/2)}\Big\{ e^{-i\frac{\Delta\theta_{\rm o}+\delta\theta_-}{2}}\Big[r_{\rm c1}(0)e^{-i\delta\Psi_1} + imr_{\rm c}^{\rm SB}\sin(\omega_{\rm m}t - \theta_{\rm m1})\Big] - e^{i\frac{\Delta\theta_{\rm o}+\delta\theta_-}{2}}\Big[r_{\rm c2}(0)e^{-i\delta\Psi_2} + imr_{\rm c}^{\rm SB}\sin(\omega_{\rm m}t - \theta_{\rm m2})\Big]\Big\}. \quad (6.16)$$

The difference of the optical path lengths is controlled in such a way that the static part of the difference of the phase is an integer times 2π;

$$\begin{aligned}\Delta\theta_{\rm o} &= 2K(l_1 - l_2) \\ &= 2n\pi \end{aligned} \tag{6.17}$$

where n is an integer. The antisymmetric port is dark for the carrier, but a part of the sidebands still appears in the anti-symmetric port, even if there is no fluctuation (*i. e.* $\delta\theta_- = 0$). In this case, the intensity of the field is calculated from Eq. 6.16 as

$$\begin{aligned} I_{\rm anti} &= |E_{\rm anti}|^2 \\ &= I_0 T_{\rm b} R_{\rm b} \Big\{ \Big| r_{\rm c1} e^{-i\delta\Psi_1} + imr_{\rm c}^{\rm SB} \sin(\omega_{\rm m} t - \theta_{\rm m1}) \Big|^2 \\ &\qquad + \Big| r_{\rm c2} e^{-i\delta\Psi_2} + imr_{\rm c}^{\rm SB} \sin(\omega_{\rm m} t - \theta_{\rm m2}) \Big|^2 \\ &\qquad - e^{-i\delta\theta_-} \Big[r_{\rm c1} e^{-i\delta\Psi_1} + imr_{\rm c}^{\rm SB} \sin(\omega_{\rm m} t - \theta_{\rm m1}) \Big] \\ &\qquad\qquad \times \Big[r_{\rm c2} e^{i\delta\Psi_2} - imr_{\rm c}^{\rm SB} \sin(\omega_{\rm m} t - \theta_{\rm m2}) \Big] \\ &\qquad + \text{c. c.} \Big\}. \end{aligned} \tag{6.18}$$

If the modulation frequency is much larger than the characteristic frequency of the fluctuations, *i.e.*

$$\omega_{\rm m}^2 >> \frac{\langle|\dot{\delta\theta}|^2\rangle}{\langle|\delta\theta|^2\rangle}, \frac{\langle|\dot{\Psi}_1 - \dot{\Psi}_2|^2\rangle}{\langle|\Psi_1 - \Psi_2|^2\rangle}, \tag{6.19}$$

the power spectral density of the intensity has the peaks at $\omega \approx 0$, $\omega_{\rm m}$, and $2\omega_{\rm m}$. In this case, it is possible to extract the terms which have the angular frequency $\omega \approx \omega_{\rm m}$ by using the band pass filter (Fig. 6.3). The terms which is proportional to $\exp(\pm i\omega_{\rm m} t)$ are the cross terms of the carriers and the sidebands, which is represented by

$$\begin{aligned} I_{\pm\omega_{\rm m}} &= mI_0 T_{\rm b} R_{\rm b} r_{\rm c}^{\rm SB} \Big\{ -2r_{\rm c1} \sin\delta\Psi_1 \sin(\omega_{\rm m} t - \theta_{\rm m1}) - 2r_{\rm c2} \sin\delta\Psi_2 \sin(\omega_{\rm m} t - \theta_{\rm m2}) \\ &\quad - e^{-i\delta\theta_-} \Big[i\sin(\omega_{\rm m} t - \theta_{\rm m1}) r_{\rm c2} e^{i\delta\Psi_2} - i\sin(\omega_{\rm m} t - \theta_{\rm m2}) r_{\rm c1} e^{-i\delta\Psi_1} \Big] \\ &\quad - e^{i\delta\theta_-} \Big[-i\sin(\omega_{\rm m} t - \theta_{\rm m1}) r_{\rm c2} e^{-i\delta\Psi_2} + i\sin(\omega_{\rm m} t - \theta_{\rm m2}) r_{\rm c1} e^{i\delta\Psi_1} \Big] \Big\} \\ &\simeq -2mI_0 T_{\rm b} R_{\rm b} r_{\rm c}^{\rm SB} \\ &\quad \times \Big\{ \Big[\delta\Psi_1 r_{\rm c1}(0) - \delta\Psi_2 r_{\rm c2}(0) \Big] \Big[\sin(\omega_{\rm m} t - \theta_{\rm m1}) - \sin(\omega_{\rm m} t - \theta_{\rm m2}) \Big] \end{aligned}$$

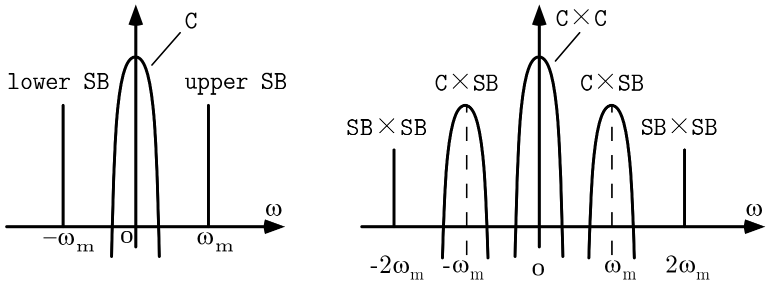

Figure 6.3: *Power spectral density of the amplitude (left) and the intensity (right) of the field in the anti-symmetric port with the modulation. If the modulation frequency is much larger than the characteristic frequency of the fluctuations, the spectrum of the intensity has peaks at $\omega \sim 0, \omega_{\rm m}, 2\omega_{\rm m}$. Only the peak at $\omega \sim \omega_{\rm m}$ is extracted.*

$$
\begin{aligned}
& +\delta\theta_- \Big[\sin(\omega_{\rm m} t - \theta_{\rm m1}) r_{\rm c2}(0) - \sin(\omega_{\rm m} t - \theta_{\rm m2}) r_{\rm c1}(0)\Big]\Big\} \\
\equiv \quad & -2 I_0 T_{\rm b} R_{\rm b} r_{\rm c}^{\rm SB} m_{\rm eff} \times \Big\{ [\delta\Psi_1 r_{\rm c1}(0) - \delta\Psi_2 r_{\rm c2}(0)] \sin(\omega_{\rm m} t + \delta_{\rm m}) \\
& +\delta\theta_- \frac{m}{m_{\rm eff}} \Big[\sin(\omega_{\rm m} t - \theta_{\rm m1}) r_{\rm c2}(0) - \sin(\omega_{\rm m} t - \theta_{\rm m2}) r_{\rm c1}(0)\Big]\Big\},
\end{aligned} \tag{6.20}
$$

where

$$
m_{\rm eff} \equiv m\sqrt{2\,[1 - \cos 2k_{\rm m}(l_1 - l_2)]}\,, \tag{6.21}
$$

$$
\tan\delta_{\rm m} \equiv -\frac{\sin\theta_{\rm m1} - \sin\theta_{\rm m2}}{\cos\theta_{\rm m1} - \cos\theta_{\rm m2}}. \tag{6.22}
$$

These terms are lock-in detected by mixing the intensity signal with the local oscillator. The phase of the local oscillator must be tuned to keep the amplitude of the signal at its maximum, *i.e.*,

$$
v_{\rm LO}(t) \propto \sin(\omega_{\rm m} t + \delta_{\rm m}). \tag{6.23}
$$

The mixed signal is proportional to the fluctuation of the phase-difference of the carriers in two paths;

$$
\begin{aligned}
v_{\rm mix} \quad \simeq \quad & R\frac{e\eta I_0}{\hbar\Omega} T_{\rm b} R_{\rm b} r_{\rm c}^{\rm SB} m_{\rm eff} \left[\delta\Psi_1 r_{\rm c1}(0) - \delta\Psi_2 r_{\rm c2}(0) + \frac{r_{\rm c1}(0) + r_{\rm c2}(0)}{2}\delta\theta_-\right] \\
= \quad & R\frac{e\eta I_0}{\hbar\Omega} T_{\rm b} R_{\rm b} r_{\rm c}^{\rm SB} m_{\rm eff} \overline{r_{\rm c}}(0) \left[\delta\Psi_1 \frac{r_{\rm c1}(0)}{\overline{r_{\rm c}}(0)} - \delta\Psi_2 \frac{r_{\rm c2}(0)}{\overline{r_{\rm c}}(0)} + \delta\theta_-\right]
\end{aligned} \tag{6.24}
$$

where $\overline{r_{\rm c}}(\omega)$ is the mean reflection coefficient of the cavities, R is the constant which have the dimension of the resistance, e is the elementary electric charge, η is the

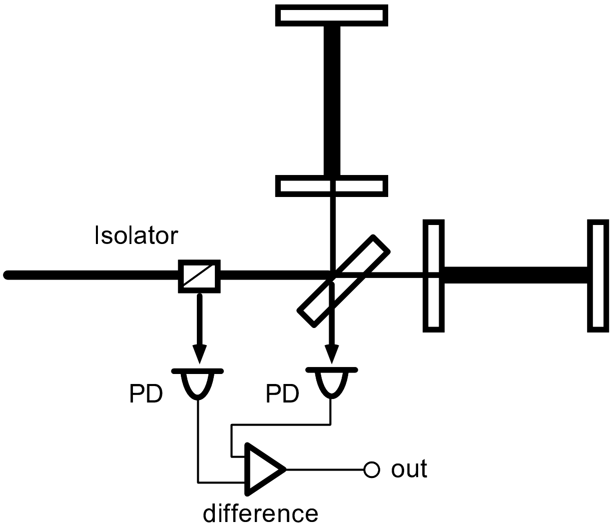

Figure 6.4: *A Fabry-Perot-Michelson interferometer in the homodyne operation. The difference in two optical length is controlled in such a way that the optical power in symmetric and anti-symmetric output is equal to each other. In such a situation, the fluctuation of the difference of the two optical power can be used to sense the fluctuation of the phase-difference.*

quantum efficiency of the photo-detector, and $\hbar$ is the Planck's constant divided by 2π, respectively. If $r_{\mathrm{c}_1}(0) = r_{\mathrm{c}2}(0)$, the above equation is simplified as

$$v_{\mathrm{mix}} \simeq R\frac{e\eta I_0}{\hbar\Omega} T_{\mathrm{b}} R_{\mathrm{b}} r_{\mathrm{c}}^{\mathrm{SB}} \overline{r_{\mathrm{c}}}(0) m_{\mathrm{eff}} (\delta\Psi_1 - \delta\Psi_2 + \delta\theta_-). \tag{6.25}$$

The effective modulation index m_{eff} is proportional to the length-difference between the beamsplitter and the front mirrors (when $k_{\mathrm{m}}(l_1 - l_2) << 1$), therefore the length-difference must be large enough to obtain a considerable amplitude of effective modulation index.

6.2.2 Homodyne Detection of the Signal

In the homodyne detection, each of the carrier field itself is used as the reference to measure the phase of the carrier from another cavity. Figure 6.4 shows the concept of how the homodyne detection is achieved. Compared with the heterodyne detection, there is no modulation sideband in the field. Therefore, by using Eq. 6.9, the field of anti-symmetric and symmetric port are written as

$$\begin{aligned}E_{\rm anti} &= E_0 t_{\rm b} r_{\rm b} e^{i\Omega t}\Big\{e^{-i[\theta_{\rm o1}+\delta\theta_1(t)+\delta\Psi_1(t)]} r_{\rm c1}(0) - e^{-i[\theta_{\rm o2}+\delta\theta_2(t)+\delta\Psi_2(t)]} r_{\rm c2}(0)\Big\} \quad (6.26)\\ E_{\rm sym} &= E_0 e^{i\Omega t}\Big\{T_{\rm b} e^{-i[\theta_{\rm o1}+\delta\theta_1(t)+\delta\Psi_1(t)]} r_{\rm c1}(0) + R_{\rm b} e^{-i[\theta_{\rm o2}+\delta\theta_2(t)+\delta\Psi_2(t)]} r_{\rm c2}(0)\Big\}. \quad (6.27)\end{aligned}$$

Suppose we control the optical length between the beamsplitter and the mirror in such a way that static part of the difference of the phase of the beams is written as

$$\theta_{\rm o1} - \theta_{\rm o2} \equiv \pi\left(n + \frac{1}{2}\right) \quad (6.28)$$

where n is an integer. From Eqs. 6.26, 6.27, and 6.28, the intensity of the antisymmetric and symmetric port are calculated as

$$\begin{aligned}I_{\rm anti} &= I_0 T_{\rm b} R_{\rm b}\left[R_{\rm c1} + R_{\rm c2} + 2 r_{\rm c1} r_{\rm c2}\sin(\delta\Psi_1 - \delta\Psi_2 + \delta\theta_-)\right] \quad (6.29)\\ I_{\rm anti} &= I_0\Big[T_{\rm b}^2 R_{\rm c1} + R_{\rm b}^2 R_{\rm c2} - 2T_{\rm b} R_{\rm b} r_{\rm c1} r_{\rm c2}\sin(\delta\Psi_1 - \delta\Psi_2 + \delta\theta_-)\Big]. \quad (6.30)\end{aligned}$$

We can electronically subtract the constant term in the above expressions in order to obtain a signal which is proportional to the term $\sin\delta\Psi_1 - \delta\Psi_2 + \delta\theta_-$ as

$$\begin{aligned}I_{\rm e} &\equiv I_{\rm anti} - \frac{T_{\rm b} R_{\rm b}(R_{\rm c1} + R_{\rm c2})}{T_{\rm b}^2 R_{\rm c1} + R_{\rm b}^2 R_{\rm c2}} I_{\rm sym}\\ &= 2 I_0 T_{\rm b} R_{\rm b} r_{\rm c1} r_{\rm c2}(1+\alpha)\sin(\delta\Psi_1 - \delta\Psi_2 + \delta\theta_-). \quad (6.31)\end{aligned}$$

In the above equation, $\alpha \equiv T_{\rm b} R_{\rm b}(R_{\rm c1}+R_{\rm c2})/(T_{\rm b}^2 R_{\rm c1}+R_{\rm b}^2 R_{\rm c2})$ is an electronic gain factor which is nearly equal to unity in a well-balanced interferometer (it is equal to unity when the transmittance and the reflectance of the beamsplitter are equal to each other, even if $r_{\rm c1} \neq r_{\rm c2}$). Thus we can use the signal $I_{\rm e}$ to sense any small phase-difference between two paths which is represented as $\delta\Psi_1 - \delta\Psi_2 + \delta\theta_-$ [8] (Fig. 6.4). Note that the optical power in the symmetric and anti-symmetric output is nearly equal to each other in this homodyne operation.

We have directly obtained the product of the carriers from the different paths in the above calculation. Thus it can be said that the DC technique is the technique to measure the difference of the phase from the two cavities directly.

6.3 Frequency Response of the Interferometer

The frequency response of the interferometer to the gravitational radiation, the frequency fluctuation, and the motion of the mirrors will be shown here[2]. Again, we assume that the detector is optimally placed for the propagation direction and the polarization of the incoming gravitational wave. Since all of the equations needed for the derivation of the frequency responses have been presented in the preceding chapters, only the results of the calculations are shown here.

6.3.1 Frequency Response to Gravitational Radiation

When gravitational wave passes the detector, the output of the FPM interferometer is extracted by pre-modulation as

$$\begin{aligned}\Delta\theta(t) &\equiv \delta\theta_{\mathrm{GR1}}(t) - \delta\theta_{\mathrm{GR2}}(t) + \frac{r_{\mathrm{c1}}(0)}{\overline{r_{\mathrm{c}}}(0)}\delta\Psi^{\mathrm{GR}}_{\mathrm{FP1}}(t-l_1/c) - \frac{r_{\mathrm{c2}}(0)}{\overline{r_{\mathrm{c}}}(0)}\delta\Psi^{\mathrm{GR}}_{\mathrm{FP2}}(t-l_2/c)\\ &\equiv +\delta\theta^{\mathrm{GR}}_{\mathrm{MI}}(t) + \delta\Psi^{\mathrm{GR}}_{\mathrm{FPM}}(t)\\ &\equiv \int \tilde{h}(\omega)H^{\mathrm{GR}}_{\mathrm{MI}}(\omega)e^{i\omega t}d\omega + \int \tilde{h}(\omega)H^{\mathrm{GR}}_{\mathrm{FPM}}(\omega)e^{i\omega t}d\omega, \end{aligned} \tag{6.32}$$

where $H^{\mathrm{GR}}_{\mathrm{MI}}(\omega)$ is defined by Eq. 3.35 and $H^{\mathrm{GR}}_{\mathrm{FPM}}(\omega)$ is defined as

$$\begin{aligned}H^{\mathrm{GR}}_{\mathrm{FPM}}(\omega) &\equiv \frac{r_{\mathrm{c1}}(0)}{\overline{r_{\mathrm{c}}}(0)}H_{\mathrm{FP1}}(\omega)\exp(-i\omega l_1/c) + \frac{r_{\mathrm{c2}}(0)}{\overline{r_{\mathrm{c}}}(0)}H_{\mathrm{FP2}}(\omega)\exp(-i\omega l_2/c)\\ &\sim \frac{\Omega}{2\omega_{\mathrm{c1}}}\frac{1}{\overline{r_{\mathrm{c}}}(0)}\frac{\mathcal{F}_1 T_{\mathrm{f1}}}{\pi}\frac{e^{-i\frac{\omega l_1}{c}}}{1+i\frac{\omega}{\omega_{\mathrm{c1}}}} + \frac{\Omega}{2\omega_{\mathrm{c2}}}\frac{1}{\overline{r_{\mathrm{c}}}(0)}\frac{\mathcal{F}_2 T_{\mathrm{f2}}}{\pi}\frac{e^{-i\frac{\omega l_2}{c}}}{1+i\frac{\omega}{\omega_{\mathrm{c2}}}}\end{aligned} \tag{6.33}$$

By using Eqs. 3.35 and 6.33, one can calculate the ratio of $H^{\mathrm{GR}}_{\mathrm{FPM}}$ and $H^{\mathrm{GR}}_{\mathrm{MI}}$ as

$$\left|\frac{H^{\mathrm{GR}}_{\mathrm{MI}}(\omega)}{H^{\mathrm{GR}}_{\mathrm{FPM}}(\omega)}\right| \sim \frac{\bar{l}}{\frac{1}{\overline{r_{\mathrm{c}}}(0)}\frac{\overline{\mathcal{F}}^2\,\overline{T_{\mathrm{f}}}}{\pi^2}\overline{L}}. \tag{6.34}$$

In the most of the interferometric gravitational wave detectors, this ratio is the order of 10^{-5} or less, thus $H^{\mathrm{GR}}_{\mathrm{MI}}$ can be neglected[3].

[2]We will calculate the response of the signal extracted by the pre-modulation technique. However, for the symmetric case, the frequency responses of the two scheme are identical. The difference between these two schemes in asymmetric case will be discussed in Chap. 7

[3]The product of the finesse and the cavity-length is on the order of 10^5m, while the mean distance between the beamsplitter and the near mirrors is on the order of $1 \sim 10$ meters. The product of

Symmetric case

It is important to note the two special cases. If the parameters of the cavities are the same ($\mathcal{F}_1 = \mathcal{F}_2 = \mathcal{F}$, $r_{\mathrm{c1}} = r_{\mathrm{c2}} = r_{\mathrm{c}}$ *etc.*), the frequency response of the FPM interferometer to the gravitational radiation is written as

$$H_{\mathrm{FPM}}^{\mathrm{GR}}(\omega) \sim \frac{\Omega}{\omega_{\mathrm{c}}} \frac{1}{\overline{r_{\mathrm{c}}}(0)} \frac{\mathcal{F} T_{\mathrm{f}}}{\pi} \frac{1}{1 + i\frac{\omega}{\omega_{\mathrm{c}}}} e^{-i\omega \bar{l}/c} \cos(\omega \Delta l/2c) \tag{6.35}$$

where $\bar{l}$ and Δl are the mean and the difference of the distance between the beamsplitter and the front mirrors.

No-loss case

Another important case is when there is no optical loss and the reflectance of the end mirror is equal to unity. In such a situation, the finesse of the cavity is determined by the transmission coefficient of the front mirror as

$$T_{\mathrm{f}i} = (1 - r_{\mathrm{f}i})(1 + r_{\mathrm{f}i}) \simeq \frac{2\pi}{\mathcal{F}_i} \ \ (i = 1, 2). \tag{6.36}$$

Also, the reflection coefficient of the cavity is equal to unity. Equation 6.33 is simplified as

$$H_{\mathrm{FPM}}^{\mathrm{GR}}(\omega) \sim \Omega e^{-i\omega\bar{l}/c} \left(\frac{1}{\omega_{\mathrm{c1}}} \frac{1}{1 + i\frac{\omega}{\omega_{\mathrm{c1}}}} e^{-i\omega\Delta l/2c} + \frac{1}{\omega_{\mathrm{c2}}} \frac{1}{1 + i\frac{\omega}{\omega_{\mathrm{c2}}}} e^{+i\omega\Delta l/2c} \right) \tag{6.37}$$

6.3.2 Frequency Response to Fluctuations of the Light Phase

Suppose that the input field has frequency fluctuations as expressed in Eq. 4.24. The signal which is obtained in pre-modulation technique is calculated as

$$\begin{aligned} \Delta\theta(t) &= -\left[\delta\phi(t - 2l_1/c) - \delta\phi(t - 2l_2/c)\right] \\ &\quad - \left[\frac{r_{\mathrm{c1}}(0)}{\overline{r_{\mathrm{c}}}(0)} \delta\Psi_{\mathrm{FP1}}^{(\mathrm{f})}(t - 2l_1/c) - \frac{r_{\mathrm{c2}}(0)}{\overline{r_{\mathrm{c}}}(0)} \delta\Psi_{\mathrm{FP2}}^{(\mathrm{f})}(t - 2l_2/c) \right] \\ &\equiv -\delta\theta_{\mathrm{MI}}^{\phi}(t) - \delta\Psi_{\mathrm{FPM}}^{\phi}(t). \end{aligned} \tag{6.38}$$

the finesse and the transmission coefficient of the front mirror is about 2π when there are no optical losses in the mirrors and the reflection coefficients of the end mirrors are equal to unity. The reflection coefficient of the cavity is on the order of 1.

We define the frequency response which is represented by H^{ϕ}_{MI} and H^{ϕ}_{FPM} as

$$\begin{aligned} H^{\phi}_{\mathrm{MI}}(\omega) &= \frac{2\pi}{i\omega}\left(e^{-2i\omega l_1/c} - e^{-2i\omega l_2/c}\right) \\ &= \frac{-4\pi}{i\omega} e^{-2i\omega \bar{l}_1/c} \sin\frac{\omega \Delta l}{c} \qquad (6.39) \\ H^{\phi}_{\mathrm{FPM}}(\omega) &= \frac{r_{\mathrm{c1}}(0)}{\overline{r_{\mathrm{c}}}(0)} H^{(\mathrm{f})}_{\mathrm{FP1}}(\omega) e^{-2i\omega l_1/c} - \frac{r_{\mathrm{c2}}(0)}{\overline{r_{\mathrm{c}}}(0)} H^{(\mathrm{f})}_{\mathrm{FP2}}(\omega) e^{-2i\omega l_2/c} \\ &= \frac{2}{\overline{r_{\mathrm{c}}}(0)}\left[\frac{\mathcal{F}_1 T_{\mathrm{f1}}}{\omega_{\mathrm{c1}}} \frac{1}{1+i\frac{\omega}{\omega_{\mathrm{c1}}}} e^{-2i\omega l_1/c} - \frac{\mathcal{F}_2 T_{\mathrm{f2}}}{\omega_{\mathrm{c2}}} \frac{1}{1+i\frac{\omega}{\omega_{\mathrm{c2}}}} e^{-2i\omega l_2/c}\right]. \qquad (6.40) \end{aligned}$$

By using these response function, the terms $\delta\theta^{\phi}_{\mathrm{MI}}$ and $\delta\Psi^{\phi}_{\mathrm{FPM}}$ are written as

$$\delta\theta^{\phi}_{\mathrm{MI}}(t) = \int H^{\phi}_{\mathrm{MI}}(\omega)\delta\tilde{\nu}(\omega)e^{i\omega t}d\omega \qquad (6.41)$$

$$\delta\Psi^{\phi}_{\mathrm{FPM}}(t) = \int H^{\phi}_{\mathrm{FPM}}(\omega)\delta\tilde{\nu}(\omega)e^{i\omega t}. \qquad (6.42)$$

When the parameters of the two cavities are the same, H^{ϕ}_{FPM} is simplified to

$$H^{\phi}_{\mathrm{FPM}}(\omega) = \frac{-4i}{\overline{r_{\mathrm{c}}}(0)} \frac{\mathcal{F} T_{\mathrm{f}}}{\omega_{\mathrm{c}}} \frac{1}{1+i\frac{\omega}{\omega_{\mathrm{c}}}} e^{-2i\omega \bar{l}/c} \sin \omega \Delta l/c. \qquad (6.43)$$

The expression of the function H^{ϕ}_{FPM} is similar to $H^{\mathrm{GR}}_{\mathrm{FPM}}$. However, the phase noise of the laser is a common fluctuation to both of the cavities, while the gravitational radiation is the differential one. Thus, when the parameters of the cavities are the same, H^{f}_{FPM} is proportional to $O(\omega\Delta l/c)$ while $H^{\mathrm{GR}}_{\mathrm{FPM}}$ is proportional to $1 + O(\omega^2\Delta l^2/c^2)$.

6.3.3 Frequency Response to the Motion of the Mirrors

Let us consider the motion of the mirrors. The distance between the beamsplitter and the near mirrors are defined as $l_i + \delta l_i(t)$ $(i = 1, 2)$, where l_i is a static term and δl_i is a fluctuation. In the same way, the lengths of the cavities are defined as $L_i + \delta L_i(t)$ $(i = 1, 2)$.

The signal that is extracted by pre-modulation is written as

$$\begin{aligned} \Delta\theta(t) &= \delta\theta_{l1}(t) - \delta\theta_{l2}(t)\frac{r_{\mathrm{c1}}(0)}{\overline{r_{\mathrm{c}}}(0)}\delta\Psi^{\mathrm{L}}_{\mathrm{FP1}}(t - l_1/c) - \frac{r_{\mathrm{c2}}(0)}{\overline{r_{\mathrm{c}}}(0)}\delta\Psi^{\mathrm{L}}_{\mathrm{FP2}}(t - l_2/c) \\ &= \delta\theta^{l-}_{\mathrm{MI}}(t) + \delta\theta^{l+}_{\mathrm{MI}}(t) + \delta\Psi^{L-}_{\mathrm{FPM}}(t) + \delta\Psi^{L+}_{\mathrm{FPM}}(t), \qquad (6.44) \end{aligned}$$

where the definition of $\delta\theta_{\rm MI}^{l-}$ and $\delta\theta_{\rm MI}^{l+}$ are given by Eqs. 3.47, 3.48, and 3.49. The definition of $\delta\Psi_{\rm FPM}^{L\pm}$ is given by

$$\delta\Psi_{\rm FPM}^{L-}(t) \equiv \int \widetilde{\delta L}_{-}(\omega) H_{\rm FPM}^{L-}(\omega) e^{i\omega t} d\omega \tag{6.45}$$

$$\delta\Psi_{\rm FPM}^{L+}(t) \equiv \int \widetilde{\delta L}_{+}(\omega) H_{\rm FPM}^{L+}(\omega) e^{i\omega t} d\omega, \tag{6.46}$$

where the difference and the sum of the motion $\widetilde{\delta L}_{\pm}$ are defined by

$$\widetilde{\delta L}_{\pm}(\omega) \equiv \widetilde{\delta L}_{1}(\omega) \pm \widetilde{\delta L}_{2}(\omega), \tag{6.47}$$

and the frequency frequency response of a FPM interferometer to the common motion and the differential motion are written as

$$\begin{aligned} H_{\rm FPM}^{L-}(\omega) &\equiv \frac{1}{2}\left[\frac{r_{\rm c1}(0)}{\overline{r_{\rm c}}(0)} H_{\rm FP1}^{L}(\omega)\exp(-i\frac{\omega l_1}{c}) + \frac{r_{\rm c2}(0)}{\overline{r_{\rm c}}(0)} H_{\rm FP2}^{L}(\omega)\exp(-i\frac{\omega l_2}{c})\right] \\ &= \frac{\Omega}{c\overline{r_{\rm c}}(0)}\left[\frac{\mathcal{F}_1^2 T_{\rm f_1}}{\pi^2}\frac{1}{1+i\frac{\omega}{\omega_{\rm c_1}}}e^{-i\omega l_1/c} + \frac{\mathcal{F}_2^2 T_{\rm f_2}}{\pi^2}\frac{1}{1+i\frac{\omega}{\omega_{\rm c_2}}}e^{-i\omega l_2/c}\right] \end{aligned} \tag{6.48}$$

$$\begin{aligned} H_{\rm FPM}^{L+}(\omega) &\equiv \frac{1}{2}\left[\frac{r_{\rm c1}(0)}{\overline{r_{\rm c}}(0)} H_{\rm FP1}^{L}(\omega)\exp(-i\frac{\omega l_1}{c}) - \frac{r_{\rm c2}(0)}{\overline{r_{\rm c}}(0)} H_{\rm FP2}^{L}(\omega)\exp(-i\frac{\omega l_2}{c})\right] \\ &= \frac{\Omega}{c\overline{r_{\rm c}}(0)}\left[\frac{\mathcal{F}_1^2 T_{\rm f_1}}{\pi^2}\frac{1}{1+i\frac{\omega}{\omega_{\rm c_1}}}e^{-i\omega l_1/c} - \frac{\mathcal{F}_2^2 T_{\rm f_2}}{\pi^2}\frac{1}{1+i\frac{\omega}{\omega_{\rm c_2}}}e^{-i\omega l_2/c}\right] \end{aligned} \tag{6.49}$$

6.4 Optical Recombination of the Light Beams

A term "recombination" is used associated with Michelson-type interferometers if the beams divided into two paths are combined again on the beamsplitter. This term is often used in contrast with the "locked FP" type interferometers, in which the beams are independently detected by using optical isolators (Figure 6.5). In locked-FP interferometers, the phase for each of the beams is detected separately. The recombined FPM configuration is indispensable for the interferometric gravitational wave detectors, because of two outstanding advantages. The first is that a power-recycling technique [23] can be applied to the interferometer in order to improve the strain sensitivity limited by the shot noise. The second is that the effect of the common-mode frequency noise of the laser on the strain sensitivity can be reduced in the recombination configuration, which will be described in the next chapter.

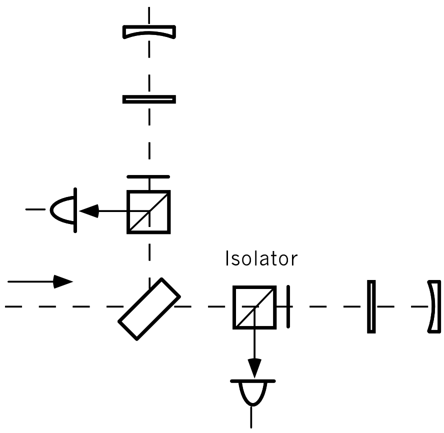

Figure 6.5: *The locked Fabry-Perot interferometer. The beams reflected by the cavities are detected independently by using optical isolators.*

7. Asymmetry of the interferometer

We have seen that the gravitational radiation and the differential motion of the mirrors produce the differential phase shift in the two arms of the FPM interferometer, while the common motion of the mirrors and the frequency fluctuation produce the common phase shift. We will call the frequency noise and the common motion of the mirrors the common-mode noise. From Eqs. 6.33, 6.40, 6.48, and 6.49, it is apparent that the common-mode noise disappears when the interferometer is completely symmetric[1]. However, when there is any asymmetry, a small fraction of the common mode phase shift is detected and distorts the gravitational radiation signal. Therefore it is useful to study the frequency response of the interferometer to the common-mode phase shifts from the point of view of asymmetry.

7.1 Non-Geometrical Asymmetry

7.1.1 Asymmetry of the Optics for the Carrier

We represent the mean value of the constant parameters of the interferometer by the bar-symbol, and the difference by Δ:

$$\bar{l} \equiv \frac{l_1 + l_2}{2} \tag{7.1}$$

$$\Delta l \equiv l_1 - l_2 \tag{7.2}$$

$$\overline{\mathcal{F}} \equiv \frac{\mathcal{F}_1 + \mathcal{F}_2}{2} \tag{7.3}$$

[1]Both the differential- and common-mode terms disappear when the interferometer is symmetric. However, the differential-mode signal is proportional to $m_{\rm eff}$, while the common-mode noise is proportional to $m_{\rm eff} \times O(\omega \Delta l/c)$. Thus the common-mode noise goes to zero faster than the differential-mode signal.

$$\Delta\mathcal{F} \equiv \mathcal{F}_1 - \mathcal{F}_2, \tag{7.4}$$

for example. The Δ-terms are the parameters which characterize the asymmetry of the interferometer. The frequency response of the interferometer in Eqs. 6.33, 6.40, 6.48, and 6.49 are expanded in terms of the asymmetry-parameters as

$$\begin{aligned}
H^{\rm GR}_{\rm FPM}(\omega) &\sim 2\overline{H^{\rm GR}_{\rm FP}}(\omega)e^{-i\omega\bar{l}/c} \\
&= \frac{\Omega}{\overline{\omega}_{\rm c}}\frac{1}{\overline{r_{\rm c}}(0)}\frac{\overline{\mathcal{F}}\overline{T_{\rm f}}}{\pi}\frac{1}{1+i\frac{\omega}{\overline{\omega}_{\rm c}}}e^{-i\omega\bar{l}/c} && (7.5)\\
H^{\phi}_{\rm FPM}(\omega) &= \frac{e^{-2i\omega\bar{l}/c}}{\overline{r_{\rm c}}(0)} \\
&\quad\times\left\{\left[r_{\rm c1}H^{\phi}_{\rm FP1}(\omega) - r_{\rm c2}H^{\phi}_{\rm FP2}(\omega)\right] - \frac{i\omega\Delta l}{c}\left[r_{\rm c1}H^{\phi}_{\rm FP1}(\omega) + r_{\rm c2}H^{\phi}_{\rm FP2}(\omega)\right]\right\} \\
&\sim \frac{2}{\overline{r_{\rm c}}(0)}\frac{\overline{\mathcal{F}}\overline{T_{\rm f}}}{\overline{\omega}_{\rm c}}\frac{e^{-2i\omega\bar{l}/c}}{1+i\frac{\omega}{\overline{\omega}_{\rm c}}}\left(\frac{2\Delta\mathcal{F}}{\overline{\mathcal{F}}}\frac{1+i\frac{\omega}{2\overline{\omega}_{\rm c}}}{1+i\frac{\omega}{\overline{\omega}_{\rm c}}} + \frac{\Delta T_{\rm f}}{\overline{T_{\rm f}}} + \frac{\Delta L}{\overline{L}}\frac{1}{1+i\frac{\omega}{\overline{\omega}_{\rm c}}} - \frac{2i\omega\Delta l}{c}\right) \\
&= \frac{e^{-i\omega\bar{l}/c}}{\nu_{\rm o}}H^{\rm GR}_{\rm FPM}(\omega)\left(\frac{2\Delta\mathcal{F}}{\overline{\mathcal{F}}}\frac{1+i\frac{\omega}{2\overline{\omega}_{\rm c}}}{1+i\frac{\omega}{\overline{\omega}_{\rm c}}} + \frac{\Delta T_{\rm f}}{\overline{T_{\rm f}}} + \frac{\Delta L}{\overline{L}}\frac{1}{1+i\frac{\omega}{\overline{\omega}_{\rm c}}} - \frac{2i\omega\Delta l}{c}\right) && (7.6)\\
H^{L-}_{\rm FPM}(\omega) &\sim \frac{2\Omega}{c\overline{r_{\rm c}}(0)}\frac{\overline{\mathcal{F}}^2\overline{T_{\rm f}}}{\pi^2}\frac{1}{1+i\frac{\omega}{\overline{\omega}_{\rm c}}}e^{-i\omega\bar{l}/c} \\
&= \frac{1}{\overline{L}}H^{\rm GR}_{\rm FPM}(\omega) && (7.7)\\
H^{L+}_{\rm FPM}(\omega) &= \frac{e^{-i\omega\bar{l}/c}}{\overline{r_{\rm c}}(0)} \\
&\quad\times\left\{\left[r_{\rm c1}H^{\rm L}_{\rm FP1}(\omega) - r_{\rm c2}H^{\rm L}_{\rm FP2}(\omega)\right] - \frac{i\omega\Delta l}{2c}\left[r_{\rm c1}H^{\rm L}_{\rm FP1}(\omega) + r_{\rm c2}H^{\rm L}_{\rm FP2}(\omega)\right]\right\} \\
&\sim \frac{\Omega}{c\overline{r_{\rm c}}(0)}\frac{\overline{\mathcal{F}}^2\overline{T_{\rm f}}}{\pi^2}\frac{e^{-i\omega\bar{l}/c}}{1+i\frac{\omega}{\overline{\omega}_{\rm c}}}\left(\frac{2\Delta\mathcal{F}}{\overline{\mathcal{F}}}\frac{1+i\frac{\omega}{2\overline{\omega}_{\rm c}}}{1+i\frac{\omega}{\overline{\omega}_{\rm c}}} + \frac{\Delta T_{\rm f}}{\overline{T_{\rm f}}} - \frac{\Delta L}{\overline{L}}\frac{i\frac{\omega}{\overline{\omega}_{\rm c}}}{1+i\frac{\omega}{\overline{\omega}_{\rm c}}} - \frac{i\omega\Delta l}{c}\right) \\
&= \frac{1}{2\overline{L}}H^{\rm GR}_{\rm FPM}(\omega)\left(\frac{2\Delta\mathcal{F}}{\overline{\mathcal{F}}}\frac{1+i\frac{\omega}{2\overline{\omega}_{\rm c}}}{1+i\frac{\omega}{\overline{\omega}_{\rm c}}} + \frac{\Delta T_{\rm f}}{\overline{T_{\rm f}}} - \frac{\Delta L}{\overline{L}}\frac{i\frac{\omega}{\overline{\omega}_{\rm c}}}{1+i\frac{\omega}{\overline{\omega}_{\rm c}}} - \frac{i\omega\Delta l}{c}\right) && (7.8)
\end{aligned}$$

to the first order of the asymmetry parameters, where $\overline{H^{\rm GR}_{\rm FP}}(\omega)$ is the mean response function of the cavities. In the above expression, the parameters $\Delta\mathcal{F}$, $\Delta T_{\rm f}$, and ΔL are the parameters which describe the asymmetry of the cavities, while Δl describes the asymmetry of the length between the beam splitter and the front mirrors.

Correction for Homodyne Scheme

All of the above presented calculations are for the P-D-H detection scheme. In the homodyne scheme, since only the difference of the phase between the carriers rather than the amplitude is detected, correction terms are needed for the asymmetry analysis:

$$-\frac{e^{-i\omega\bar{l}/c}}{\nu_\mathrm{o}} H^{\mathrm{GR}}_{\mathrm{FPM}}(\omega) \times \frac{\Delta r_\mathrm{c}}{\overline{r_\mathrm{c}}(0)} \tag{7.9}$$

has to be added to Eq. 7.6, and

$$-\frac{1}{2\overline{L}} H^{\mathrm{GR}}_{\mathrm{FPM}}(\omega) \times \frac{\Delta r_\mathrm{c}}{\overline{r_\mathrm{c}}(0)} \tag{7.10}$$

to Eq. 7.8, where Δr_c is the difference between the DC reflection coefficients of the cavities for the carrier.

7.1.2 Asymmetry of the Optics for the Sidebands

So far we have ignored the asymmetry of the sidebands because the reflectance of FP for the sidebands is considered to be almost equal to unity. However, there may be some asymmetry if there are apparent loss factors in the interferometer[2]. It is easily shown that the asymmetry for the sidebands is interpreted as a shift of the optimal demodulation phase and a change in the effective modulation index. If we introduce the reflection coefficients for the sidebands for each of the cavities represented by $r^{\mathrm{SB}}_{\mathrm{c}n}$ ($n = 1, 2$), the reflectance for the sidebands in Eq. 6.24 has to be replaced by the mean reflectance,

$$\overline{r^{\mathrm{SB}}_\mathrm{c}} = \frac{r^{\mathrm{SB}}_{\mathrm{c1}} + r^{\mathrm{SB}}_{\mathrm{c2}}}{2}. \tag{7.11}$$

The new definition of the effective modulation index and the optimal demodulation phase are:

$$m_{\mathrm{eff}} \equiv m \left(\overline{r^{\mathrm{SB}}_\mathrm{c}}\right)^{-1} \sqrt{(r^{\mathrm{SB}}_{\mathrm{c1}})^2 + (r^{\mathrm{SB}}_{\mathrm{c2}})^2 - 2r^{\mathrm{SB}}_{\mathrm{c1}} r^{\mathrm{SB}}_{\mathrm{c2}} \left[1 - \cos 2k_\mathrm{m}(l_1 - l_2)\right]} \tag{7.12}$$

$$\tan\delta_\mathrm{m} \equiv -\frac{r^{\mathrm{SB}}_{\mathrm{c1}} \sin\theta_{\mathrm{m1}} - r^{\mathrm{SB}}_{\mathrm{c2}} \sin\theta_{\mathrm{m2}}}{r^{\mathrm{SB}}_{\mathrm{c1}} \cos\theta_{\mathrm{m1}} - r^{\mathrm{SB}}_{\mathrm{c2}} \cos\theta_{\mathrm{m2}}}. \tag{7.13}$$

These have to be taken into account for the sideband-asymmetry.

[2]For example, the anti-reflection (AR) coating of the back side of the mirror has finite reflectance which produce an apparent loss in the interferometer. Any asymmetry in such AR coatings will lead to an asymmetry not only for the carrier but also for the sidebands.

7.2 Geometrical Asymmetry

Even if the optics have ideal quality, any misalignment produce an asymmetry in the interferometer. This is because the phase of the reflected light is shifted by the misalignment according to Eqs. 5.66 – 5.68. For convenience, let us assume that the optics are completely symmetric except for the alignment. Also, let us consider only the frequency noise for simplicity. Suppose that the input beam is matched to the cavities of the interferometer, but there are small misalignments in the orientation of the mirrors. Again for simplicity, only the misalignments in one dimension are discussed. After some calculations using Eqs. 5.66 – 5.68 and 5.70, the amplitude of the common mode noise in the differential phase measurement which is represented by $\Psi^{\phi}_{\mathrm{comm}}(t)$ is obtained[3]:

$$\Psi^{\phi}_{\mathrm{comm}}(t) \sim -\Psi^{\phi}_{\mathrm{FP}}(t) \frac{1}{r_{\mathrm{c}0}(0)} \left(\frac{a_{x1}^2 - a_{x2}^2}{w_0^2} - \frac{\alpha_{x1}^2 - \alpha_{x2}^2}{\alpha_0^2} \right) \tag{7.14}$$

where a_{xn} and α_{xn} $(n = 1, 2)$ are the misalignment parameters of the cavities. Therefore, in this case, the frequency response of the interferometer is written as

$$H^{\phi}_{\mathrm{FPM}}(\omega) \sim -\frac{e^{-i\omega\bar{l}/c}}{\nu_{\mathrm{o}}} H^{\mathrm{GR}}_{\mathrm{FPM}}(\omega) \times \frac{1}{r_{\mathrm{c}0}(0)} \left(\frac{a_{x1}^2 - a_{x2}^2}{w_0^2} - \frac{\alpha_{x1}^2 - \alpha_{x2}^2}{\alpha_0^2} \right). \tag{7.15}$$

7.3 Rejection of the Common-Mode Noise

From Eqs. 7.5 –7.8, we can see that the disturbance that acts in-phase on the two cavities "leaks" to the anti-symmetric port if there is any asymmetry, and distorts the gravitational wave signal. The common-mode-noise-rejection-ratio (CMRR) of the interferometer is defined as the ratio of the difference of the phase delays of the field from the perpendicular cavity and the parallel cavity to the mean phase delay of the cavities. For the frequency fluctuation, CMRR is defined to

$$\begin{aligned} \gamma^{\phi}(\omega) &\equiv \frac{H^{\phi}_{\mathrm{MI}}(\omega) + H^{\phi}_{\mathrm{FPM}}(\omega)}{\overline{H^{\phi}_{\mathrm{FP}}}(\omega)} \\ &\sim \frac{H^{\phi}_{\mathrm{FPM}}(\omega)}{\overline{H^{\phi}_{\mathrm{FP}}}(\omega)} \end{aligned} \tag{7.16}$$

[3]This expression can be used both for P-D-H scheme and homodyne scheme, except for some factor which is close to unity.

where $\overline{H^{\phi}_{\rm FP}}(\omega)$ is the mean response function of the cavities to the frequency fluctuation. Using Eqs. 7.6 and 7.16, the expression of CMR to the phase noise is obtained as

$$\gamma^{\phi}(\omega) \simeq \left(\frac{2\Delta\mathcal{F}}{\overline{\mathcal{F}}} \frac{1+i\frac{\omega}{2\overline{\omega}_{\rm c}}}{1+i\frac{\omega}{\overline{\omega}_{\rm c}}} + \frac{\Delta T_{\rm f}}{\overline{T_{\rm f}}} + \frac{\Delta L}{\overline{L}} \frac{1}{1+i\frac{\omega}{\overline{\omega}_{\rm c}}} - \frac{2i\omega\Delta l}{c} \right) e^{-2i\omega\bar{l}/c} \tag{7.17}$$

for the asymmetry of the optics, and

$$\gamma^{\phi}(\omega) \simeq \frac{1}{r_{\rm c0}(0)} \left(\frac{a_{x1}^2 - a_{x2}^2}{w_0^2} - \frac{\alpha_{x1}^2 - \alpha_{x2}^2}{\alpha_0^2} \right) e^{-2i\omega\bar{l}/c} \tag{7.18}$$

for the asymmetry of the alignment. The amplitude of the equivalent noise which is caused by the phase noise is written as

$$h^{\phi}_{\rm n}(\omega) = \gamma^{\phi}(\omega) \times \frac{\delta\nu(\omega)}{\nu_{\rm o}} e^{i\omega\bar{l}/c} \tag{7.19}$$

in the unit of the dimension-less strain h, and

$$\delta L^{\phi}_{\rm n-}(\omega) = \gamma^{\phi}(\omega) \times \overline{L} \frac{\delta\nu(\omega)}{\nu_{\rm o}} e^{i\omega\bar{l}/c} \tag{7.20}$$

in the unit of the differential motion δL_-.

No-Loss case

When there is no optical loss in the mirrors and the reflectances of the end mirrors are equal to unity, $\Delta\mathcal{F}$ and $\Delta T_{\rm f}$ are not independent. From Eq. 6.36, we obtain the following equation:

$$\frac{\Delta T_{\rm f}}{\overline{T_{\rm f}}} = -\frac{\Delta\mathcal{F}}{\overline{\mathcal{F}}}. \tag{7.21}$$

In this case, the expression for CMRR is simplified as

$$\gamma^{\phi}(\omega) \simeq \left[\left(\frac{\Delta\mathcal{F}}{\overline{\mathcal{F}}} + \frac{\Delta L}{\overline{L}} \right) \frac{1}{1+i\frac{\omega}{\overline{\omega}_{\rm c}}} - \frac{2i\omega\Delta l}{c} \right] e^{-2i\omega\bar{l}/c}. \tag{7.22}$$

When $L_1\mathcal{F}_1 = L_2\mathcal{F}_2$ (or, in other words $\omega_{\rm c1} = \omega_{\rm c2}$), the asymmetry term of the cavity disappears.

8. 3-meter Fabry-Perot-Michelson Interferometer

The recombined Fabry-Perot-Michelson (FPM) configuration is indispensable for the interferometric gravitational wave detectors, because of two outstanding advantages. The first is that a power-recycling technique [23] can be applied to the interferometer in order to improve the sensitivity, which is limited by the shot noise. The second is that the common-mode noise due to frequency fluctuation of the laser can be reduced in the recombination configuration. The common-mode-noise-rejection ratio of the interferometer is quite important, because the requirement on the frequency stability of the laser can be considerably relaxed if the interferometer has a good CMRR.

Since all of the optical components must be suspended independently as pendulums for GW detection, it is quite significant to test the properties of the optical system and to develop a technique to control the interferometer in a more realistic situation. Therefore an optically recombined FPM interferometer with the 3 m baseline has been built in the campus of the University of Tokyo. The mirrors and the beamsplitter of the interferometer are suspended independently by wires. The aim of the construction of this interferometer was to experimentally investigate the optical recombination, especially the common-mode noise rejection under the all-suspended configuration. This was the first example of the optically recombined, all-suspended interferometer with the Fabry-Perot cavities in the arms[16][1]. The experimental setup of the 3m-FPM interferometer is shown in Fig. 8.1. There are three important points about this setup.

[1]Before the 3m-FPM experiment, the recombined FPM configuration was experimentally investigated with only table-top interferometers having rigidly mounted mirrors and beamsplitter [24, 25], while the all-suspended configuration of the FPM was studied with the locked-Fabry-Perot configuration [26].

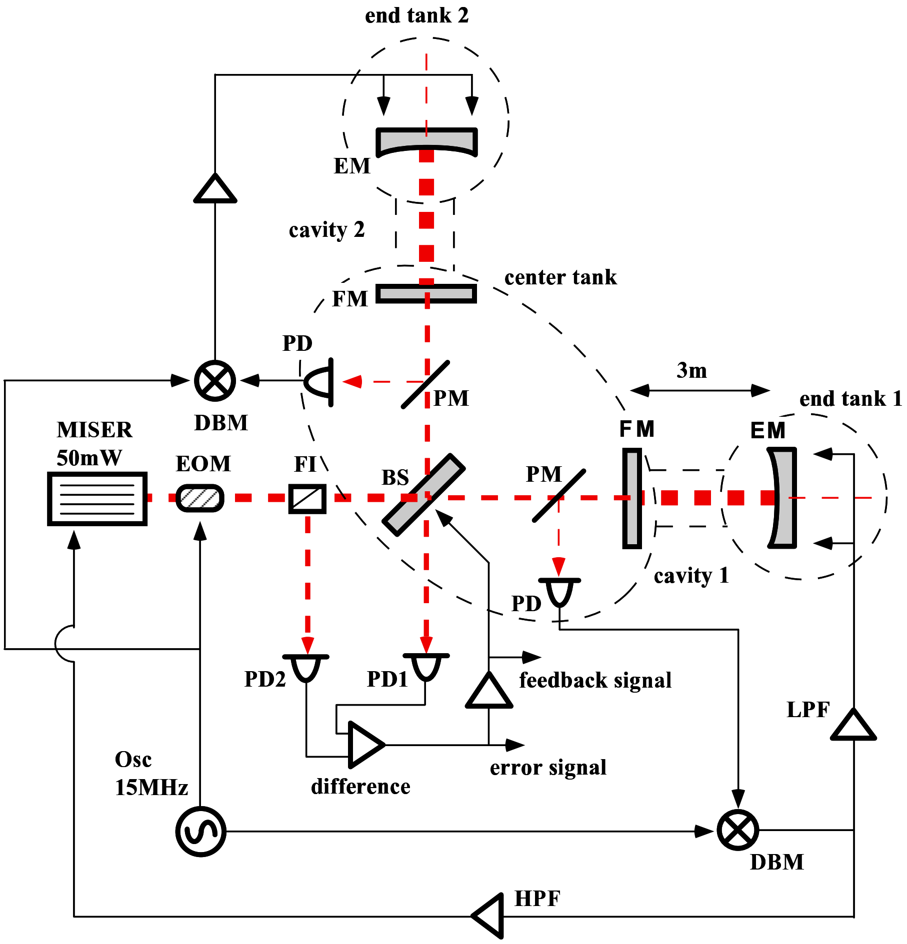

Figure 8.1: *The schematic diagram of the 3m FPM interferometer which was built in the campus of the University of Tokyo. As a light source, a laser-diode-pumped Nd:YAG laser (*Lightwave*, MISER model 124) was used. FM, front mirror; EM, end mirror; BS, beamsplitter; FI, Faraday isolator; PM, partial mirror for pick-off purpose; PD, photo-detector; EOM, electro-optical modulator; Osc, local oscillator; DBM, double-balanced modulator. L, spherical lens; CL, cylindrical lens.*

- The laser beams reflected by the two FP cavities were recombined again on the beamsplitter. The relative phase difference between the two beams was detected by using the recombined beam.

- For convenience, the operation point of the interferometer was chosen at the steepest slope of the fringe. In other words, the signal was extracted by using homodyne detection[2].

- All of the optical components were suspended independently by wires.

In this chapter, the experimental apparatus of the 3-meter interferometer is described. Calibration procedures that were the basis of the displacement sensitivity analysis are also be shown.

8.1 Layout of the Optics

Figure 8.2 shows the optical layout of the interferometer. The input optics were set on a small optical bench. As a light source we used a laser-diode-pumped Nd:YAG laser (Lightwave, MISER model 124). It has a linearly polarized, single mode beam with a power of 54 mW. Also it has an elliptical beam profile, because the laser resonator of MISER is a non-planar ring cavity. Two cylindrical lenses were used to transform the beam to the axisymmetric one. A lens was used to match the beam to the fundamental mode of the 3-m cavity. An electro-optical modulator (EOM, Newfocus model 4003) was used to apply a phase modulation at 15 MHz. The modulation index of the EOM was measured to be $m \approx 0.67$. After EOM, two Faraday isolators (FI) were used to prevent optical feedback to the laser. The beam was introduced into the vacuum

[2]Because of this feature, *i.e.* the homodyne scheme, the interferometer was not directly compatible with power-recycling. However, the demonstration of the recombination technique in this experiment led to the power-recycling demonstration. As soon as this experiment had been finished, the optical configuration of the interferometer has been changed to the pre-modulation topology to lock the operation point to the dark-fringe [43]. After the reconfiguration of the optical and servo topology to pre-modulation scheme [44], the power-recycling has been demonstrated successfully with the all-suspended FPM interferometer [45, 46].

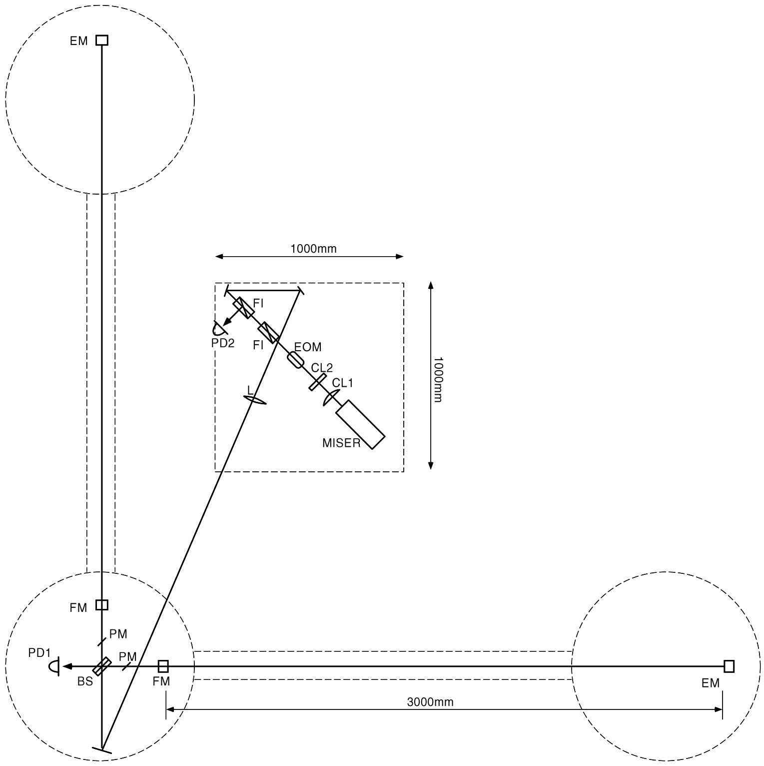

Figure 8.2: *Layout of the optics. The laser and the input optics were set on a 1 m by 1 m optical bench. The mirrors and the beamsplitter of the interferometer were housed in a vacuum enclosure. FM, front mirror; EM, end mirror; BS, beamsplitter; FI, Faraday isolator; PM, partial mirror for pick-off purpose; PD, photo-detector; EOM, electro-optical modulator; L, spherical lens; CL, cylindrical lens.*

chamber through an anti-reflecting coated glass window. Several mirrors were used for the coarse alignment of the beam. Though the output power of the laser was about 54 mW, the optical power which was led into the interferometer was about 29 mW, due to the optical loss of the optics placed between the laser and the interferometer.

In the vacuum chamber, a beamsplitter and two Fabry-Perot cavities formed a Fabry-Perot-Michelson type interferometer. The beam was led to the beamsplitter and was injected to the arm Fabry-Perot cavities. The reflected beams from the cavities were optically recombined on the beamsplitter. A part of the optical power of the recombined beam was led to the photo detector in the center chamber (PD1 in Fig. 8.2), while the rest of the power was reflected back to the optical bench, reflected by the Faraday isolator and detected by another photo-detector (PD2 in Fig. 8.2). The outputs of the photo-detectors were used for the signal extraction of the interferometer (see also 8.4.3). A small part of the optical power reflected from the arm cavities was picked off by two partially reflecting mirrors (PO in Fig. 8.2). The picked-off beams were also used for the signal extraction of the arm cavities (see 8.4.2).

8.2 Vacuum

The main part of the interferometer is housed in a vacuum system (Fig 8.3) to protect the interferometer against any acoustic noise. The whole system comprises three identical chambers with an inner diameter of one meter. The center chamber and the end chambers are connected by 15-cm-diameter vacuum tubes. The distance between the center and the end chamber is 3 m, from center to center. The whole system is evacuated by using a scroll pump connected to the center chamber. All of the measurements were made under a pressure of less than 10 Pa.

8.3 Mirror Suspension

The beamsplitter and the mirrors of the Fabry-Perot cavities were suspended by the suspension system shown in Fig.8.4. Seismic vibration was isolated horizontally by a double pendulum [27] and vertically by the coil springs. The intermediate mass of the

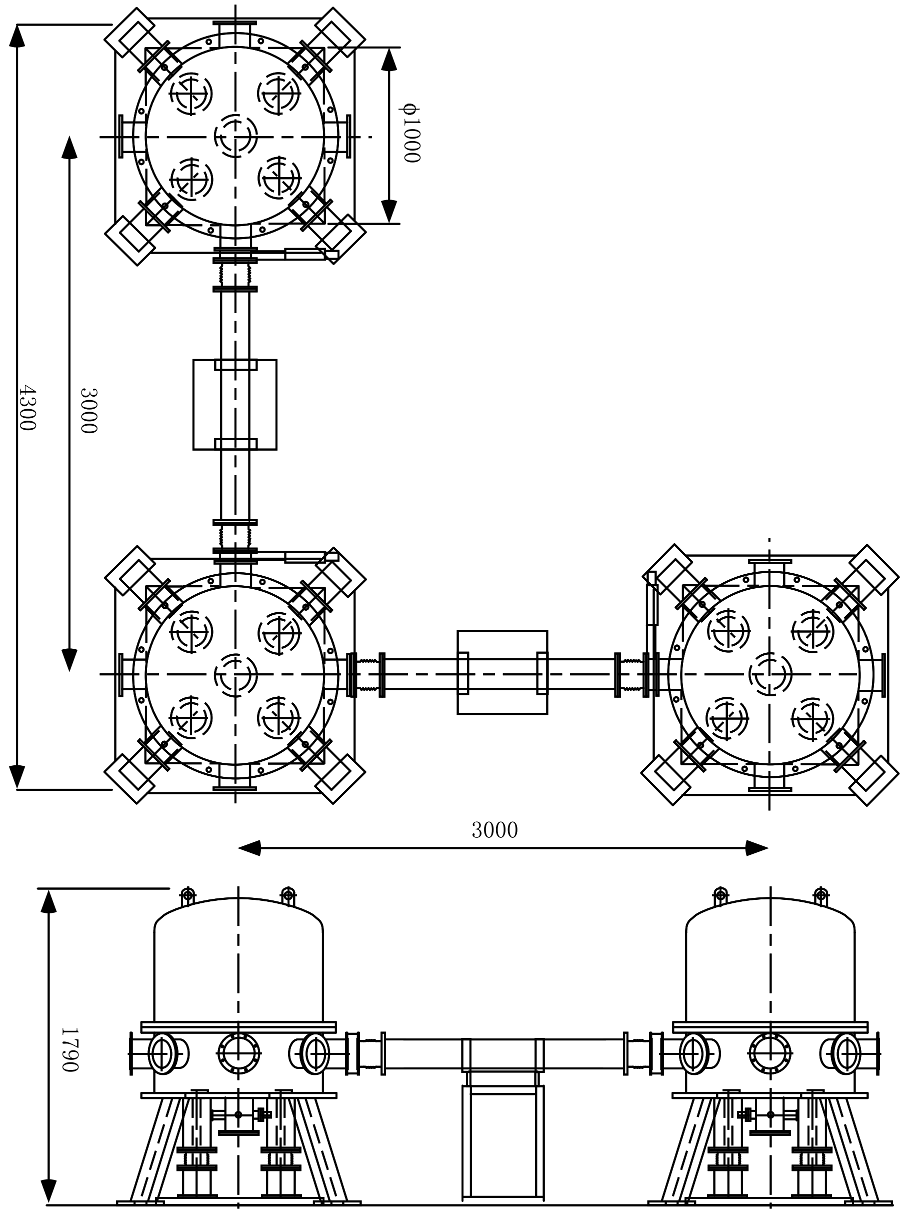

Figure 8.3: *The vacuum system of the interferometer comprises three identical chambers. The inner diameter of each chamber is one meter. The distance between the center and the end chamber is three meters, from center to center.*

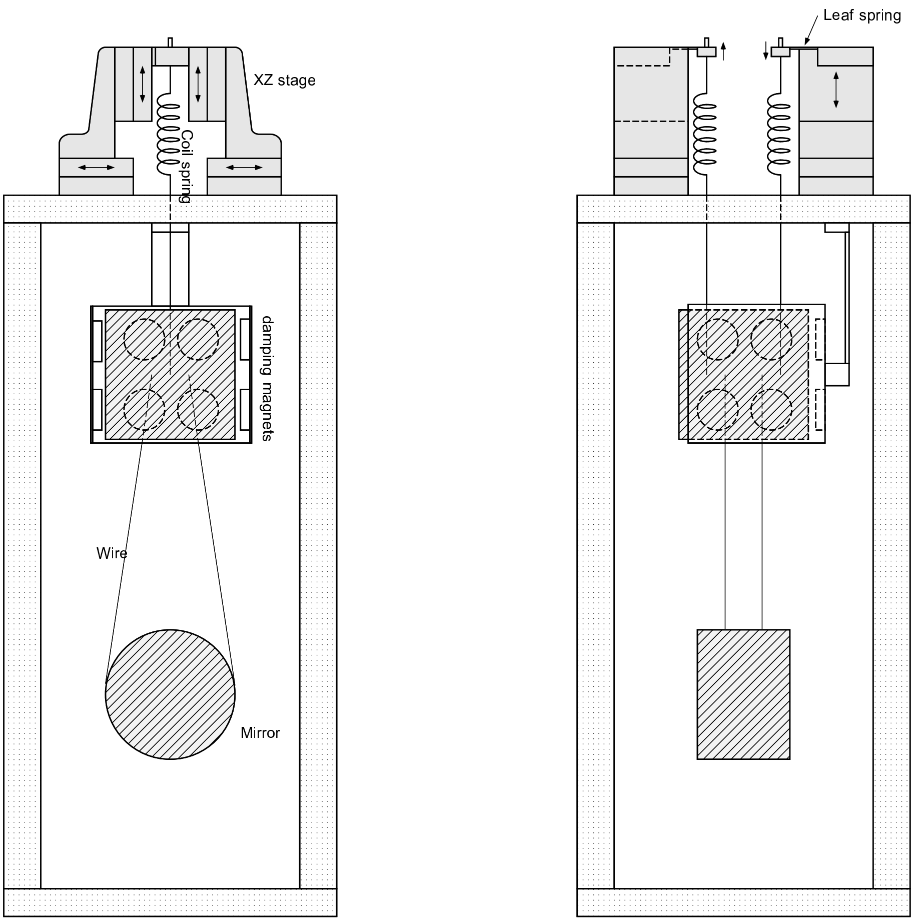

Figure 8.4: *The suspension system of the mirrors. Horizontal vibration was isolated by a double pendulum. The vertical isolation was mainly provided by the coil-springs. The leaf springs were used for the fine adjustment of the alignment by using the actuators.*

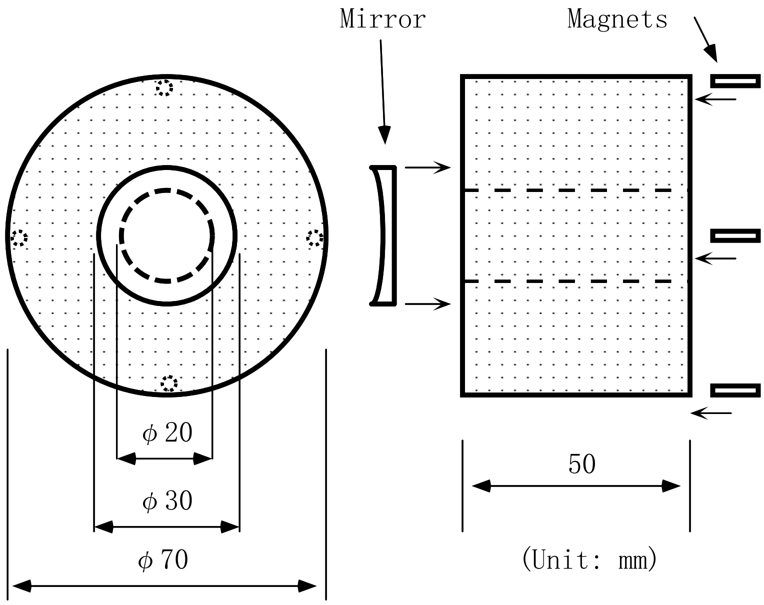

Figure 8.5: *A mirror and four magnets were glued to each of the test masses which are made of aluminum. The diameter and the thickness of the mirror is 3 cm and 5 mm. The diameter and the thickness of the test mass are 7 cm and 5 cm. The diameter of the hole drilled at the center of the cylinder is 2cm.*

pendulum was made of copper and was suspended by two coil springs. The bottom mass (the test mass) was a cylinder made of aluminum and was suspended by two loops of wire from the intermediate mass. Each mirror with the diameter of 3 cm and the thickness of 5 mm was glued to the test mass (Fig. 8.5). The diameter and the thickness of the test mass was 7 cm and 5 cm, respectively. Four small permanent magnets for the control purpose were glued on the opposite side of the test mass to the mirror.

The beamsplitter was also suspended by the same suspension mechanism as the mirrors. The diameter and the thickness of the beamsplitter [3] was 10 cm and 3 cm. Figure 8.6 shows the physical dimensions of the beamsplitter. Both sides of the half-mirror coating are covered with anti-reflection coated glass. Four magnets were glued directly on one side of the beamsplitter. The translation of the mirrors and the beam-splitter was controlled by using two coil-and-magnet-type actuators which were verti-

[3] This beamsplitter is identical to the one used in the 20-m FPM interferometer built in the campus of National Astronomical Observatory, Japan.

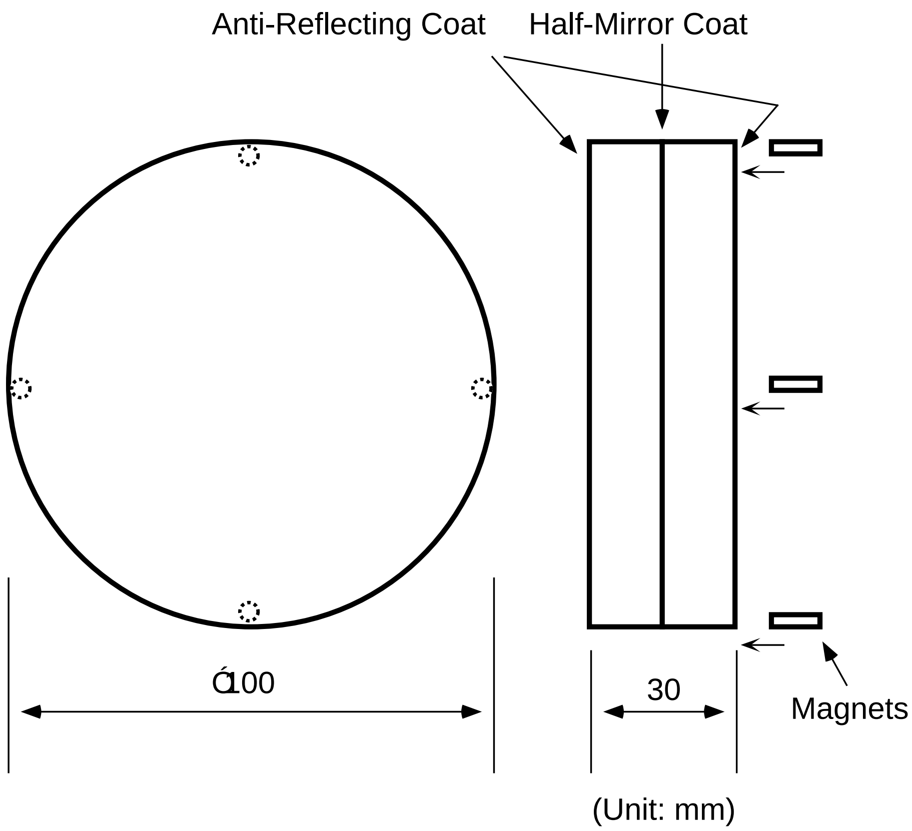

Figure 8.6: *Physical dimensions of the beamsplitter. The diameter is 10 cm and the thickness is 3cm. Four magnets were glued to the beamsplitter.*

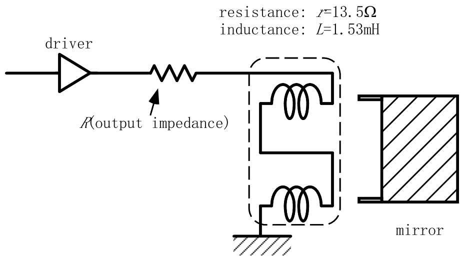

Figure 8.7: *A force, proportional to the current in the coil, was applied to the test mass.*

cally aligned on the test mass. The other two horizontally-aligned actuators on the test mass were used for the fine adjustment of the yaw-alignment. The suspension point of the coil springs were supported by the leaf springs. The two actuators set on the leaf springs were used for the fine pitch-alignment. No active feedback servo was used for the alignment.

Strong permanent magnets were used to damp by eddy currents the large motion of the intermediate mass due to the resonance of the pendulum [27]. The permanent magnets were also isolated from external vibrations by a leaf spring.

8.3.1 Actuator

The actuators used for the translational and rotational control of the test masses were of the coil-and-magnet type (Fig.8.7). Magnets were glued to the masses and the coils were fixed to the optical table in the vacuum chamber. The coils were driven by a simple buffer amplifier which had the finite output impedance R. The force applied on the test masses were proportional to the current in the coil. The internal resistance and the inductance of the coils of the actuators were measured as being 13.4Ω and 1.53mH for the mirror control, and 7.35Ω and 0.793mH for the beamsplitter control.

In a voltage-driven coil circuit, a pole is generated by the output impedance and the inductance as

$$\frac{1}{1 + i\omega\frac{L}{R+r}}, \tag{8.1}$$

where r and L are the internal resistance and the inductance of the coil. However, the measured frequency of the pole was 50.3kHz for the mirror and 39.2kHz for the

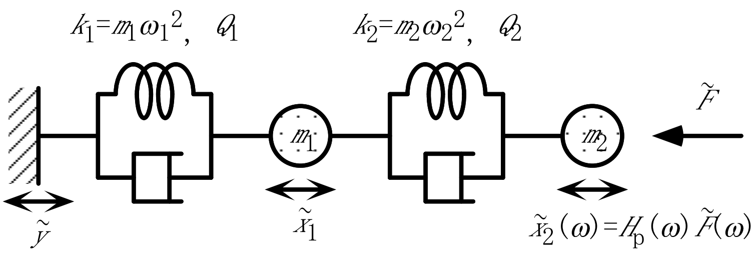

Figure 8.8: *The suspension is well approximated by a two-mode oscillator.*

beamsplitter (see AppendixB for the circuits of the drivers), therefore the poles can be ignored.

8.3.2 Model of the Suspension

The suspension is well approximated by a two-mode oscillator illustrated in Fig. 8.8. In the figure, y, m_i, x_i, and k_i $(i = 1, 2)$ are the displacement of the suspension point, the masses, the displacements, and the spring constants. Also, ω_1 and Q_1 are the resonant angular frequency and the Q-factor of the first stage pendulum without the second stage $(k_2 = 0)$, and ω_2 and Q_2 are those of the second stage pendulum with the intermediate mass fixed $(x_1 = 0)$. The equations of motions for the masses are written as

$$-\omega^2\tilde{x}_1 = \left[-\frac{m_2}{m_1}\left(\omega_2^2 + i\frac{\omega\omega_2}{Q_2}\right)(\tilde{x}_1 - \tilde{x}_2) - \left(\omega_1^2 + i\frac{\omega\omega_1}{Q_1}\right)(\tilde{x}_1 - \tilde{y})\right] \tag{8.2}$$

$$-\omega^2\tilde{x}_2 = -\left(\omega_2^2 + i\frac{\omega\omega_2}{Q_2}\right)(\tilde{x}_2 - \tilde{x}_1) + \frac{1}{m_2}\tilde{F} \tag{8.3}$$

where F is the force applied on the test mass. Solving theses equations, the transfer function of the actuator system defined as the transfer function from the force of the actuator to the position of the test mass is written as follows;

$$H_{\mathrm{p}}(\omega) = \frac{1}{m_2}\frac{\omega_1^2 + \alpha\omega_2^2 - \omega^2 + i\omega\left(\omega_1/Q_1 + \alpha\omega_2/Q_2\right)}{\left(\omega_2^2 - \omega^2 + i\omega\omega_2/Q_2\right)\left(\omega_1^2 - \omega^2 + i\omega\omega_1/Q_1\right) - \alpha\omega^2\left(\omega_2^2 + i\omega\omega_2/Q_2\right)} \tag{8.4}$$

where $\alpha \equiv m_2/m_1$ is the ratio of the masses. In a similar way, the isolation ratio defined as the transfer function from the vibration of the suspension point to the

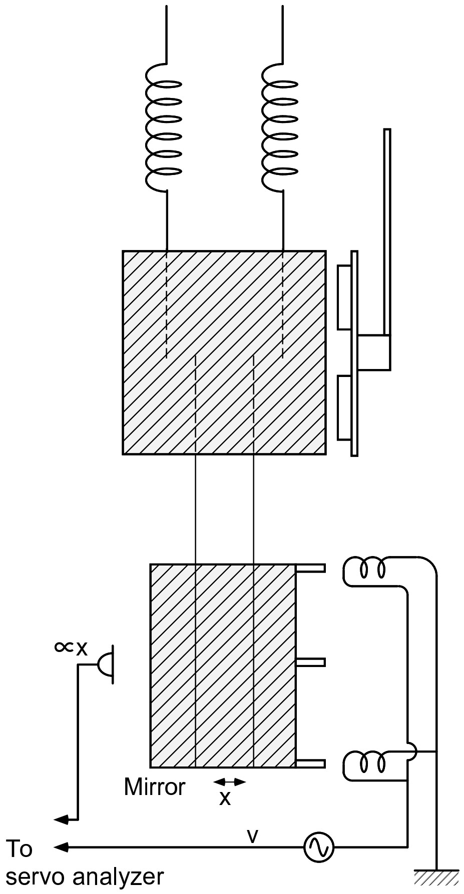

Figure 8.9: *Measurement of the transfer function from the voltage applied to the actuator to the displacement of the mirror. The motion of the mirror is measured by using reflection type photo sensor(see Appendix B).*

mirror-displacement is calculated as

$$H_{\mathrm{isol}}(\omega) = \frac{(\omega_1^2 + i\omega\omega_1/Q_1)\,(\omega_2^2 + i\omega\omega_2/Q_2)}{(\omega_2^2 - \omega^2 + i\omega\omega_2/Q_2)\,(\omega_1^2 - \omega^2 + i\omega\omega_1/Q_1) - \alpha\omega^2\,(\omega_2^2 + i\omega\omega_2/Q_2)}. \quad (8.5)$$

To identify the parameters of the suspension system, the transfer function of the actuator system was measured (Fig. 8.9) by using a reflection type photo-sensor[4]. Figure 8.10 shows the measured and fitted transfer function from the input voltage of the coil driver to the motion of the test mass. In the calculation of the transfer function, it is a good approximation that the loss in the wire of the last stage was negligible in the measurement frequency band. Therefore, in the least-squares fit, the

[4]see Appendix B for the detail of the reflection type photo sensor)

fitting parameters were the frequencies (ω_1 and ω_2), the quality factor of the first stage (Q_1), and the ratio of the masses (m_2/m_1). The least-squares fit resulted in $f_1 = \omega_1/2\pi = 1.53$Hz, $Q_1 = 0.59$, $f_2 = \omega_2/2\pi = 1.23$Hz, and $m_2/m_1 = 0.58$. From these parameters, the isolation ratio of the suspension system was calculated. Figure 8.11 shows the calculated plot of the isolation ratio. The Q-value of the final pendulum (Q_2) was not measured, but it is quite reasonable to assume that the Q-value was more than 1000. There are two curves plotted in the figure, one with $Q_2 = \infty$ and the other with $Q_2 = 1000$. As the plot shows, there is almost no difference between the two curves in the frequency range lower than 1kHz, therefore the model with $Q_2 =!\infty$ will be adopted as the isolation ratio model in the low-frequency range. Note that all of the mechanical resonances except the pendulum peak are ignored in this model, therefore the real isolation ratio is believed to have been much poorer than this, especially in the frequency range higher than 100Hz.

8.3.3 Beamsplitter

The beamsplitter has a polarizing property. Its transmittance and reflectance were measured with various polarizations of the input beam by using a half-wave plate that is mounted on a rotating holder (Fig. 8.12). Figure 8.13 shows the measured dependence of the beamsplitter to the polarization. When the input beam has the S-polarization, the reflectance is about 51 % and the transmittance about 49 %.

As shown in Fig. 8.6, each side of the beamsplitter coating is covered with the anti-reflection (AR) coated glass with a thickness of 15 mm. The reflectance of the AR coat was measured to be 0.5±0.1%. Though the reflectance of the AR was small, the beams generated by the reflection at the AR coats interfered with the main beams. Therefore baffles having small apertures were inserted to shut out the spurious paths (Fig. 8.14).

8.3.4 Mirrors

The optical paths of the arms of the interferometer are folded by using FP cavities. Each FP cavity comprises a flat front mirror (reflectance 97.5 %) and a concave end

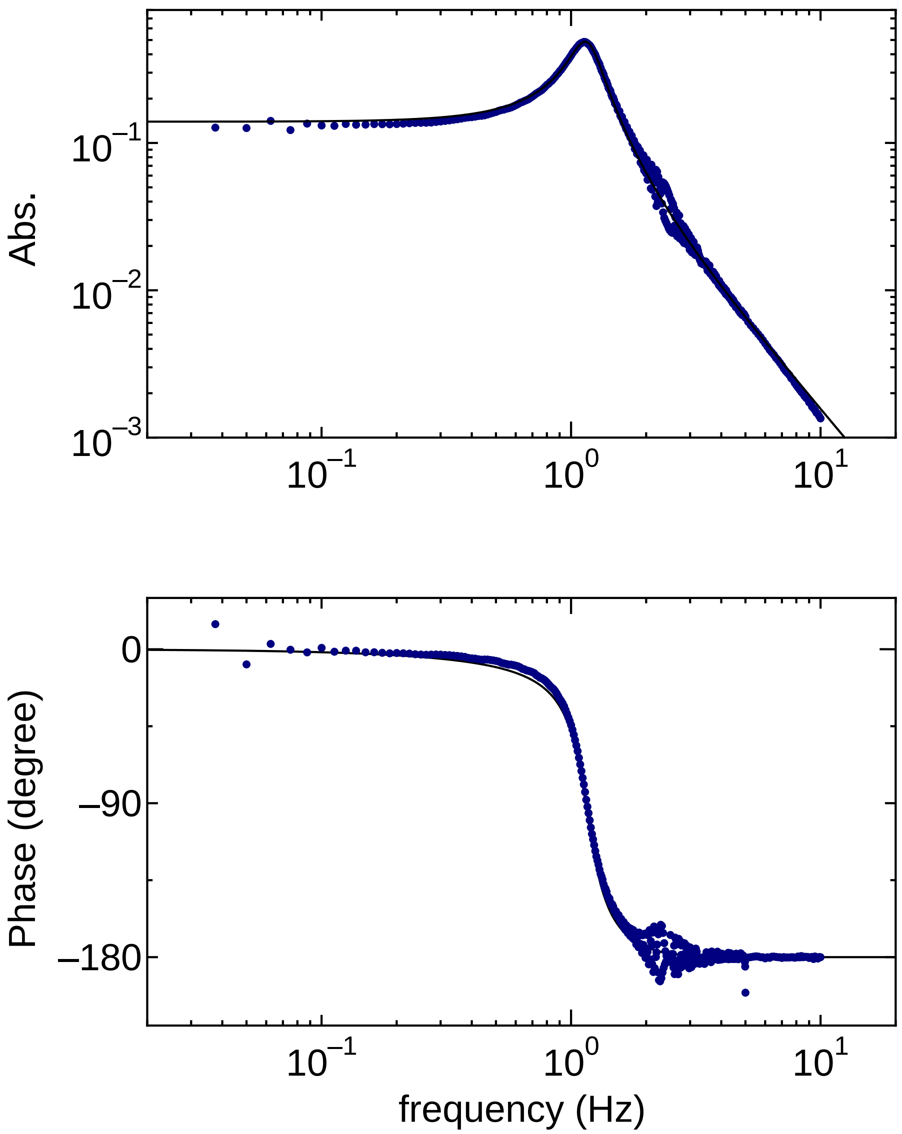

Figure 8.10: *The measured and the fitted transfer function from the input voltage of the coil driver to the motion of the test mass.*

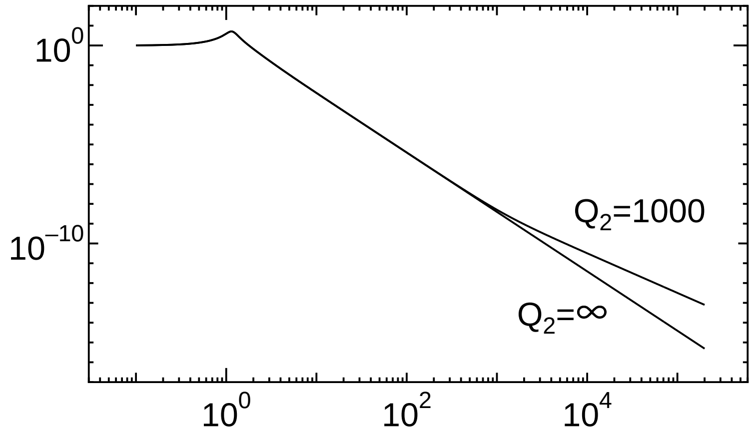

Figure 8.11: *Theoretical isolation ratio of the suspension system with the parameters obtained by the least-squares fit in Fig. 8.10. One plot is for* $Q_2 = \infty$ *and the other is for* $Q_2 = 1000$*. Since there is almost no difference in the low frequency range, the model with* $Q = \infty$ *will be used as the isolation-ratio of the system in the frequency range lower than 100Hz. Note that the real isolation ratio is believed to have been much poorer than this plot, especially in the frequency range higher than 100Hz, because there were many mechanical resonances.*

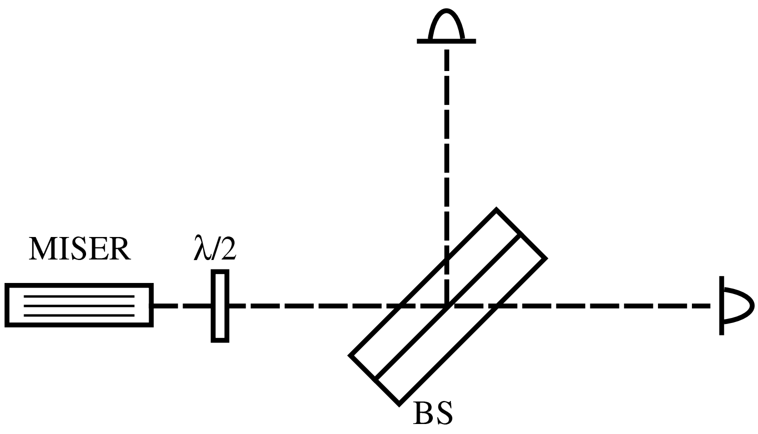

Figure 8.12: *The measurement of the polarization characteristic of the beamsplitter. The polarization of the input beam was rotated by rotating the half-wave plate which is indicated by* $\lambda/2$ *in the figure.*

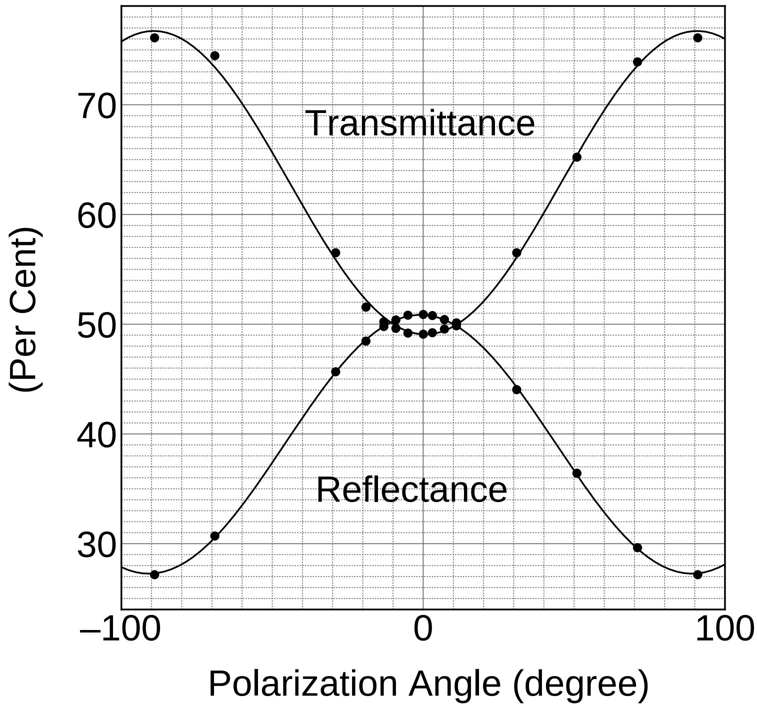

Figure 8.13: *The polarizing property of the beamsplitter. The angle of the plane of polarization of the input beam is expressed as a relative value to the angle of the S-polarization plane. Dots are the measured data and the solid lines are the fitted sinusoidal curves.*

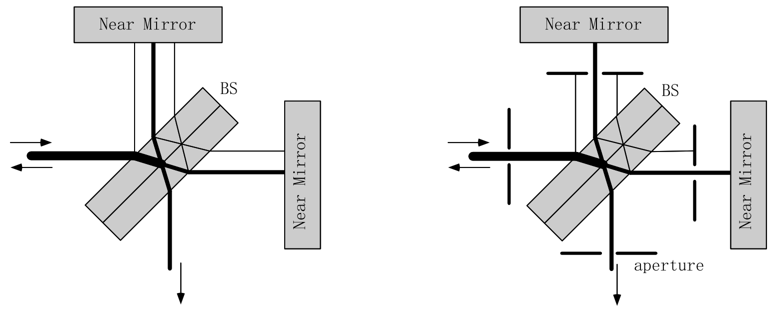

Figure 8.14: *The beams generated by the AR coats interfered with the main beams (left). Therefore baffles having small apertures were inserted to shut out the spurious paths (right).*

mirror (radius of curvature, 4.5 m; reflectance, 99.9 %). The diameter and the thickness of the mirrors are 3 cm and 5 mm, respectively.

In order to measure the finesse of each FP cavity, a sinusoidal force was applied to the test-mass to change the length of the cavity with a frequency of 2 Hz and an amplitude of typically a few micro-meters. The transmission of the cavity was monitored by a photo-diode and stored by a computer with 40 μs of sampling interval. Each large peak of the carrier appeared with two small peaks of the sidebands which originated from phase modulation at 15 MHz (Fig. 8.15). The intervals of time between a carrier peak and two sideband peaks represented as δt_1 and δt_2 in Fig. 8.15 correspond to the phase difference of $4\pi\nu_m l/c$, where ν_m, l, and c are the modulation frequency, the length of the cavity, and the speed of light, respectively. Because of the external disturbances, the phase change was not always proportional to the time change in fact. Therefore we selected the data which satisfied the condition that $\delta t_1 - \delta t_2$ must be less than 2.5 per cent of $\delta t_1 + \delta t_2$, and assumed that the time was proportional to the phase in the selected data (a more strict condition would considerably decrease the number of available data). After the selection of the data, the finesse of the cavity was calculated by applying least-squares fitting to the transmission of the carrier peak (Fig. 8.16). The finesse of the cavities under the pressure of less than 10 Pa were

$$\mathcal{F}_1 = 221 \pm 11 \tag{8.6}$$

$$\mathcal{F}_2 = 235 \pm 19 \tag{8.7}$$

where the errors are expressed as the square root of the variance (18 and 12 data of the carrier peaks were used to obtain $\mathcal{F}_1$ and $\mathcal{F}_2$, respectively). From these values, one of the parameters which represent the symmetry of the interferometer was calculated as

$$\left|\frac{\mathcal{F}_1 - \mathcal{F}_2}{\mathcal{F}_1 + \mathcal{F}_2}\right| \simeq (3.1 + 6.8 - 3.1)\ \%. \tag{8.8}$$

The length of the cavity was 2.95 m, therefore the cut-off frequency of the cavity was calculated as

$$f_{\rm c} = \frac{c}{4\mathcal{F}L_0} \sim 100\text{kHz} \tag{8.9}$$

We observed that the finesse decreased under the atmospheric pressure,

$$\mathcal{F}_{\rm atm1} = 206 \pm 4$$

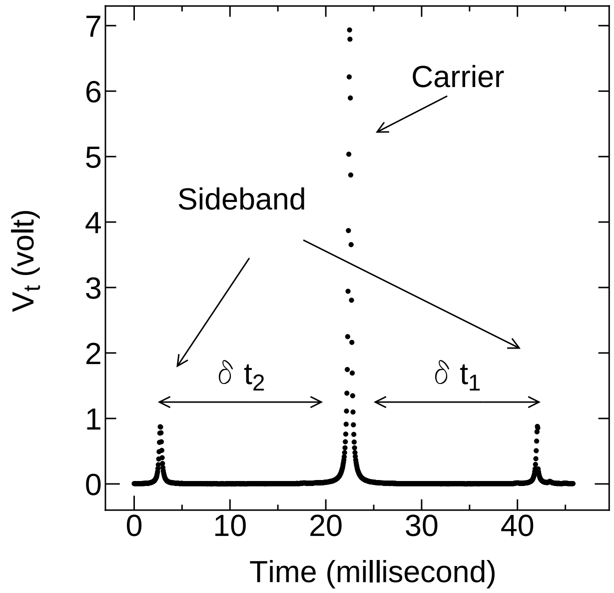

Figure 8.15: *The transmission of one of the Fabry-Perot cavities. A large peak of the carrier and two small peaks of the sidebands can be observed.*

$$\mathcal{F}_{\mathrm{atm2}} = 219 \pm 9$$

The transmittance of the cavity was measured as being 14 % which was in good agreement with the reflectance of each individual mirror.

8.4 Servo Topology

There were three important servo loops to control the interferometer; the frequency stabilization loop, the cavity locking loop, and the Michelson fringe control loop. Figure 8.17 shows the basic idea of the servo loops. If the interferometer is completely symmetric, the frequency noise of the laser doesn't appear in the phase difference between the two beams reflected from the cavities. However, in fact, there was a small asymmetry, therefore the laser frequency was stabilized using one of the cavities (parallel cavity). We call this cavity as the reference cavity. Only the DC part of the error

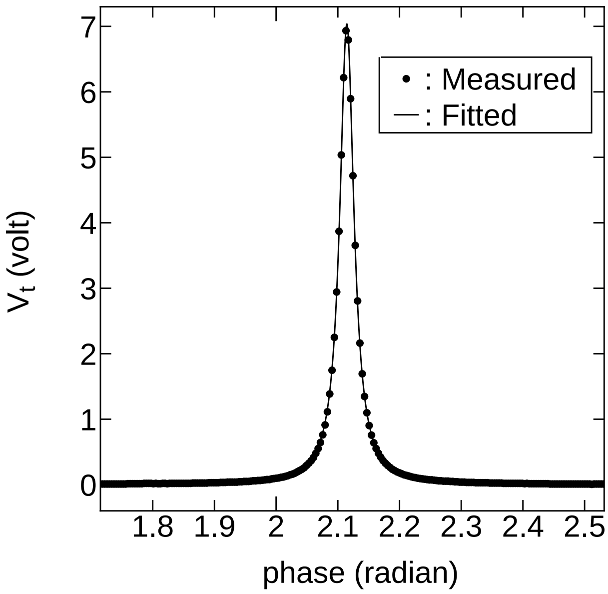

Figure 8.16: *A closer view of the peak of the carrier. Dots show the measured data and the solid line shows the fitted curve (the fitted value of the finesse was 225 in this case).*

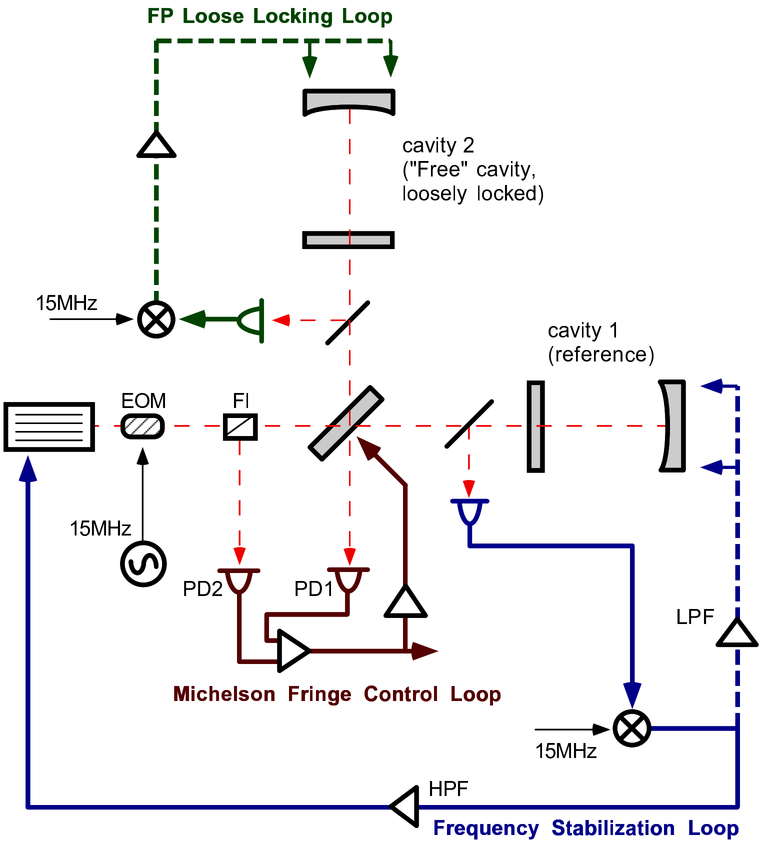

Figure 8.17: *Basic idea of the servo loops. One of the cavities was used as the phase reference of the frequency stabilization loop. The other cavity was loosely locked to the resonance. Thus the recombined beams had the phase proportional to the difference of the cavity lengths. The fringe of the recombined beams was fed back to the beamsplitter.*

signal was fed back to the reference mechanically. The other cavity which is denoted as "free cavity" in Fig.8.17 was loosely locked to the resonance by the mechanical feedback. Thus the phase difference between the two reflected beams from the cavities was proportional to the difference of the length fluctuation of the cavities. This phase difference was extracted from the recombined beams. For convenience, the homodyne technique was used. In other words, the operation point of the interferometer was chosen to the steepest slope of the fringe. To lock the Michelson fringe to the operation point, the error signal was fed back to the position of the beamsplitter.

In this section, the servo loops are studied in detail.

8.4.1 Frequency Stabilization Loop

One of the cavities was used as the reference for the frequency stabilization. Pound-Drever-Hall (P-D-H) technique [28] was used to extract the deviation of the frequency (or the cavity length) from the resonance by using the 15 MHz phase modulation. For this purpose, a small fraction (10 %) of the optical power reflected from the cavity was sent to a photo-detector. The demodulated signal was used as the error signal, and was fed back to the laser tightly. Only the DC signal was fed back mechanically to the end mirror of the cavity by using the magnet-coil actuator; the front mirror was not controlled at all.

Figure 8.18 shows the characteristic frequencies of the frequency stabilization loop. The PZT to control the frequency of the laser had a resonance at 366 kHz. To maximize the bandwidth of the PZT control loop, a notch filter with a Q of 4 was used to eliminate the large resonance peak.

The equations which governs this servo system are described as

$$\delta\nu = \delta\nu_{\mathrm{n}} - G_{\mathrm{f-PZT}}\left(\delta\nu + \frac{\nu_{\mathrm{o}}}{L_0}\delta L_1\right) \tag{8.10}$$

$$\delta L_1 = \delta L_{1\mathrm{n}} - G_{\mathrm{f-mass}}\left(\delta L_1 + \frac{L_0}{\nu_{\mathrm{o}}}\delta\nu\right) \tag{8.11}$$

where $\delta\nu$, $\delta\nu_{\mathrm{n}}$, δL_1, $\delta L_{1\mathrm{n}}$, L_0, and ν_0 are the fluctuation of the frequency with and without the stabilization, the fluctuation of the length of the reference with and without the stabilization, mean length of the cavity, and the center frequency of the laser,

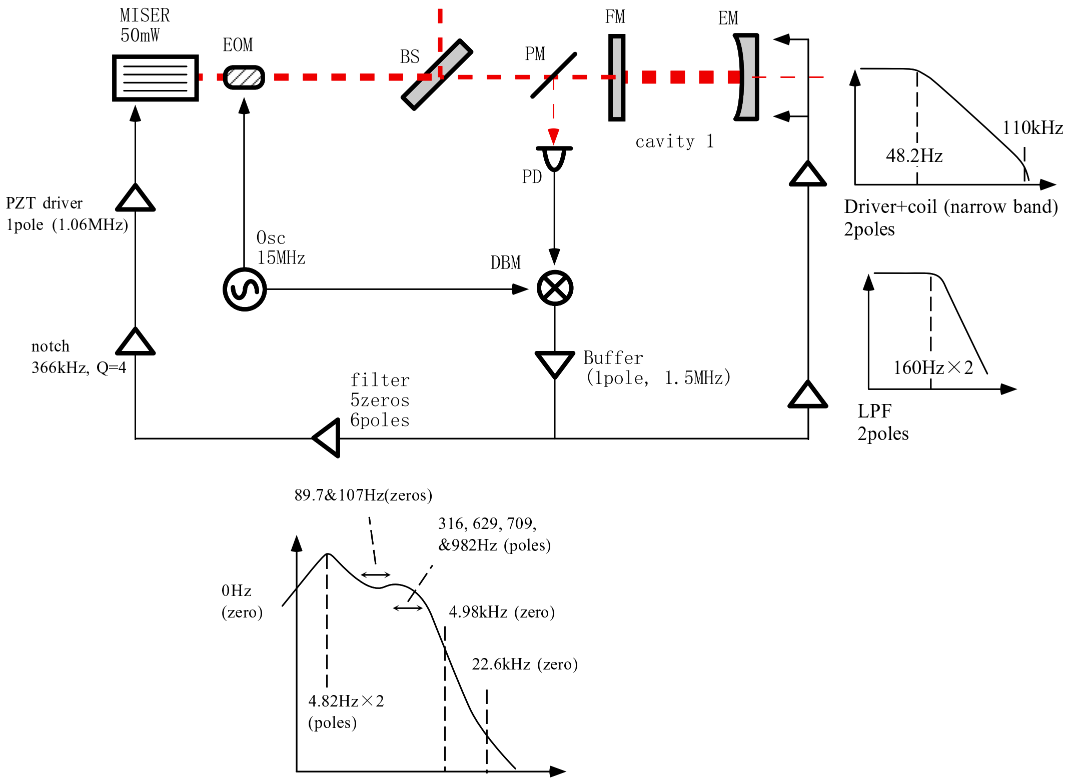

Figure 8.18: *Characteristic frequencies used in the frequency-stabilizing servo.*

respectively. Also, $G_{\mathrm{f-PZT}}$, and $G_{\mathrm{f-mass}}$ are the open-loop transfer function of the PZT- and the mass-control loop, respectively. These equations are solved as

$$\begin{aligned}
\delta\nu &= \frac{1+G_{\mathrm{f-mass}}}{1+G_{\mathrm{f-PZT}}+G_{\mathrm{f-mass}}}\delta\nu_{\mathrm{n}} - \frac{G_{\mathrm{f-PZT}}}{1+G_{\mathrm{f-PZT}}+G_{\mathrm{f-mass}}}\frac{\nu_{\mathrm{o}}}{L_0}\delta L_{1\mathrm{n}} \\
&\equiv \delta\nu_{\mathrm{stab}} - \frac{G_{\mathrm{f-PZT}}}{1+G_{\mathrm{f-PZT}}+G_{\mathrm{f-mass}}}\frac{\nu_{\mathrm{o}}}{L_0}\delta L_{1\mathrm{n}} \qquad (8.12) \\
\delta L_1 &= -\frac{G_{\mathrm{f-mass}}}{1+G_{\mathrm{f-PZT}}+G_{\mathrm{f-mass}}}\frac{L_0}{\nu_{\mathrm{o}}}\delta\nu_{\mathrm{n}} + \frac{1+G_{\mathrm{f-PZT}}}{1+G_{\mathrm{f-PZT}}+G_{\mathrm{f-mass}}}\delta L_{1\mathrm{n}} \qquad (8.13)
\end{aligned}$$

where $\delta\nu_{\mathrm{stab}}$ represents the reduced frequency-noise level. The phase fluctuation of the reflected beam from the reference cavity (which is denoted here as Ψ_1) is written as

$$\Psi_1 \propto 2k\left[\delta L_{1\mathrm{n}} + \frac{L_0}{\nu_{\mathrm{o}}}\delta\nu_{\mathrm{n}}\right]\frac{1}{1+G_{\mathrm{f-PZT}}+G_{\mathrm{f-mass}}}. \qquad (8.14)$$

The open-loop transfer function of the whole system is written as $G_{\mathrm{f-PZT}}+G_{\mathrm{f-mass}}$, but this is not the frequency stabilization gain itself. Equation 8.12 shows that the frequency of the laser is reduced by the factor of

$$\frac{1+G_{\mathrm{f-mass}}}{1+G_{\mathrm{f-PZT}}+G_{\mathrm{f-mass}}} = \frac{1}{1+\frac{G_{\mathrm{f-PZT}}}{1+G_{\mathrm{f-mass}}}}. \qquad (8.15)$$

The equivalent noise-stabilization gain G_{stab} is defined as

$$G_{\mathrm{stab}} \equiv \frac{G_{\mathrm{f-PZT}}}{1+G_{\mathrm{f-mass}}}. \qquad (8.16)$$

When the mass-loop gain is much larger than unity, G_{stab} is approximately equal to $G_{\mathrm{f-PZT}}/G_{\mathrm{f-mass}}$. Therefore, to maximize the frequency-stabilization gain, the loop gain of the mass-loop ($G_{\mathrm{f-mass}}$) had to be made as small as possible. On the other hand, since the frequency control range by using PZT was limited, it was impossible to completely remove the mass-loop because the seismic disturbance was too large to be compensated by only using frequency control. In such kind of system in general, it is practically important to make the cross-over frequency, at which the absolute value of the two loops are equal to each other, as small as possible.

In this experiment, the cross-over frequency of the PZT- and mass-control loop was designed to be 7Hz. For this purpose, special care had to be taken for the design of the feedback filter. In the frequency range larger than the first resonance at around

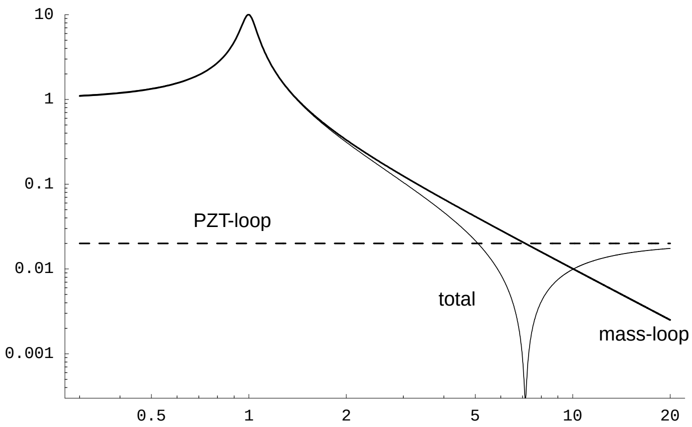

Figure 8.19: *When the feedback transfer function of PZT- and mass-loop have approximately the opposite phase at the cross-over frequency, a deep notch appears.*

1Hz, the phase delay of the transfer function of the pendulum $H_{\rm pend}$ is almost 180°. On the other hand, the response of PZT represented by $H_{\rm PZT}$ is almost flat at around several tens kHz and less. Suppose that the open-loop gain of PZT- and mass-loop is proportional to $H_{\rm PZT}$ and $H_{\rm pend}$:

$$G_{\rm f-PZT} = aH_{\rm PZT} \tag{8.17}$$

$$G_{\rm f-mass} = bH_{\rm pend}. \tag{8.18}$$

If the cross-over is at several Hz while a and b in the above equations are real, the open-loop transfer function of the whole system will have a deep notch at the cross-over frequency, because the phase of $H_{\rm PZT}$ is close to zero, while the phase of $H_{\rm pend}$ is almost close to $-180°$ (see Fig. 8.19). This will lead to a serious instability of the system.

To avoid this instability, a negative phase shift (delay) has to be added to the PZT-loop, or a positive shift has to be added to the mass-loop. Phase adjustment in the opposite sign (*i.e.* positive phase shift to the PZT-loop or delay in mass-loop) never works because the whole system does not meet the Nyquist criteria of stability in such a case. Since the mass-loop gain had to be minimized, we added a phase delay to the PZT-loop by adding two poles and one zero.

Figure 8.20 shows the measured open-loop transfer function of the whole stabilization system together with the calculated gain of the PZT-loop, mass-loop and the whole loop. The calculated curve for the mass-loop (dashed line in the Figure) was derived from the transfer function of the pendulum shown in Fig. 8.10 and the poles and zeros of the servo circuits. Only the DC gain factor was least-squares fitted. The calculated curve for PZT-loop was least-squares fitted to the measured transfer function of the whole system (dots in the figure) in the frequency range higher than 1kHz where the mass-loop was negligible. Again, the only one fitting parameter was the gain factor, and all of the poles and zeros were taken from those of the electrical circuits. The mechanical resonance of PZT was ignored here for convenience. The calculated curve for the whole system is the simple sum of the mass- and the PZT-loop. As the figure shows, the theory and the experiment agrees quite well. There still was a notch in the absolute value plot, because there were more poles in this feedback system than in the simple single pendulum system illustrated in Fig.8.19. However, due to a careful servo design, the bottom of the notch is at least more than 60dB and didn't lead to instability. The bandwidth of this servo system was about 55kHz in this plot and the phase margin was about 25°. Also a calculated plot of the equivalent frequency-noise reduction factor $G_{\mathrm{f-PZT}}/1 + G_{\mathrm{f-mass}}$, which has been obtained from the fitted transfer functions $G_{\mathrm{f-PZT}}$ and $G_{\mathrm{f-mass}}$, is shown in the figure. The equivalent reduction factor reached its maximum of 76dB at around 440Hz, and crossed the unity-gain line at about 7Hz (the cross over frequency of the two loops). A narrower mass-loop would have made the frequency-noise reduction factor larger between several tens Hz and 440Hz. However, since the frequency stability was well below the other noise levels in the interferometer (see 9.1), the mass-loop was not optimized further. A wider bandwidth was possible but was not necessary for our experiment for the same reason.

While the frequency stabilization system reduced the frequency noise, the length fluctuation of the reference cavity was also corrected by the frequency tuning. This may cause a doubt that the frequency stabilization made some problem with the length measurement which was the aim of this experiment. However, in fact this was not a problem at all. To understand the system behavior, let us consider the ideal case, i.e., $|G_{\mathrm{f-PZT}}| = \infty$ and $|G_{\mathrm{f-mass}}| = 0$. In this case, the phase fluctuation of the reflected beam caused by the length fluctuation of the reference cavity is completely compensated by the laser frequency tuning, *i.e.* $\Psi_1 = 0$. The laser frequency fluctuation is equal to

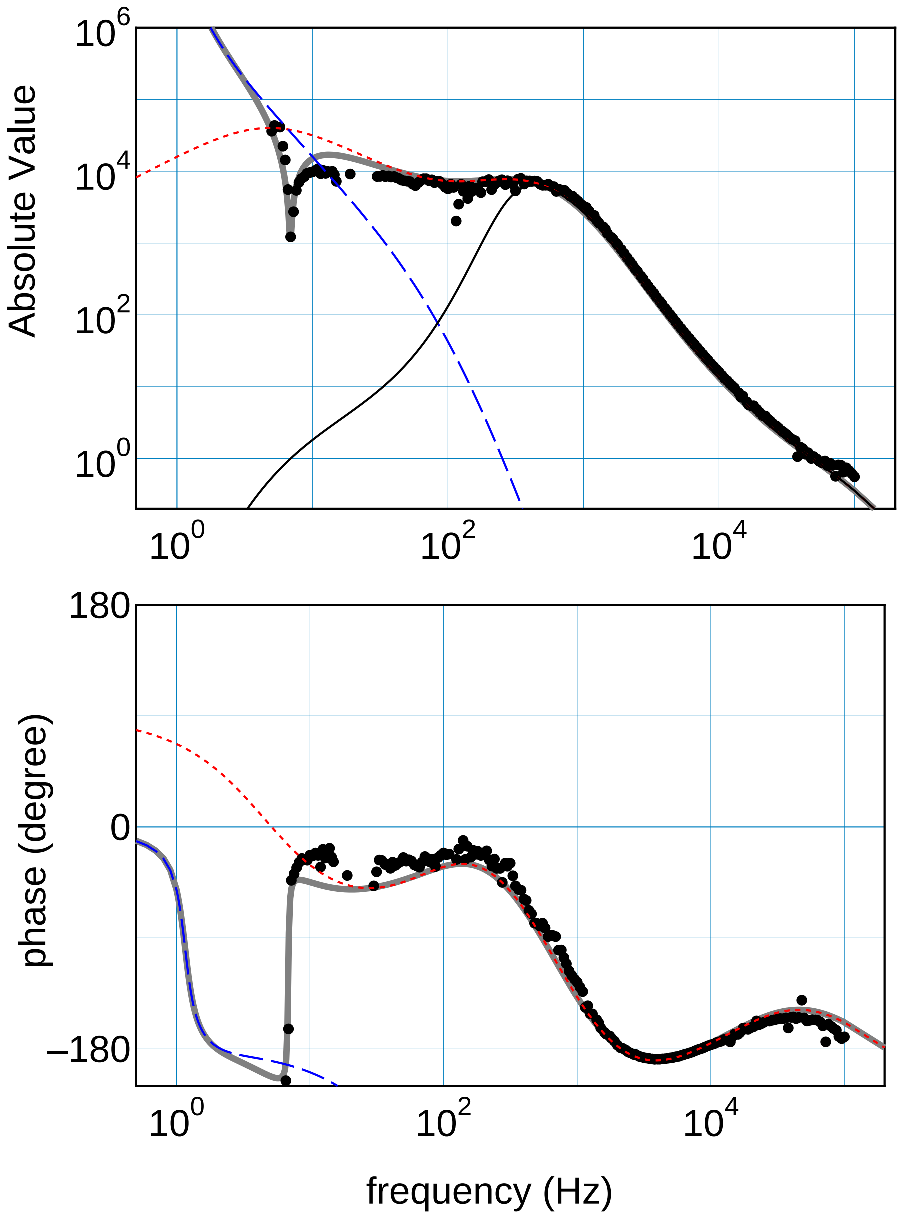

Figure 8.20: *The open-loop transfer function of the frequency stabilization system. The dots show the measured transfer function for the whole loop. The dotted line is the calculated one for the PZT-loop, with the AC gain factor least-squares fitted to the dots. The dashed line shows the calculated transfer function for the pendulum-loop. For this curve, only the DC gain factor was least-squares fitted. The thick solid line is the sum of the calculated values for pendulum- and PZT-loop, which agrees well with the measured values. The thin solid line is the equivalent frequency noise reduction factor of this servo system.*

$-\widetilde{\delta L}_1 \nu_0 / L_0$. The phase fluctuation of the reflected beam from the loosely locked cavity is always the sum of the length-originated and frequency-originated fluctuations. Since the frequency-originated one is proportional to $-\widetilde{\delta L}_1$, Ψ_2 is proportional to $-\widetilde{\delta L}_1 + \widetilde{\delta L}_2$. The purpose of the experiment is to measure the phase difference $\Psi_1 - \Psi_2$, therefore one can see that the length signal is not affected at all by the frequency stabilization. More realistic and quantitative discussions are shown in the following contexts.

8.4.2 Cavity Length Control Loop

The length of the perpendicular cavity was loosely locked to the resonance. The same signal extraction system used for the frequency stabilization was used to extract the deviation of the cavity length from the resonance. The demodulated signal was mechanically fed back to the end mirror of the cavity. Figure 8.21 shows the characteristic frequencies used in the servo. As Eq. 8.4 and Fig. 8.10 show, the phase delay of the pendulum was slightly larger than or nearly equal to 2π, therefore the control filter was basically designed as a lead-lag filter that had a positive phase shift to compensate the phase delay. The frequency of poles were 658 Hz and 2 kHz, and that of the zero was 87 Hz. Also, the coil driver for the actuator had a pole at 1026 Hz. Figure 8.22 shows the measured and the calculated open-loop transfer function of the cavity length control loop. In the 'calculated' plot, all of the poles and the zero were determined from the electronic circuit, and the only free parameter was the DC gain which was obtained from the least-squares fitting. The typical servo bandwidth of the cavity-locking loop was between 200 and 400 Hz.

The phase of the reflected light from the perpendicular cavity was corrected by the control loop as

$$\widetilde{\Psi}_2(f) \propto 2k \left[\widetilde{\delta L}_{2\mathrm{n}}(f) + L_0 \frac{\widetilde{\delta \nu}(f)}{\nu_0} \right] \frac{1}{1 + G_{\mathrm{FP}}(f)} \tag{8.19}$$

where $\delta L_{2\mathrm{n}}$ and G_{FP} denotes the fluctuation of the cavity length without the servo system and the open-loop transfer function, respectively.

When the frequency stabilization loop was turned on, the error signal of the cavity

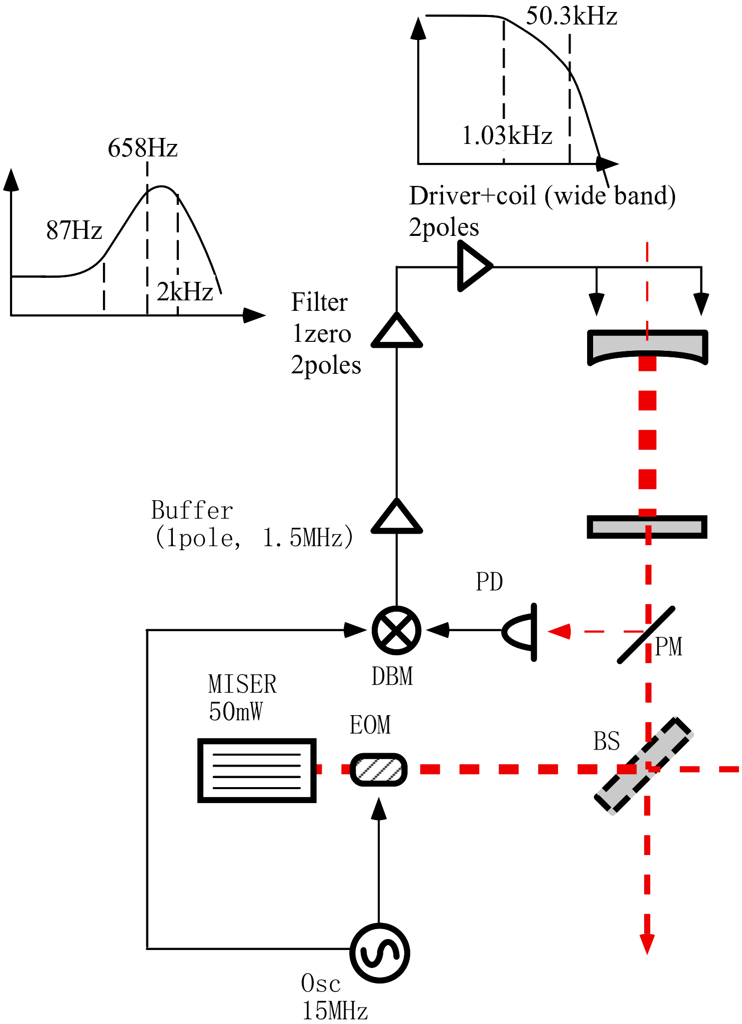

Figure 8.21: *Characteristic frequencies used in the cavity locking servo. A filter having a zero at 87 Hz was used to compensate the phase delay of the double-pendulum.*

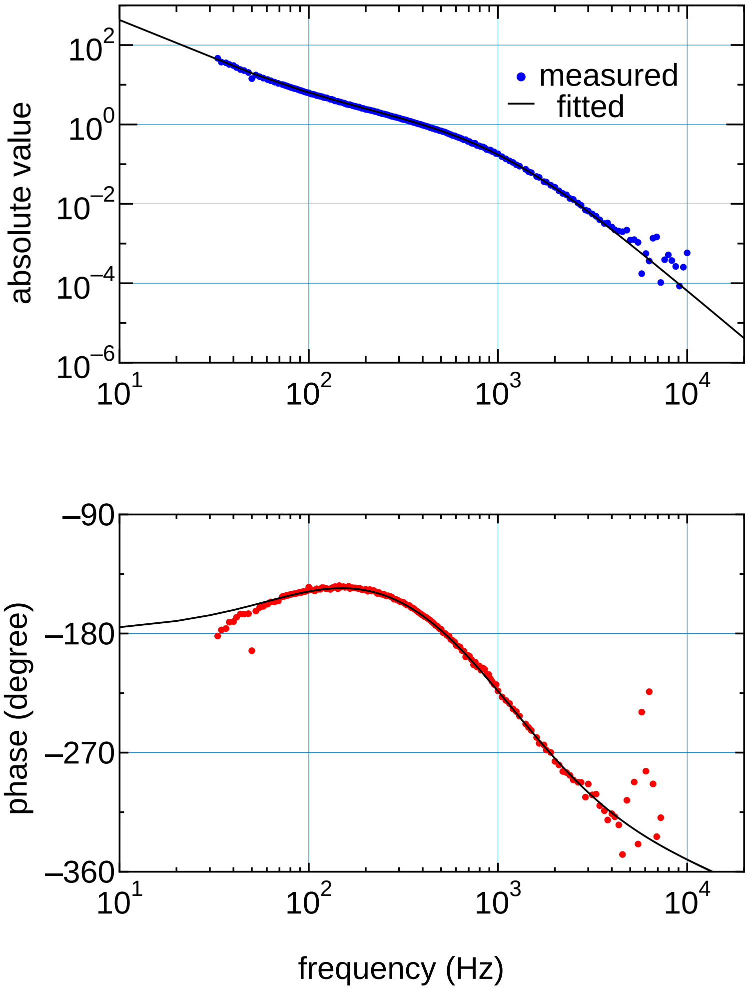

Figure 8.22: *Open-Loop transfer function of the cavity locking servo. The dots show the measured points and the line represents the calculated value. The typical servo bandwidth of the cavity-locking loop was between 200 and 400 Hz (390 Hz in this plot).*

locking system was calculated by using Eqs. 8.12 and 8.19 as

$$\begin{aligned}\tilde{v}_{\mathrm{err}}^{\mathrm{FP}} &\propto \left[\widetilde{\delta L}_{2\mathrm{n}} - \frac{G_{\mathrm{f-PZT}}\widetilde{\delta L}_{1\mathrm{n}} - (1+G_{\mathrm{f-mass}})\, L_0 \widetilde{\delta \nu}_{\mathrm{n}}/\nu_{\mathrm{o}}}{1+G_{\mathrm{f-PZT}}+G_{\mathrm{f-mass}}}\right] \frac{1}{1+G_{\mathrm{FP}}} \\ &= \left[\widetilde{\delta L}_{2\mathrm{n}} - \widetilde{\delta L}_{1\mathrm{n}} \left(1 - \frac{1}{1+G_{\mathrm{stab}}}\right) - L_0 \frac{\widetilde{\delta \nu}_{\mathrm{stab}}}{\nu_0}\right] \frac{1}{1+G_{\mathrm{FP}}}. \end{aligned} \quad (8.20)$$

One can see that the error signal is proportional to the difference of the length of the cavities if the equivalent frequency stabilization gain (G_{stab}) is much larger than unity.

8.4.3 Michelson Interferometer Fringe Control

The fringe of the Michelson interferometer was detected by using two DC-photo-detectors, one to detect the transmission of the interferometer (referred to as PD1 in Fig. 8.1) and one to detect the reflection (PD2 in Fig. 8.1). The transmission detector was placed inside the center chamber, while the reflection detector was put on the table for the input beam optics. A feedback system was used to keep the fringe at its operation-point where the optical power is equally divided to the two output ports. There was an amplifier to provide the electronic gain factor α which is defined in Eq. 6.31, even though the interferometer itself had a good symmetry. This was because the reflected beam from the interferometer was reflected three times by the aluminum plated mirrors after the recombination (see Fig. 8.2), while the transmission beam was directly detected by the photo-detector. After the correction by the electronic gain α, the difference of the two detectors were used as the error signal which was proportional to the deviation of the fringe. The error signal was filtered appropriately and fed back mechanically to the position of the beamsplitter by using coil-magnet actuator. The feedback was done tightly and the feedback signal was read-out by monitoring the current in the feedback coils: In tight-lock system one can able to reduce the noise contribution of the driver circuit, in general (see 9.1). The feedback filter was the same type as the one used for the cavity-locking, but the control bandwidth was rather large, typically from 400Hz to 1kHz. Figure 8.23 illustrates the characteristic frequencies in the feedback servo. There were two large mechanical resonance at 15kHz and 24kHz, which were identified as the resonances of the BS. Though notch

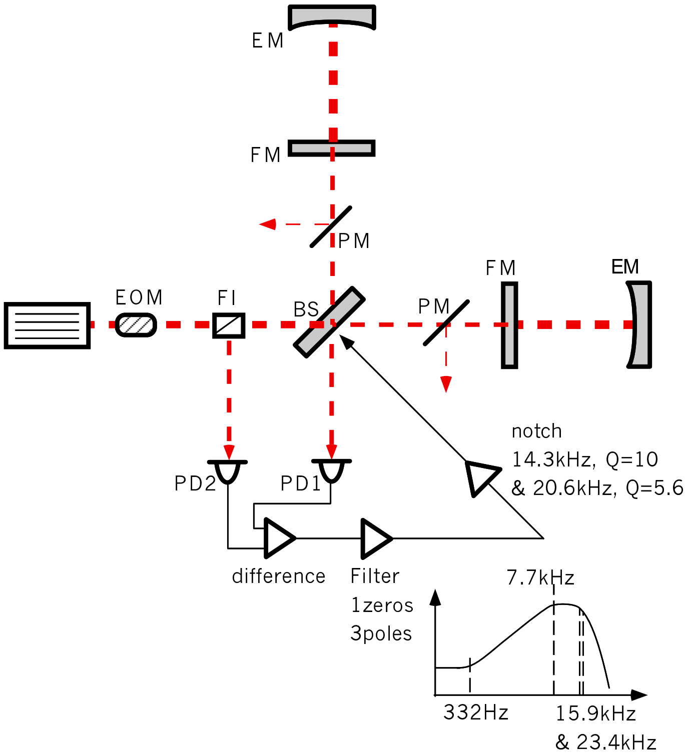

Figure 8.23: *The servo system to control the Michelson fringe.*

filters were used to suppress these peaks, these resonances still prevented the control bandwidth from being larger than about 2kHz.

Figure 8.24 is the typical open-loop transfer function of the fringe control loop. Dots are the measured data and the lines are the fitted curve. In the fitting, the only one free parameter was the DC gain. All of the poles and zeros were calculated from the electronics constants, except for the pendulum's poles which were not important here because the frequency range of interest was far above the pendulum's poles. The fitted curve and the measured data agrees quite well.

With the servo system, the measured signal is written as follows:

$$\begin{aligned} v_{\rm err}^{\rm FPM} &\propto \frac{\delta\theta_- + \delta\Psi_-}{1 + G_{\rm FPM}} \\ &= \frac{\delta\theta_- + \delta\Psi_-}{1 + G_{\rm FPM}} \end{aligned} \tag{8.21}$$

where $G_{\rm FPM}$ is the open-loop transfer function of the Michelson fringe locking servo, $\delta\Psi_- = \Psi_1 - \Psi_2$ is the cavity-originated phase difference, and $\delta\theta_-$ is the phase difference

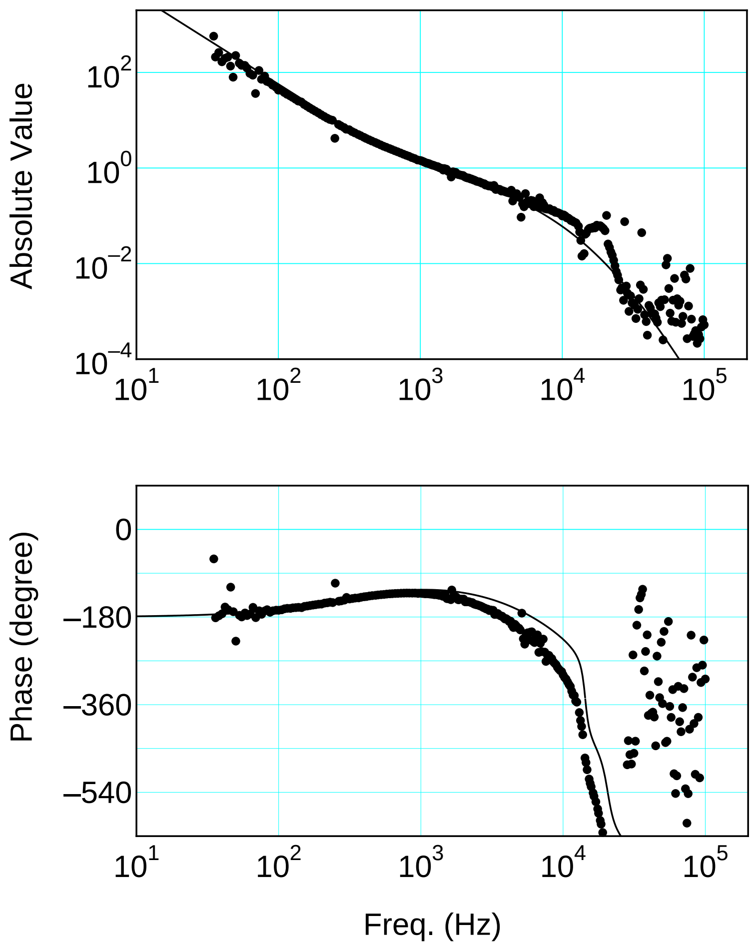

Figure 8.24: *A typical open-loop transfer function of the Michelson-fringe locking servo. Dots are the measured data and the lines are the fitted curve. In the fitting, only one free parameter was the DC gain, and the theoretical values were used for all of the poles and zeros.*

caused by the fluctuation of the length between the beamsplitter and the near mirrors. When the interferometer was operated in simple Michelson configuration comprising only the beamsplitter and the near mirrors, $\delta\Psi_-$ was considered to be zero. For the Fabry-Perot-Michelson configuration, one could ignore the $\delta\theta_-$ term, because the finesse of the cavity was large enough (about 230). In this case, the error signal was calculated by using Eqs. 8.19, 8.12, and 8.14, together with Eq. 8.21 as

$$\begin{aligned}
\tilde{v}_{\mathrm{err}}^{\mathrm{FPM}} &\propto \left[\frac{\widetilde{\delta L}_{1\mathrm{n}} + L_0\widetilde{\delta\nu}_{\mathrm{n}}/\nu_{\mathrm{o}}}{1+G_{\mathrm{f-PZT}}+G_{\mathrm{f-mass}}} - \frac{\widetilde{\delta L}_{2\mathrm{n}} + L_0\widetilde{\delta\nu}/\nu_0}{1+G_{\mathrm{FP}}}\right]\frac{1}{1+G_{\mathrm{FPM}}} \\
&= \left[\widetilde{\delta L}_{1\mathrm{n}}\left(1-2\gamma_{\mathrm{m}}^{\mathrm{s}}\right) - \widetilde{\delta L}_{2\mathrm{n}} - \gamma_{\mathrm{f}}^{\mathrm{s}} L_0 \frac{\widetilde{\delta\nu}_{\mathrm{stab}}}{\nu_0}\right]\frac{1}{\left(1+G_{\mathrm{FPM}}\right)\left(1+G_{\mathrm{FP}}\right)} \\
&= \left[\widetilde{\delta L}_{-}\left(1-\gamma_{\mathrm{m}}^{\mathrm{s}}\right) - \gamma_{\mathrm{m}}^{\mathrm{s}}\widetilde{\delta L}_{+} - \gamma_{\mathrm{f}}^{\mathrm{s}} L_0 \frac{\widetilde{\delta\nu}_{\mathrm{stab}}}{\nu_0}\right]\frac{1}{\left(1+G_{\mathrm{FPM}}\right)\left(1+G_{\mathrm{FP}}\right)} \qquad (8.22)
\end{aligned}$$

where $\gamma_{\mathrm{m}}^{\mathrm{s}}(f)$ and $\gamma_{\mathrm{f}}^{\mathrm{s}}(f)$ are the asymmetry factors for the motion of the mirror and for the frequency noise which were introduced into the system by the feedback. The definition of these factors are as follows:

$$\gamma_{\mathrm{m}}^{\mathrm{s}}(f) \equiv \frac{G_{\mathrm{f-mass}}(f) - G_{\mathrm{FP}}(f)}{2\left[1+G_{\mathrm{f-mass}}(f)+G_{\mathrm{f-PZT}}(f)\right]} \qquad (8.23)$$

$$\gamma_{\mathrm{f}}^{\mathrm{s}}(f) \equiv \frac{G_{\mathrm{f-mass}}(f) - G_{\mathrm{FP}}(f)}{1+G_{\mathrm{f-mass}}(f)}. \qquad (8.24)$$

Figure 8.25 shows the typical absolute value of these asymmetry factors, which were derived from the fitted transfer functions in Figs. 8.22 and 8.20.

8.5 Calibration of the Signal-Extraction and the Feedback System

To evaluate the displacement sensitivity of the interferometer, it was necessary to calibrate both the signal-extraction system and the feedback actuators. The calibration process was done step by step, beginning from the simplest configuration to the more complex ones. The interferometer was calibrated whenever the displacement sensitivity spectrum was measured, even though the interferometer was fairly stable and the voltage-displacement conversion factor obtained by the calibration didn't significantly change for a long period.

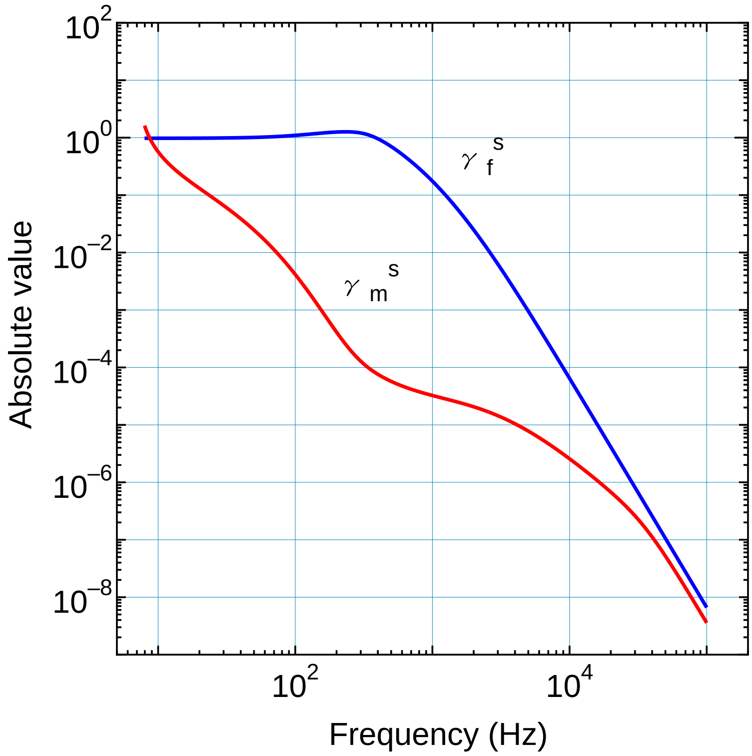

Figure 8.25: *The asymmetry factor for the motion of the mass ($\gamma_{\rm m}^{\rm s}$) and for the frequency noise ($\gamma_{\rm f}^{\rm s}$) introduced by the feedback system.*

8.5.1 Calibration of the Near Mirror Actuators by Using the Simple Michelson Configuration

First, the optical paths for the Fabry-Perot cavity were shut by using the gate-valve at the joint of the tube and the tank. The interferometer was operated in a simple Michelson configuration. The feedback circuit for the Michelson fringe-locking was turned off, and the beamsplitter was driven by the slowly changing (typically 3Hz or smaller) signal with relatively large amplitude (typically several fringes peak-to-peak). The maximum and the minimum voltage of the error signal, denoted as $V_{\mathrm{MI}}^{\mathrm{max}}$ and $V_{\mathrm{MI}}^{\mathrm{min}}$ were recorded. The absolute values of these were almost the same, $V_{\mathrm{max}}^{\mathrm{MI}} = -V_{\mathrm{min}}^{\mathrm{MI}}$. Then the feedback circuit was turned on to lock the fringe to its operation point. In this condition, the error signal was approximated by

$$\begin{aligned} v_{\mathrm{error}}^{\mathrm{MI}} &= V_{\mathrm{max}}^{\mathrm{MI}} \sin 2k\delta l_{-} && (8.25) \\ &\sim 2V_{\mathrm{max}}^{\mathrm{MI}} k\delta l_{-} && (8.26) \end{aligned}$$

where k and δl_{-} are the wave number of the laser and the fluctuation of the Michelson path difference. Thus the displacement-to-voltage conversion ratio of the simple Michelson interferometer was

$$\frac{\mathrm{d}v_{\mathrm{error}}^{\mathrm{MI}}}{\mathrm{d}l_{-}} = 2V_{\mathrm{max}}^{\mathrm{MI}} k. \tag{8.27}$$

The open-loop transfer function of the fringe locking servo was measured in this configuration. A small sinusoidal calibration signal with the frequency of 3kHz was added to one of the front mirrors[5], and the amplitude of the error signal $v_{\mathrm{cal}}^{\mathrm{MI}}$ at the calibration frequency was measured by using a spectrum analyzer (Fig. 8.26). From this value, we could know the displacement amplitude of the calibration signal by using the equation

$$\delta x_{\mathrm{cal}} = \frac{v_{\mathrm{cal}}^{\mathrm{MI}}}{2V_{\mathrm{max}}^{\mathrm{MI}} k} \left|1 + G_{\mathrm{MI}}\right|_{f=3\mathrm{kHz}}. \tag{8.28}$$

Both of the front mirrors were calibrated by the same method.

[5]The calibration frequency, 3kHz, was carefully chosen to avoid any mechanical resonances while minimizing the effect of the mechanical feedback.

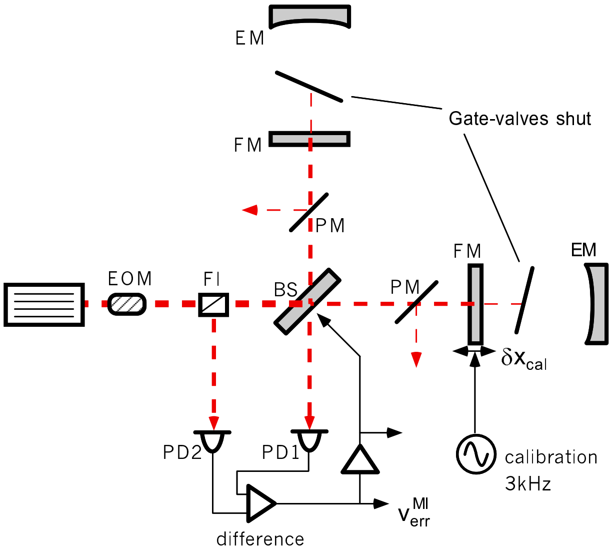

Figure 8.26: *For the calibration of the interferometer, the simple Michelson configuration was used at first. A small calibration voltage was used to drive one of the front mirrors at 3kHz.*

8.5.2 Calibration of the Displacement Sensitivity of the Single Fabry-Perot Cavity

After the calibration of the near-mirror actuators, the optical paths of the FPs were opened. The frequency stabilization loop and FP loose locking loop were closed in this order, while the Michelson locking loop was opened[6]. The open-loop transfer function of the cavity-locking servo was measured. The same calibration signal as used in the simple Michelson configuration was applied to the near mirror of the loosely-locked cavity (Fig. 8.27). The Fabry-Perot locking error signal $v_{\rm cal}^{\rm FP}$ at 3kHz was measured by using servo analyzer. The amplitude of the mirror motion caused by the calibration signal was thought to be the same as that in the simple Michelson configuration. Therefore, by comparing the calibration displacement $\delta x_{\rm cal}$ with the error signal, the displacement-to-voltage conversion factor for the Fabry-Perot signal extraction system

[6]The frequency stabilization was not essential for the calibration purpose. Nevertheless it was useful to maximize the SNR of the measurement by suppressing the frequency noise.

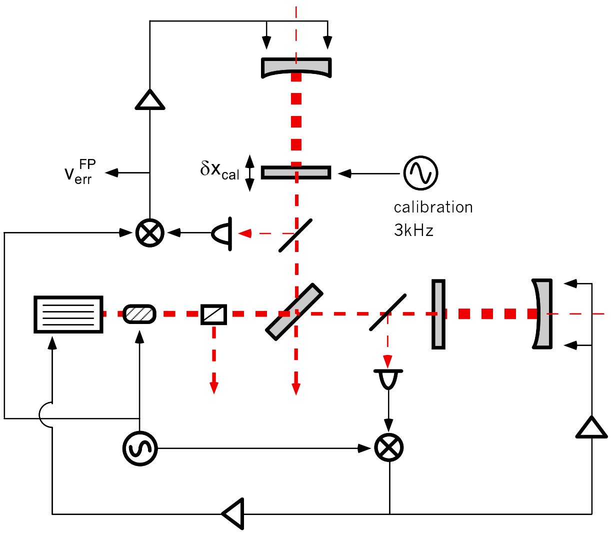

Figure 8.27: *The same calibration voltage as used in the simple Michelson configuration was used for the calibration of the single Fabry-Perot cavity. The typical value for this was* 10^{10}volt/m.

was obtained:

$$\frac{\mathrm{d}v_{\mathrm{err}}^{\mathrm{FP}}}{\mathrm{d}L} = \frac{v_{\mathrm{cal}}^{\mathrm{FP}}}{\delta x_{\mathrm{cal}}} \left|1 + G_{\mathrm{FP}}\right|_{f=3\mathrm{kHz}} \tag{8.29}$$

where δL and G_{FP} is the length of the cavity and the open-loop transfer function of the loose-locking servo of the cavity. Both of the cavities were calibrated by the same procedure.

8.5.3 Calibration of the Displacement Sensitivity of the Fabry-Perot-Michelson Interferometer

The frequency stabilization loop and FP loose locking loop were closed in this order, while the Michelson locking loop was opened. Just in the same way as the simple Michelson configuration, the maximum and the minimum voltage of the error signal, $V_{\mathrm{FPM}}^{\mathrm{max}}$ and $V_{\mathrm{FPM}}^{\mathrm{min}}$, were measured while BS was driven with a large amplitude[7]. After the Michelson fringe locking servo was closed, the open-loop transfer function of the three

[7]The measurement of $V_{\mathrm{FPM}}^{\mathrm{max}}$ and $V_{\mathrm{FPM}}^{\mathrm{min}}$ wasn't directly related with the calibration, but by using this value we could check the consistency of the fringe voltage with the reflectance of the cavity and the open-loop transfer function.

loops (frequency control, FP loose lock, and Michelson lock) were measured. Because the reflectance of the FP was smaller than that of the front mirror, the open-loop transfer function of the Michelson fringe control loop was smaller in this configuration than in the simple Michelson configuration. The same calibration voltage as used in simple Michelson configuration was applied to one of the front mirrors (Fig. 8.28). The Michelson error signal voltage denoted as $v_{\rm cal}^{\rm FPM}$ at the calibration frequency was measured by using the spectrum analyzer (Advantest, R9211). From this value, one could obtain the displacement-to-voltage conversion factor as expressed in the following equation:

$$\frac{\mathrm{d}v_{\rm err}^{\rm FPM}}{\mathrm{d}L_-} = \frac{v_{\rm cal}^{\rm FPM}}{\delta x_{\rm cal}} \left|(1+G_{\rm FPM})(1+G_{\rm FP})\right|_{f=3\rm kHz} \tag{8.30}$$

where $\delta v_{\rm err}^{\rm FPM}$, δL_-, $G_{\rm FPM}$, and $G_{\rm FP}$ are the error signal of the Michelson fringe of FPM, the differential fluctuation of the length of the arm cavities, the open-loop transfer function of the Michelson fringe locking loop of FPM, and the open-loop transfer function of loose FP locking loop. For our experiment, this factor was typically 10^{10}V/m. In the above equation the frequency stabilization loop was ignored, because the gain of the PZT-control was much larger than that of the mass-control in the frequency stabilization loop at the calibration frequency, thus there was almost no phase modification by this loop.

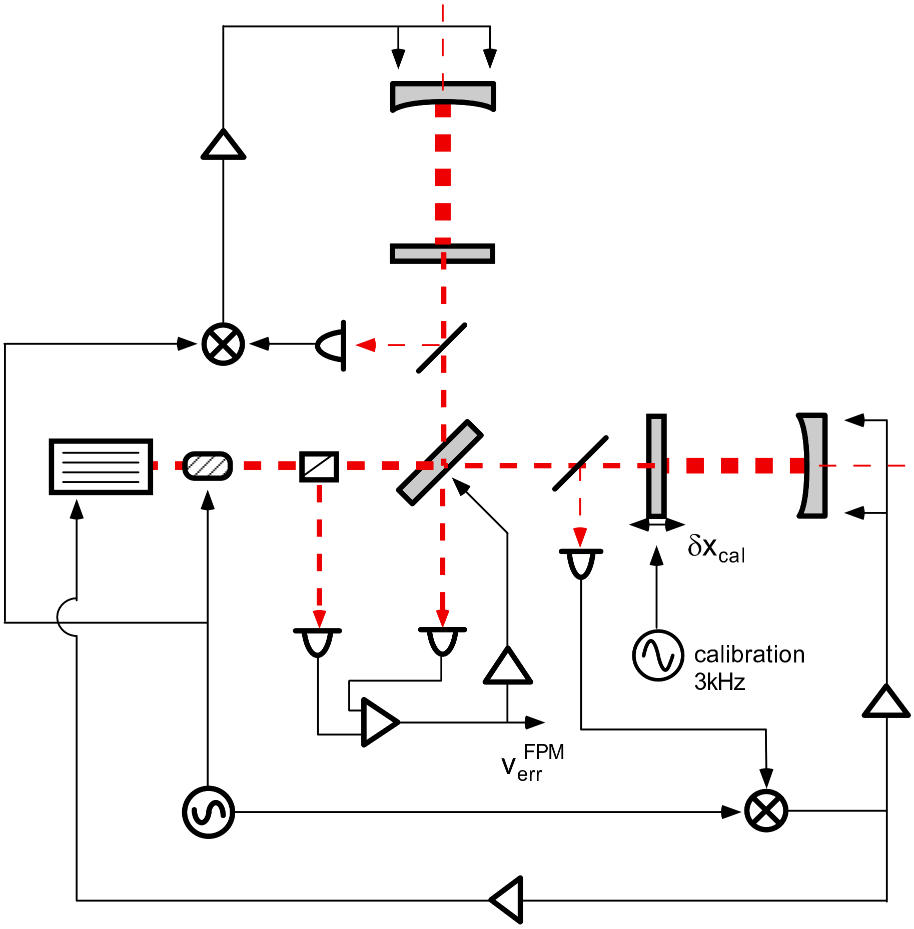

Figure 8.28: *In the full FPM configuration, the same calibration voltage as used in the simple Michelson configuration was used to drive one of the front mirrors at 3kHz. The amplitude of the error signal of the Michelson fringe of the FPM was compared with that of the simple Michelson configuration. Taking into account the effects of the open-loop transfer function, the displacement-to-voltage factor of the interferometer was obtained. The typical value for this was* 10^{10} V/m.

9. Displacement Sensitivity and the Noise Analysis

In this chapter, the noise level in the displacement sensitivity of the interferometer is studied. The measured noise level and the identification of the noise sources are shown.

9.1 Displacement Sensitivity of the Interferometer

To evaluate the displacement sensitivity of the Fabry-Perot-Michelson interferometer, the noise-spectrum of the feedback signal of the Michelson fringe locking servo was measured as the current in the feedback actuator by using the spectrum analyzer, while the interferometer was in operation. All of the calibration measurement described in the preceding section were done. The feedback signal $v_{\mathrm{fed}}^{\mathrm{FPM}}$ was measured using the spectrum analyzer. Combining this signal with Eq.8.22, putting zero to all of the terms except for the differential fluctuation δL_{-}, the displacement spectrum of δL_{-} was obtained as

$$\widetilde{\delta L}_{-}(f) = \left(\frac{\mathrm{d}v_{\mathrm{err}}^{\mathrm{FPM}}}{\mathrm{d}L_{-}}\right)^{-1} \frac{|1+G_{\mathrm{FPM}}(f)|\cdot|1+G_{\mathrm{FP}}(f)|}{|G_{\mathrm{filt}}|\cdot|1-\gamma_{\mathrm{m}}^{\mathrm{s}}|} v_{\mathrm{fed}}^{\mathrm{FPM}} \tag{9.1}$$

where G_{filt} is the transfer function of the feedback filter from the error point to the feedback point of the Michelson fringe locking servo. In the calculation above, the measured value of the transfer functions were used whenever it was possible. "Fitted" transfer functions were used only in the frequency range where it was difficult to measure the correct transfer functions (*i.e.* below 10Hz). For the asymmetry factor originating from the servo system represented by $\gamma_{\mathrm{m}}^{\mathrm{s}}$, the calculated value shown in Fig.8.25 was used, since it was impossible to directly measure it.

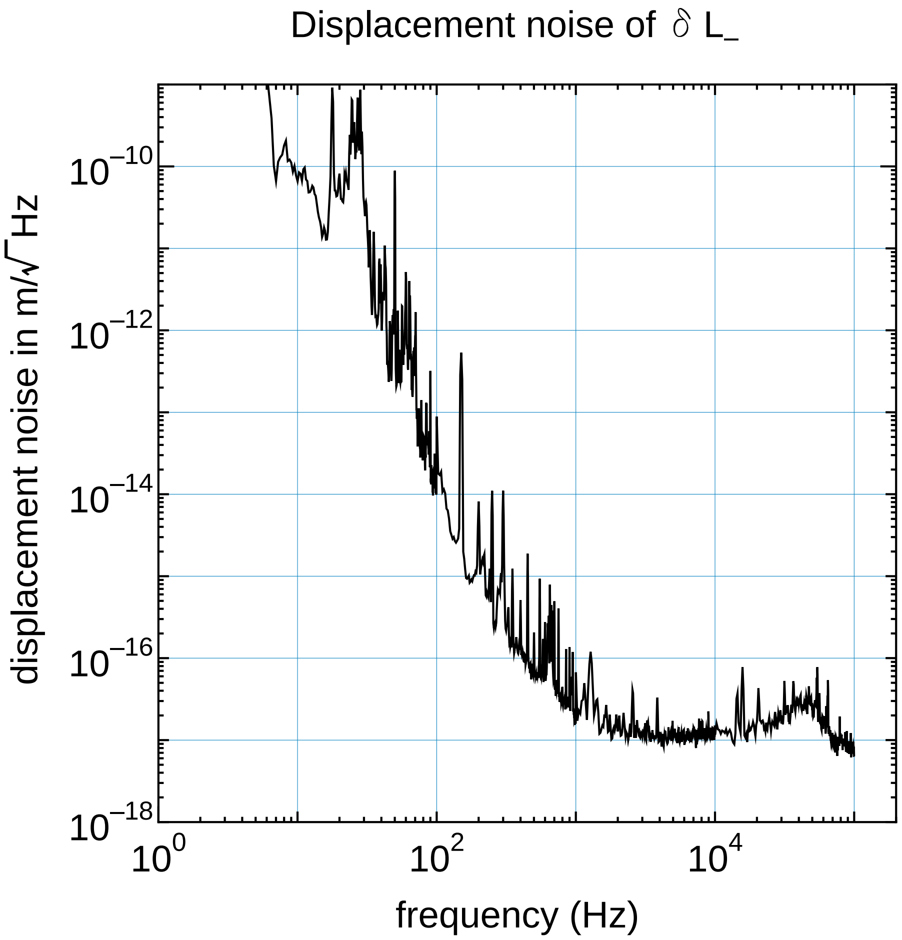

Figure 9.1: *The displacement noise spectrum for δL_- of the 3m Fabry-Perot-Michelson interferometer.*

Figure 9.1 shows the obtained displacement noise for δL_-. There are three major noise sources in 3-meter interferometer; the seismic-induced displacement of the mirror, frequency noise of the laser, and the photon shot noise. There are also many noise sources related to the signal extraction and control system. All of these noise sources are described in detail in the following sections.

9.2 Seismic-Induced Noise

The mirrors of the interferometer are driven by the seismic motion, even though they are isolated from such disturbances by suspension system. The seismic motion of the campus of the University of Tokyo approximately follows the "standard" formula [29]

$$\tilde{y}(f) = \left(\frac{1\mathrm{Hz}}{f}\right)^2 \times 10^{-7} \quad \mathrm{m}/\sqrt{\mathrm{Hz}} \tag{9.2}$$

in the frequency range between 10^{-1} and 1kHz [30], where $\tilde{y}$ is the power-spectral density of the seismic motion. The seismic-induced displacement of the mirrors is related to the seismic motion as

$$\tilde{x}_{\mathrm{seism}} = H_{\mathrm{isol}}\tilde{y} \tag{9.3}$$

where H_{isol} is the isolation ratio of the suspension system. Putting the theoretical values of Eq.8.5 and Eq. 9.2 into the above equation, we can obtain the expected amplitude of the seismic-induced noise for one mirror. If we assume that the motion of the mirrors were independent from each other, the seismic-induced noise of the interferometer was calculated to be factor two larger than x_{seism}.

On the other hand, the seismic-induced noise was able to evaluate by measuring the displacement noise spectra of the interferometer in two configurations.

Noise spectra of a simple Michelson interferometer.

In the simple Michelson interferometer comprising BS and the two front mirrors, the error signal $\tilde{v}_{\mathrm{err}}^{\mathrm{MI}}(f)$ of the fringe-locking servo was measured by using spectrum analyzer. The error signal was corrected by the open-loop transfer function of the fringe locking servo G_{MI}. The displacement-to-voltage conversion factor for a simple Michelson configuration given by Eq. 8.27 was used to obtain the displacement noise of the simple Michelson interferometer as

$$\widetilde{\delta l}_{-}(f) = \tilde{v}_{\mathrm{err}}^{\mathrm{MI}}(f)\left(\frac{\mathrm{d}v_{\mathrm{err}}^{\mathrm{MI}}}{\mathrm{d}l_{-}}\right)^{-1}|1 + G_{\mathrm{MI}}(f)|\,. \tag{9.4}$$

Noise spectrum of the Fabry-Perot locking system.

When the frequency control loop was turned on, the error signal of the perpendicular cavity was written by Eq. 8.20. Assuming that the seismic fluctuation for the two cavities were of the same amplitude and were independent from each other, one can calculate the seismically-induced noise for the differential motion using Eq. 8.20:

$$\widetilde{\delta L}_{-}(f) = \tilde{v}_{\rm err}^{\rm FP}(f)\left(\frac{{\rm d}v_{\rm err}^{\rm FP}}{{\rm d}L}\right)^{-1}|1+G_{\rm FP}(f)|\sqrt{\frac{2}{1+|1-1/\left[1+G_{\rm stab}(f)\right]|^2}} \tag{9.5}$$

All of the above mentioned three power-spectra were plotted together with the displacement noise of Fabry-Perot-Michelson interferometer in Fig. 9.2. The FPM signal agreed well with the FP locking signal from 10 to several hundreds hertz. For the simple Michelson configuration, it was possible to evaluate the seismic-induced noise level only below 100 Hz because the sensitivity was poor, but the spectrum also agreed with the FPM signal from 10 to several tens hertz. From the fact that the signals obtained by the different phase sensing system agreed well with each other, the noise of the FPM interferometer between ten and hundred hertz range was identified as seismic-induced noise. In this range, the spectrum didn't agree with the "theoretical" noise, because of the resonances of the suspension (mainly vertical) which appears as the large peaks at around 18 and 28 Hz in Fig. 9.2[1].

On the other hand, the "theoretical", the MI, and the FP signals agreed well below 10Hz, while FPM signal was much larger. However, this does not mean that the FPM was much noisier than MI or FP in the lower frequency region. This was because the length between the beamsplitter and the near mirrors were ignored when the FPM was calculated. In calculating Eqs. 8.22 and 9.1, the $\delta\theta_{-}$ term in Eq. 8.21 was ignored on the assumption that the phase change caused by cavity-length fluctuation was much larger than that by the Michelson path fluctuation. Since the phase change caused by the cavity was corrected by the FP locking servo, this assumption is not true if the control gain of the FP locking loop was larger than or comparable to the finesse of the cavity. Though the FP loose-locking servo was designed to be as low-gain as possible, it was not possible to ignore this effect in the low frequency range. Figure 9.3 shows the raw feedback voltage of the beamsplitter in MI and FPM configuration in the low frequency range. The plot shows that the spectrum for the two configuration were at the same level. Because the fringe control gain was much larger than unity, the same voltage in this plot means that the phase fluctuation which had to be compensated by the beamsplitter control for MI and FPM configuration were at the same level. Therefore

[1] These peaks were difficult to measure with photo-sensor measurement (Fig. 8.10).

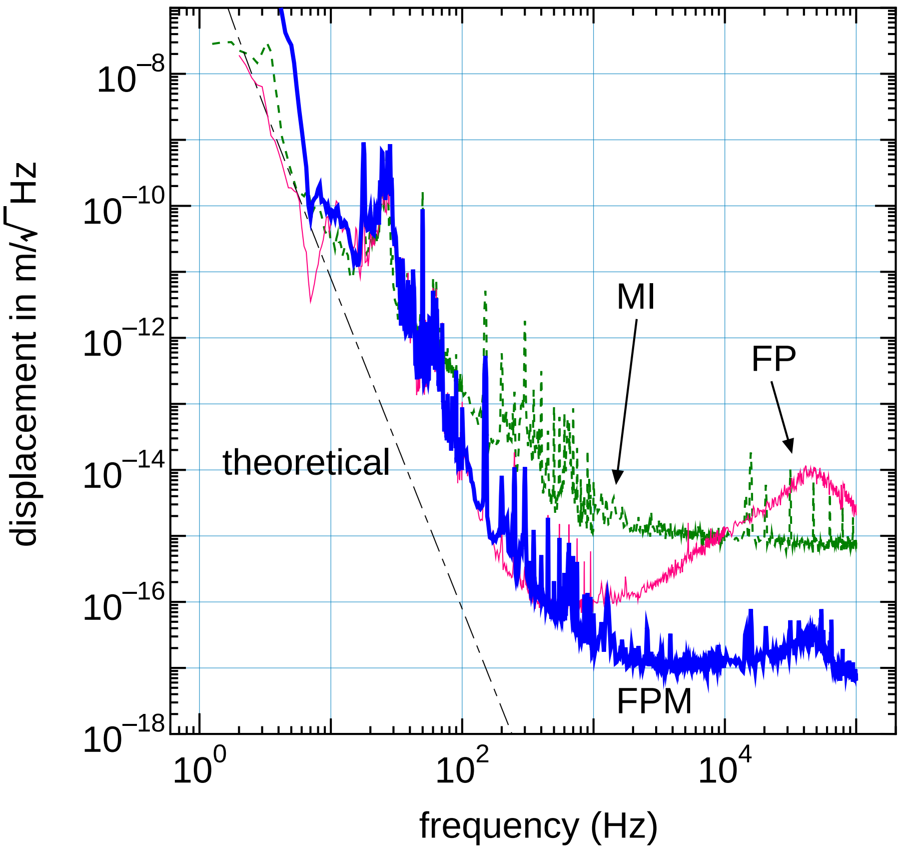

Figure 9.2: *Displacement noise spectra of the FPM (thick solid line), the MI (thin dotted), and the FP (thin solid) configuration. The thin dashed line is the "theoretical" line calculated from the seismic vibration formula and the ideal isolation ratio of the system. From the fact that the signals obtained by the different phase sensing system agreed well with each other, the noise of the FPM interferometer between 10 and 100 hertz range was identified as seismic-induced noise. There were resonances of the suspension system (mainly vertical) which appears as the large peaks at around 18 and 28 Hz in this plot. (The difference between the FPM signal and others in the frequency range below 10Hz will be discussed in the next plot.)*

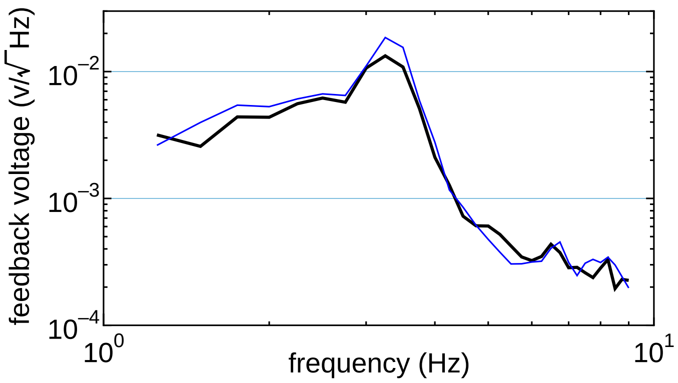

Figure 9.3: *Raw feedback voltage of the Michelson fringe locking servo, i.e. the voltage applied to the actuator of the beamsplitter, for MI (thin line) and FPM (thick) configuration. The same voltage in this plot means that the phase fluctuation which had to be compensated by the beamsplitter control for MI and FPM configuration were at the same level. This strongly indicates that the FPM signal was dominated by the Michelson path fluctuation (δl_-) in the frequency range lower than 10Hz.*

one can conclude that the spectrum of the FPM configuration was actually dominated by the fluctuation of the Michelson path in the frequency range lower than 10Hz; the vibration of the mirrors of FPM was at the same level as MI, FP, and "theoretical" level, but the finite servo gain of the FP loose locking system suppressed the cavity-originated signal, which added the relative weight to the Michelson-originated signal. This was not a problem at all in this experiment because the frequency where this effect had to be counted was rather low.

To summarize the above discussions, the noise spectrum of the FPM interferometer was dominated by seismic-induced motion of the mirrors in the frequency range below 100 Hz. Because of the finite control gain of the FP loose locking system, the seismic-induced fluctuation of the Michelson path length (δl_-) dominated the spectrum, but this was in the lowest frequency band of the measurement (*i.e.* below 10Hz).

9.3 Frequency Noise and Common-Mode-Rejection

If the interferometer was completely symmetric, the frequency fluctuation of the laser would not be the noise source to the differential phase measurement. However, since there were optical asymmetry as well as the servo asymmetry, the frequency noise appeared in the displacement spectrum of the FPM interferometer, in the high frequency range. Here, the frequency noise and the CMRR of the interferometer are studied.

9.3.1 Frequency Noise Spectra Obtained by Using Two Cavities

Frequency noise of the laser was evaluated from the error signal of the frequency stabilization servo as well as that of the FP loose locking servo. The error signals were measured with and without the frequency stabilization, thus the noise corresponding to the free-running and frequency-stabilized laser were obtained. First, the reference cavity was locked to the resonance loosely by only using mechanical feedback using the same feedback filter as used in the FP loose locking servo. The spectrum was corrected by the measured open-loop transfer function to give the frequency fluctuation of the free-running laser as

$$\widetilde{\delta\nu}_{\mathrm{free}}(f) = \nu_0 \frac{v_{\mathrm{free}}^{\mathrm{FP1}}(f)}{L_0} \left(\frac{\mathrm{d}v_{\mathrm{err}}^{\mathrm{FP1}}}{\mathrm{d}L} \right)^{-1} |1 + G_{\mathrm{FP1}}(f)| \tag{9.6}$$

With this free-running noise and the measured open-loop transfer function of the frequency stabilizing loop, the expected error signal of the frequency-stabilized system would be calculated as

$$\widetilde{\delta\nu}^{\mathrm{calc}}_{\mathrm{err-stab}}(f) = \frac{\widetilde{\delta\nu}_{\mathrm{free}}(f)}{|1 + G_{\mathrm{f-mass}}(f) + G_{\mathrm{f-PZT}}(f)|}. \tag{9.7}$$

When the frequency stabilization loop was turned on, the error signal of the stabilization loop as well as that of the free cavity was measured:

$$\widetilde{\delta\nu}^{\mathrm{FP1}}_{\mathrm{err-stab}}(f) = \nu_0 \frac{v^{\mathrm{FP1}}_{\mathrm{err-stab}}(f)}{L_0} \left(\frac{\mathrm{d}v_{\mathrm{err}}^{\mathrm{FP}}}{\mathrm{d}L} \right)^{-1} \tag{9.8}$$

$$\widetilde{\delta\nu}^{\mathrm{FP2}}_{\mathrm{err-stab}}(f) = \nu_0 \frac{v^{\mathrm{FP2}}_{\mathrm{err-stab}}(f)}{L_0} \left(\frac{\mathrm{d}v_{\mathrm{err}}^{\mathrm{FP}}}{\mathrm{d}L} \right)^{-1} |1 + G_{\mathrm{FP}}(f)| \tag{9.9}$$

Figure 9.4 shows the typical power-spectrum of the above mentioned four signals. One can see that the expected ($\delta\nu^{\rm calc}_{\rm err-stab}$) and the measured ($\delta\nu^{\rm FP1}_{\rm err-stab}$) error signal for the stabilization loop agreed well with each other, which indicates that the servo loop worked quite correctly. It is apparent that the measured signals were dominated by the seismic-induced noise in the lower frequency range (see the previous section about the seismic-induced noise). For the free-running laser, the data in the frequency range higher than 100Hz was least-squares fitted by the power-law to give the model of the frequency noise below 100Hz:

$$\widetilde{\delta\nu}^{\rm model}_{\rm free}(f) = 2.21 \times 10^3 \times \left(\frac{1{\rm Hz}}{f}\right)^{0.825}. \tag{9.10}$$

There were also the shot-noise of the P-D-H sensing system for the two cavities, which will be calculated in the followings.

9.3.2 Shot Noise Level of the Pound-Drever-Hall Sensing System

Even though one took the effect of the seismic-induced noise into account, there still remained the difference between the measured error signal of the stabilization loop ($\delta\nu^{\rm FP1}_{\rm err-stab}$) and that of the loosely locked cavity ($\delta\nu^{\rm FP2}_{\rm err-stab}$) in the frequency range between 200 and 2kHz. In the loosely-locked cavity's spectrum, which is the measure of the "real" frequency stability, there was a noise floor originating from the shot noise of P-D-H sensing system. To confirm this, the shot noise level of the P-D-H system was measured as follows.

As mentioned earlier in Sec. 8.4, a small fraction of the reflected beams from the cavities were picked off and demodulated at 15 MHz to give the P-D-H error signal. The noise level of the demodulation system was the sum of the shot noise of the real photo-current and the electronics noise. The electronics noise of the demodulating system was expressed as the corresponding photo-current in the photo diode. The noise level of the demodulated signal was then represented by

$$\widetilde{v}_{{\rm demod}n} = \sqrt{2e\,(I + I_{{\rm D}n})}R_{{\rm equiv}n} \quad (n = 1, 2) \tag{9.11}$$

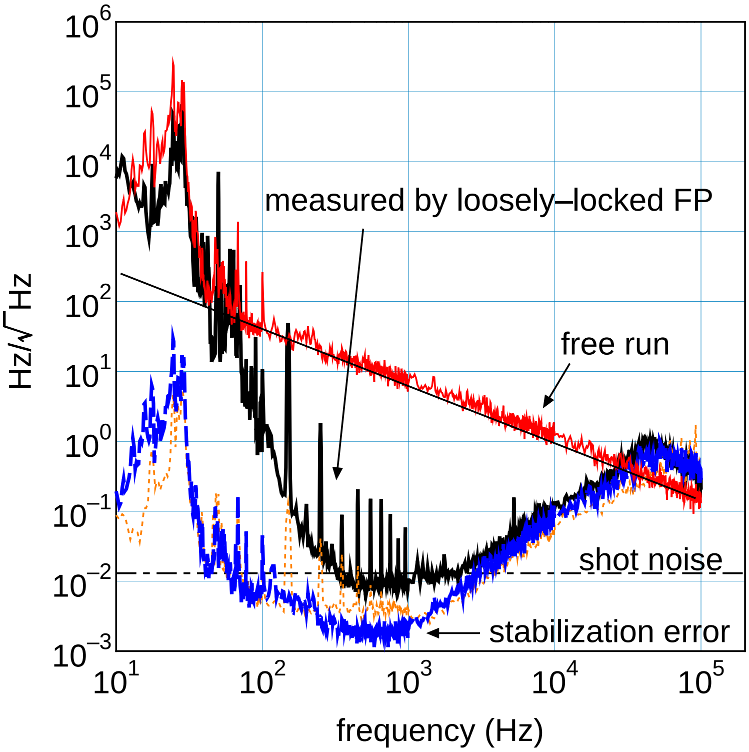

Figure 9.4: *The frequency noise of the laser with and without the frequency stabilization of the typical servo setting. The thin solid line is the noise level of the free-running laser. The fitted line for the free-running laser is also shown. The the thin dotted and the thick broken lines are the calculated and the measured error signal of the closed stabilization loop. The thick solid line shows the frequency noise level of the stabilized laser measured by using loosely-locked cavity as another reference. Below 100Hz, frequency noise was masked by the seismic-induced vibration of the mirrors. The dot-dashed line is the shot-noise level of the P-D-H systems for the two cavities.*

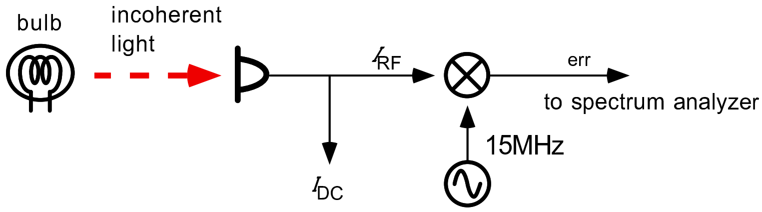

Figure 9.5: *Calibration of the shot-noise level, the dark current, and the equivalent gain of the RF P-D-H circuits. Incoherent light from the bulb was used as the standard of the shot-noise level. The DC photo-current in the photodiode and the spectrum of the demodulated signal were measured with several input power levels.*

where $v_{\mathrm{demod}n}$, I, $I_{\mathrm{D}n}$, and $R_{\mathrm{equiv}n}$ are the demodulated signal, the DC photo-current in the diode, the equivalent photo-current (the dark current) of the electronics, and the equivalent gain of the system with the dimension of the resistance,

The shot noise level corresponding to the demodulated signals are written by

$$\widetilde{\delta\nu}_{\mathrm{shot}n}(I_{\mathrm{DC}}) = \tilde{v}_{\mathrm{demod}n}\frac{\nu_0}{L_0}\left(\frac{\mathrm{d}v_{\mathrm{err}}^{\mathrm{FP}n}}{\mathrm{d}L}\right)^{-1} \quad (n = 1, 2). \tag{9.12}$$

The dark current and the equivalent gain of both of the P-D-H circuits were calibrated by using incoherent light from an electric bulb (Fig. 9.5). The DC current in the photodiode and the power-spectral density of the demodulated signal were measured with various input power. Since it is reasonable to assume that the intensity noise of the incoherent source from the bulb reached the shot-noise level at 15MHz, this measurement can be thought as a calibration of the shot-noise level. Figure 9.6 shows the measured data. The data were least-squares fitted to give the dark current and the equivalent gain of the circuits as

$$(I_{\mathrm{D1}}, R_{\mathrm{equiv1}}) = (91.5\mu\mathrm{A}, 16.1\mathrm{k}\Omega) \tag{9.13}$$

$$(I_{\mathrm{D2}}, R_{\mathrm{equiv2}}) = (169\mu\mathrm{A}, 22.4\mathrm{k}\Omega). \tag{9.14}$$

The data showed the saturation of the RF gain in $I_{\mathrm{DC}} > 2$ mA range, so the data in this range were not used for the fitting.

Combining these values with Eqs. 9.11 and 9.12 and the DC current in the photodiodes in the operation (0.48 mA for FP1 and 0.38 mA for FP2), the shot-noise level

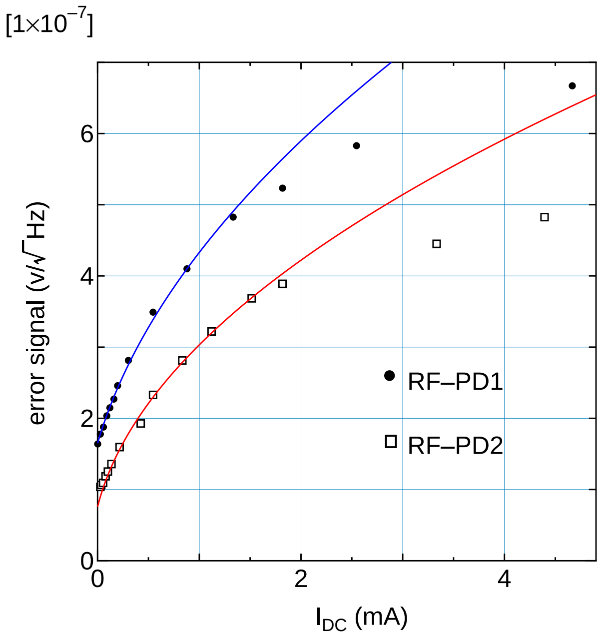

Figure 9.6: *Measured and fitted plot of the shot-noise level of the P-D-H circuits for both of the arms. The data showed the saturation of the RF gain in* $I_{\mathrm{DC}} > 2$ *mA range, so the data in this range were not used for the fitting.*

for the P-D-H circuits were obtained as

$$\widetilde{\delta\nu}_{\rm shot1} = 6.9{\rm mHz}/\sqrt{\rm Hz} \tag{9.15}$$

$$\widetilde{\delta\nu}_{\rm shot2} = 11{\rm mHz}/\sqrt{\rm Hz}. \tag{9.16}$$

The two shot-noise levels are uncorrelated, so the root of the square sum of these levels ($13{\rm mHz}/\sqrt{\rm Hz}$) should have appeared in the measured spectrum of the loosely locked cavity, though this is not the shot-noise level of the real frequency noise of the stabilized laser. From Fig. 9.4 one can see that the floor noise of the loosely locked cavity agreed with the shot-noise level.

9.3.3 Estimation of the Frequency Noise of the Stabilized Laser

It is a good assumption that the spectrum of the error signal of the loosely-locked cavity with the frequency stabilization agreed well with the real frequency noise of the laser at several kilohertz and above. At 100Hz and below, the seismic-induced noise masked the frequency noise. Also, in the frequency range between several hundred and several kilohertz, there was the shot-noise of the P-D-H sensing system of FP2 ($\delta\nu_{\rm shot2}$) which had nothing to do with the stabilization system. Though it was impossible to directly measure only the frequency noise separately from the displacement of the mirrors and the shot noise of the sensing system in the low frequency range, one could calculate the frequency noise of the stabilized laser:

$$\left|\widetilde{\delta\nu}_{\rm stab}(f)\right| = \sqrt{\left|\widetilde{\delta\nu}_{\rm shot1}\right|^2 + \left|\frac{\widetilde{\delta\nu}_{\rm n}(f)}{1+G_{\rm stab}}\right|^2} \tag{9.17}$$

where $\widetilde{\delta\nu}_{\rm n}(f)$ is the frequency noise of the free running laser. Therefore the following values are used as the frequency noise of the stabilized laser in this paper:

- The calculated spectrum by using the combination of Eq. 9.17 and the model spectrum of the free-running laser for $f < 100$Hz.

- The calculated spectrum by using the combination of Eq. 9.17 and the measured spectrum of the free-running laser between 100 and 5 kHz.

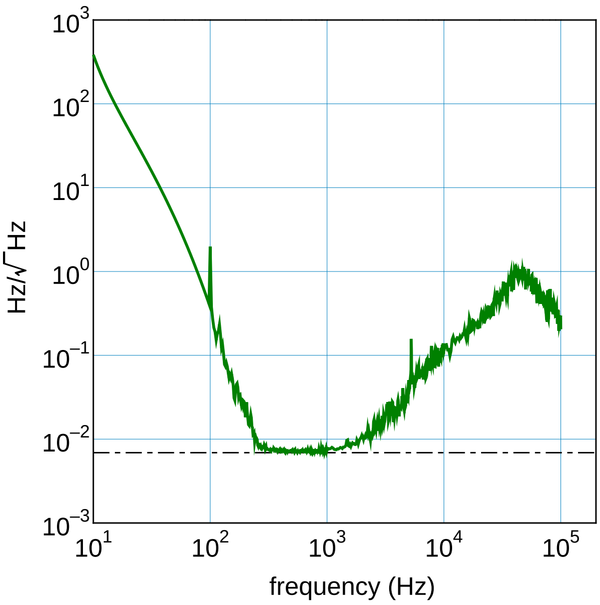

Figure 9.7: *Estimated frequency noise of the stabilized laser. In the frequency range lower than 100 Hz, the spectrum was obtained by using the model spectrum of the free-running laser and the stabilization gain. Between 100 and 5 kHz, it was calculated from the measured spectrum of the free-running laser, the shot-noise level, and the stabilization gain. At 5 kHz and above, the measured spectrum of the stabilized laser was used. The broken line shows the shot-noise level of the stabilizing system.*

- The measured error spectrum of the loosely-locked cavity corrected by the open-loop transfer function of the FP locking servo for 5 kHz and above.

Figure 9.7 shows the estimated frequency noise level of the stabilized laser.

9.3.4 Measurement of the Optical Common-Mode-Rejection

After the measurement of the frequency noise of the laser, the optical CMRR of the FPM interferometer was measured by intentionally applying the frequency noise to the laser. Figure 9.8 shows the setup of the measurement. The laser frequency stabilization was not used in this measurement, and both of the cavities were loosely locked to the resonance by means of mechanical feedback. The Michelson path was also locked, therefore the whole configuration was the FPM interferometer without the frequency

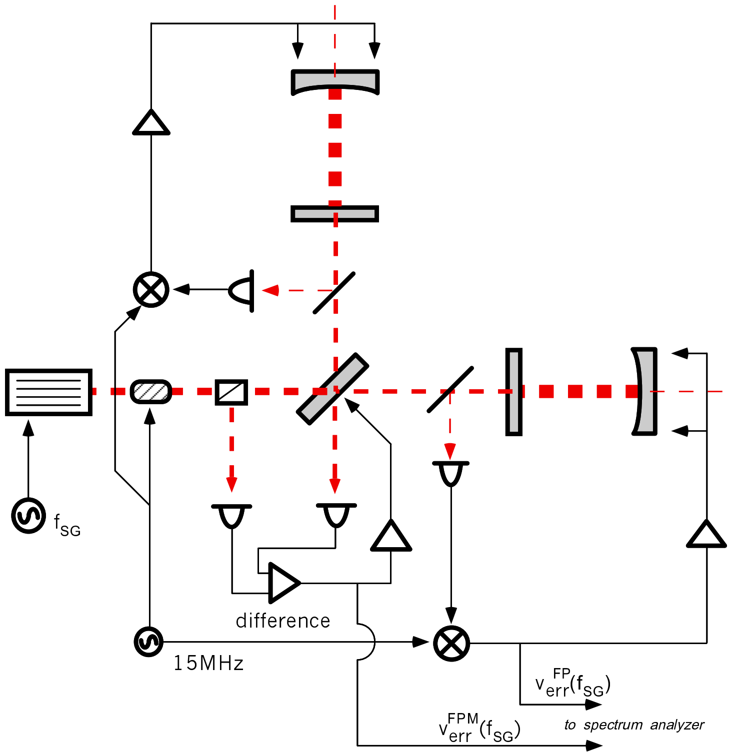

Figure 9.8: *Measurement of the CMRR of the FPM interferometer. A sinusoidal signal with the frequency $f_{\rm SG}$ was applied to the tuning PZT of the laser. Both of the cavities were locked loosely to the resonance without the frequency stabilization. The transfer function from the error of the FP locking to that of the FPM fringe locking was measured by using a spectrum analyzer.*

stabilization. A sinusoidal voltage was applied to the tuning PZT of the laser to generate the intentional frequency fluctuation. The transfer function from the error signal of one of the FPs to that of the FPM fringe locking was measured by using a spectrum analyzer. In this measurement, the error signals were approximated by

$$\tilde{v}_{\rm err}^{\rm FP1}(f) = L_0 \frac{\widetilde{\delta\nu}(f)}{\nu_0} \left(\frac{{\rm d}v_{\rm err}^{\rm FP1}}{{\rm d}L}\right) \frac{1}{1+G_{\rm FP1}} \tag{9.18}$$

$$\tilde{v}_{\rm err}^{\rm FPM}(f) = L_0 \frac{\widetilde{\delta\nu}(f)}{\nu_0} \left(\frac{{\rm d}v_{\rm err}^{\rm FPM}}{{\rm d}L_-}\right) \left(\frac{1}{1+G_{\rm FP1}} - \frac{1+\gamma_{\rm opt}(f)}{1+G_{\rm FP2}}\right) \frac{1}{1+G_{\rm FPM}} \tag{9.19}$$

thus the measured transfer function is represented by

$$H(f) \equiv \frac{\tilde{v}_{\rm err}^{\rm FPM}(f)}{\tilde{v}_{\rm err}^{\rm FP1}(f)}$$

$$= \left(\frac{\mathrm{d}v_{\mathrm{err}}^{\mathrm{FPM}}}{\mathrm{d}L_-}\right)\left(\frac{\mathrm{d}v_{\mathrm{err}}^{\mathrm{FP1}}}{\mathrm{d}L}\right)^{-1}\left\{1-\frac{1+G_{\mathrm{FP1}}}{1+G_{\mathrm{FP2}}}\left[1+\gamma_{\mathrm{opt}}(f)\right]\right\}\frac{1}{1+G_{\mathrm{FPM}}} \quad (9.20)$$

where H is the measured transfer function and γ_{opt} is the optical CMRR. One can see that the measured transfer function can be simply translated to the CMRR when all of the control gains G_{FPM}, G_{FP1}, and G_{FP2} are much smaller than unity (*i.e.* $f > 10\mathrm{kHz}$) as

$$|\gamma_{\mathrm{opt}}(f)| = |H(f)|\left(\frac{\mathrm{d}v_{\mathrm{err}}^{\mathrm{FPM}}}{\mathrm{d}L_-}\right)^{-1}\left(\frac{\mathrm{d}v_{\mathrm{err}}^{\mathrm{FP1}}}{\mathrm{d}L}\right), \quad (9.21)$$

The above equation is also true if the open-loop transfer function of the servo for the two cavities were identical. Figure 9.9 shows the measured optical CMRR of the interferometer. The optical CMRR had no significant frequency dependence, which agreed with the fact that the cut-off frequencies of the cavities were about 100 kHz. Though there seemed to be the frequency dependence in $f < 10$ kHz range, this was because of the difference between G_{FP1} and G_{FP2}. Even though it was theoretically possible to correct the measured transfer function to CMRR, it was very difficult to do the correction in fact, because the small CMRR value had to be calculated as the difference of the large numbers which was the same order of or much larger than CMRR itself in this frequency range. The value of CMRR was measured as

$$\gamma_{\mathrm{opt}} = 2 \sim 3 \times 10^{-3}. \quad (9.22)$$

The optical CMRR of 1 % level was almost always realizable without any difficulties. However, the best value on the order of 0.1 % was possible only when the mirrors of the interferometer were aligned very carefully[2]. Though the dependence of the CMRR on alignment was not measured quantitatively, we have observed the degradation of the CMRR when the mirrors were poorly aligned (Fig. 9.10). Also we have observed that the CMR was degraded after several hours of operation, which could be recovered by aligning the mirrors again.

The measurement of the optical parameters such as the finesse and the reflection coefficient of the cavities were not as accurate as 0.1 % level, therefore it was difficult

[2]The mirrors were aligned to maximize the contrast of the FPM interferometer.

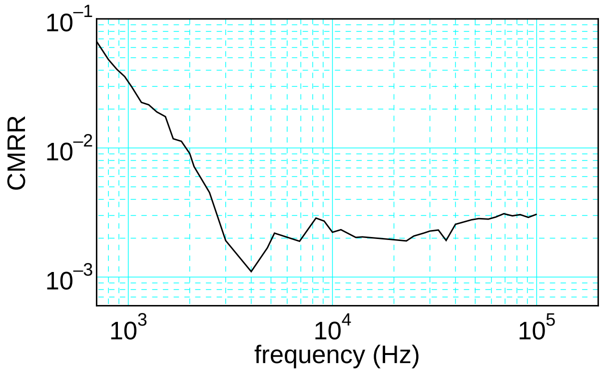

Figure 9.9: *The optical CMRR of the FPM interferometer was measured to be* $2 \sim 3 \times 10^{-3}$. *One can see that there was no significant frequency dependence in* $f > 10$ *kHz range. The frequency dependence in the lower frequency range came from the asymmetry of the cavity-locking servos when the measurement was done, and this had nothing to do with the optical CMRR.*

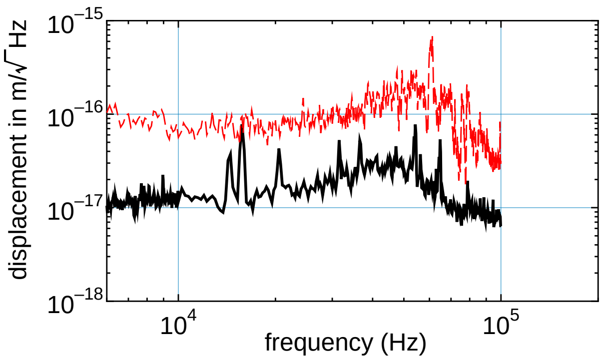

Figure 9.10: *The displacement sensitivity of the FPM interferometer. When the interferometer was aligned carefully (solid line), the CMRR of* 10^{-3} *order was obtained. With a small misalignment, the CMRR was degraded and thus the frequency-noise contribution in the spectrum increased (broken line).*

to conclude if the best value was limited by the asymmetries in the optics. However, it is quite reasonable to assume that the asymmetries in the optics were within 1 %, considering the fact that the CMRR of 1 % was relatively easy to realize. From Eqs. 7.6 and 7.15, there still remains the possibility that the asymmetries in the optics was compensated by the alignment. This possibility was not studied further, because the alignment sensors that directly measure the coupling of the cavities to the fields would have been required for such purpose.

9.3.5 Total CMRR and the Projection of the Frequency Noise on the Displacement Sensitivity

As shown in Eq. 8.22, not only the optical CMRR but the control asymmetry factor $\gamma_{\mathrm{f}}^{\mathrm{s}}$ also determined the interferometer's response to the frequency noise in this experiment. Therefore both of these two factors have to be taken into account to project the frequency noise of the laser onto the displacement sensitivity of the FPM interferometer:

$$\gamma(f) = \sqrt{|\gamma_{\mathrm{o}}|^2 + |\gamma_{\mathrm{f}}^{\mathrm{s}}(f)|^2} \tag{9.23}$$

where γ represents the total CMRR of the interferometer. By combining Eqs. 8.22 and 9.23, the frequency noise of the stabilized laser was projected on the displacement sensitivity of the FPM,

$$\widetilde{\delta L}_{-}^{\mathrm{FM}}(f) = \frac{\sqrt{|\gamma_{\mathrm{o}}|^2 + |\gamma_{\mathrm{f}}^{\mathrm{s}}(f)|^2}}{1 - \gamma_{\mathrm{m}}^{\mathrm{s}}(f)} L_0 \frac{\widetilde{\delta\nu}_{\mathrm{stab}}(f)}{\nu_0} . \tag{9.24}$$

In Fig. 9.11, both of the optical CMRR and the servo symmetry are projected on the displacement sensitivity. Due to the servo asymmetry, the frequency noise level was the dominant noise source between 400 and 1 kHz.

9.4 Shot Noise of the Michelson Fringe Detection System

The Michelson fringe detection system also had its own shot-noise level. The analysis of this was rather simple and straightforward compared with that of the P-D-H system,

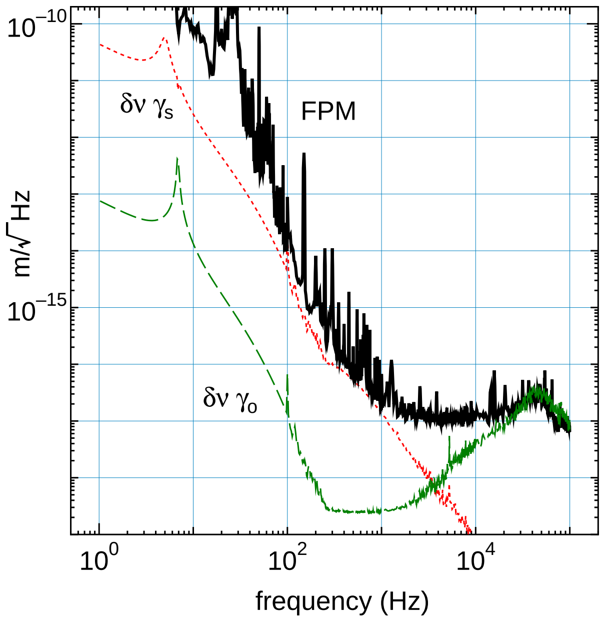

Figure 9.11: *The projection of the frequency noise of the stabilized laser on the displacement sensitivity of the FPM interferometer. The solid line shows the FPM sensitivity, the dashed line is the projection of the frequency noise that coupled to the optical CMRR, and the dotted line is the projection of the frequency noise coupled to the asymmetry factor of the servo system.*

because there was no RF circuits used in the system. During the operation of the interferometer, the DC voltage of the photo detectors were measured, from which the current in the photodiodes were calculated. The shot-noise voltage of the detectors are written by

$$v_{\rm shot}^{{\rm PD}n} = \sqrt{2e\frac{v_{{\rm DC}n}}{R}} \times R \quad (n = 1, 2) \tag{9.25}$$

where $v_{{\rm DC}n}$ is the DC voltage of the photo-detector for PDn ($n = 1, 2$) and R is the feedback resistance of the detector circuit (see Fig. B.7 for the circuit of the detectors). Though the shot-noise voltage itself should have flat spectrum, it had to be corrected by the cavity pole (100kHz) in the higher frequency range. Also, since the shot noise in the DC detectors were added to the system after the recombination of the beam, it had to be corrected by the servo asymmetry factor and the open-loop transfer function of the FP locking servo, but not by that of the Michelson fringe servo. Thus the shot-noise level of the displacement sensitivity was obtained from the following equation:

$$\widetilde{\delta L}_-^{\rm shot}(f) = \left(\frac{{\rm d}v_{\rm err}^{\rm FPM}}{{\rm d}L_-}\right)^{-1} \sqrt{|v_{\rm shot}^{\rm PD1}|^2 + |\alpha v_{\rm shot}^{\rm PD2}|^2} \left|\frac{[1 + G_{\rm FP}(f)]\,[1 + if/f_{\rm c}]}{1 - \gamma_{\rm m}^{\rm s}(f)}\right| \tag{9.26}$$

where α is the electronic gain factor (Eq. 6.31) and $f_{\rm c}$ is the cut-off frequency of the cavities. Putting the measured values into the above equation, the shot-noise level of the displacement sensitivity was calculated as

$$\widetilde{\delta L}_-^{\rm shot}(f) = 6.6 \times 10^{-18}\ {\rm m}/\sqrt{\rm Hz} \times \left|\frac{[1 + G_{\rm FP}(f)]\,[1 + if/f_{\rm c}]}{1 - \gamma_{\rm m}^{\rm s}(f)}\right|, \tag{9.27}$$

which is plotted in Figure 9.12.

9.5 Other Noise Sources

In this section, other two noise sources (*i.e.* the electronics noise and the intensity noise) and their levels which are plotted in Fig. 9.13 are described briefly.

9.5.1 Electronics Noise

Among the many electronics circuits, the largest noise source was the coil driver for the actuator of the FP loose-locking servo. The end mirror of the FP cavity was driven by

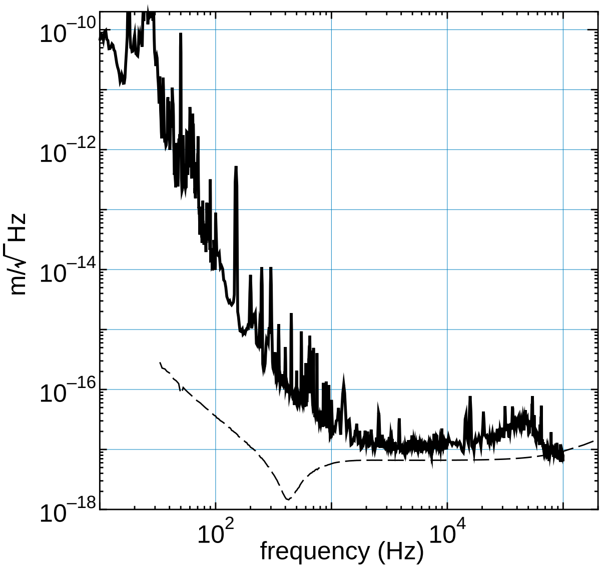

Figure 9.12: *Shot-noise level of the Michelson fringe detection system (broken line) and the displacement noise level of the FPM interferometer (solid). The floor level was* 6.6×10^{-18} m/$\sqrt{\text{Hz}}$*. The spectrum was corrected by the cavity pole (100 kHz) and the feedback servo of the FP locking.*

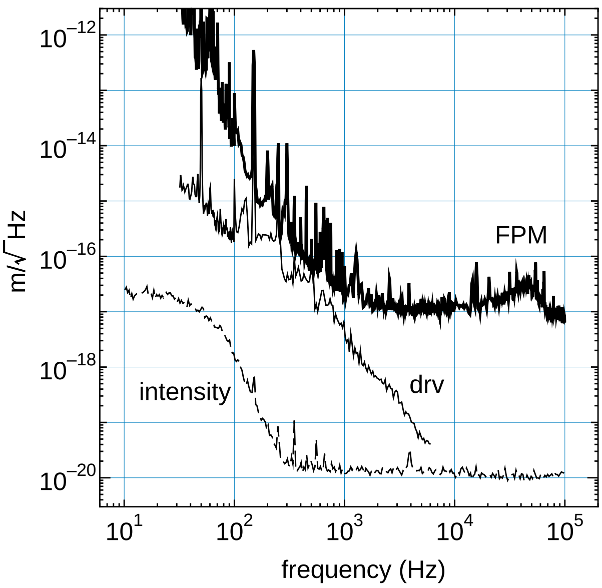

Figure 9.13: *The equivalent displacement noise level of the electronics noise (thin solid line) and the intensity noise of the input light (broken line). The thick solid line is the displacement noise level of the FPM interferometer.*

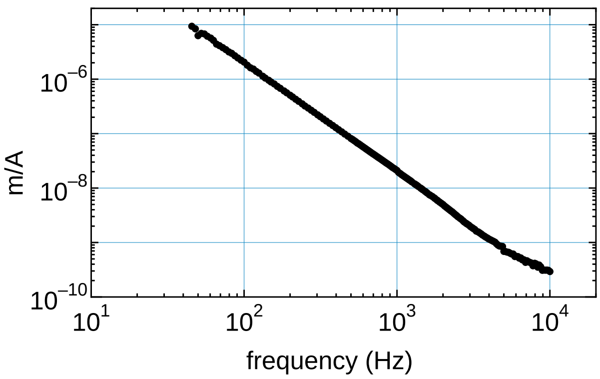

Figure 9.14: *Transfer function from the feedback current to the displacement of the mirror. This plot is the calculated value which was obtained from the open-loop transfer function of the FP locking servo, the transfer function of the control circuit from the error signal to the feedback signal, the impedance of the current read-out resistance, and the displacement-to-voltage conversion factor of the FP.*

the electronics noise in the feedback circuit, thus the phase fluctuation was generated in the reflected beam from the cavity. The input of the driver was grounded and the voltage noise of the feedback signal represented by $v_{\rm drv}$ was measured. During the measurement, the output of the driver was connected to the coil-and magnet just in the same way as in the operation of the interferometer[3]. On the other hand, the open-loop transfer function of the FP locking servo ($G_{\rm FP}$) and the transfer function from the error signal to the feedback voltage which is represented by $H_{\rm circ}$ were measured. The ratio of $G_{\rm FP}$ to $H_{\rm circ}$ was used as the transfer function from the feedback voltage to the error signal, which is shown in Fig. 9.14. The plot showed that the actuator's transfer function agreed well with the f^{-2} formula:

$$1.8 \times 10^{-2} \times \left(\frac{1\mathrm{Hz}}{f}\right)^2 \mathrm{m/A}. \tag{9.28}$$

The equivalent displacement noise by the electronics of the coil driver was then written by

$$\delta L_-^{\rm drv} = \frac{G_{\rm FP}}{H_{\rm circ}} v_{\rm drv} \left(\frac{\mathrm{d}v_{\rm err}^{\rm FP}}{\mathrm{d}L}\right)^{-1}. \tag{9.29}$$

[3]Otherwise the load-impedance to the driver would have changed the noise property.

As Fig. 9.13 shows, though the driver noise was not the dominant source, it was close to the noise level of the FPM interferometer between 100 and 1kHz.

9.5.2 Intensity Noise

In general, though the interferometer is tightly locked to its operation point by servo systems, there still remains some residual deviation in the phase-extraction point of the signal. The intensity noise of the laser couples to this residual deviation and is converted to the displacement signal:

$$\delta L_{-}^{\mathrm{I}} = \langle \delta L_{-} \rangle_{\mathrm{RMS}} \frac{\delta I}{I_0}, \tag{9.30}$$

where $\delta L_{-}^{\mathrm{I}}$, $\langle \delta L_{-} \rangle_{\mathrm{RMS}}$, and $\delta I / I_0$ are the equivalent displacement noise originating from the intensity noise, the RMS residual fluctuation, and the relative intensity noise of the laser, respectively. To evaluate this noise level, the intensity noise of the input light and the residual fluctuation of the Michelson fringe were measured (Fig. 9.15). Because the input optics were in the open air, the intensity noise of the input light was thought to be larger than the intensity noise of the laser itself. Especially, the spectrum was not stationary in the lower frequency range, which indicates that the noise came from the dust or the air flow. On the other hand, the residual fluctuation of the Michelson fringe was typically several millivolts, which corresponded to $10^{-13}\,\mathrm{m}$ of the displacement. Because of this small residual fluctuation, the intensity noise was not a problem at all in this experiment: Multiplying the intensity noise in Fig. 9.15 by $10{-}13\,\mathrm{m}$, the displacement noise level of $10^{-18}\,\mathrm{m}/\sqrt{\mathrm{Hz}}$ was obtained at 100 Hz.

9.6 Summary of the Noise Analysis

We have identified noise sources which limited the strain sensitivity in almost all of the frequency range of our interest. Figure 9.16 shows the measured displacement noise of the FPM interferometer, together with the noise level of the various sources. The displacement noise level of the interferometer reached $2 \times 10^{-17}\mathrm{m}/\sqrt{\mathrm{Hz}}$ at 1kHz and $1 \times 10^{-17}\mathrm{m}/\sqrt{\mathrm{Hz}}$ at the noise floor between 2kHz and 10kHz. The floor noise was identified as the shot noise of the light in the Michelson fringe detection system.

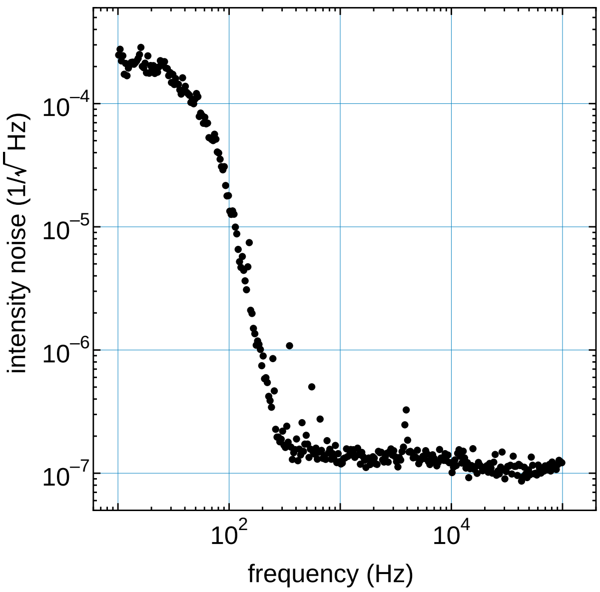

Figure 9.15: *Measured relative intensity noise of the input light to the interferometer. Since the input optics were placed in the open air, this plot is thought to be larger than the intensity noise of the laser itself. Especially, the spectrum was not stationary in the lower frequency range, which indicates that the noise came from the dust or the air flow.*

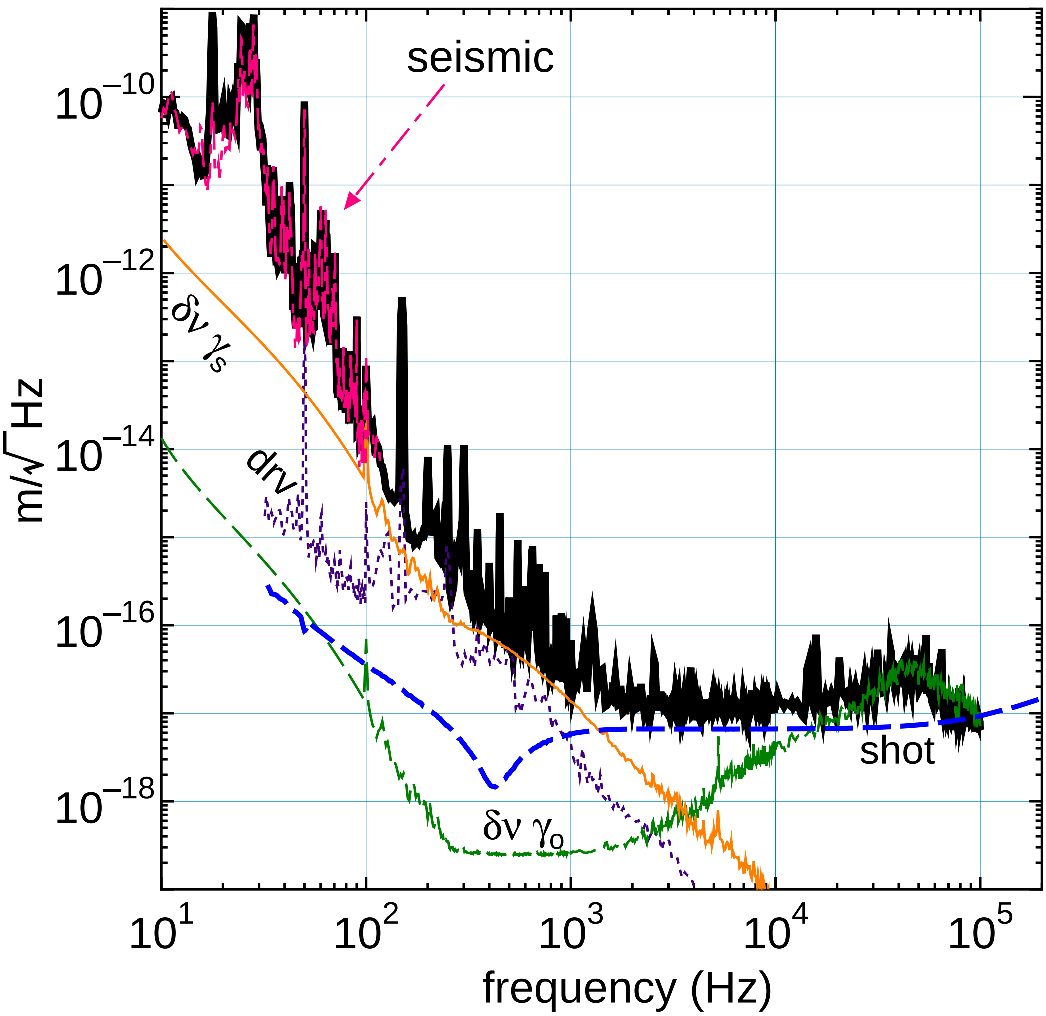

Figure 9.16: *Displacement noise level of the 3-m FPM interferometer, plotted together with the noise sources.* $\delta\nu\gamma_{\rm o}$*, the frequency noise coupled to the optical CMRR* ($2 \sim 3 \times 10^{-3}$)*;* $\delta\nu\gamma_{\rm s}$*, the frequency noise coupled to the servo asymmetry; drv, the electronic noise of the driver of the coil-magnet actuator used for the FP control; shot, the shot noise of the Michelson fringe detection; seismic, the seismic-induced vibration of the mirrors. The noise floor between 2kHz and 10kHz was dominated by the shot-noise level, which was* $6.6 \times 10^{-18}\mathrm{m}/\sqrt{\mathrm{Hz}}$.

Below 100Hz, the seismic noise was dominant. At 20kHz and above, the spectrum was dominated by the the frequency noise of the laser. The frequency stabilization and the good optical CMRR of $2 \sim 3 \times 10^{-3}$ suppressed the frequency noise level smaller than the shot-noise limited sensitivity of the Michelson fringe detection in the kilohertz range. The servo asymmetry factor degraded the CMRR below 1 kHz, thus the frequency noise was also the dominant noise source between 400 and 1 kHz. This was because of the asymmetric design of the servo system used in this experiment. Though the noise of the driver circuit of the actuators was the dominant source, it was close to the noise level of the FPM interferometer between 100 Hz and 1 kHz.

Though the dependence of CMRR on the alignment was not measured quantitatively, the dependence itself was observed during the operation of the interferometer.

10. Discussions

10.1 Asymmetry of the Optics

In this experiment, the CMRR on the order of 10^{-3} was obtained. It was difficult to conclude if this was limited by the asymmetries in the optics, because the measurement of the optical parameters such as the finesse and the reflection coefficients of the cavities were not as accurate as 0.1 % level. However, from the measured finesse (Eq. 8.8), it is quite reasonable to assume that the asymmetries in the optics were about or within 1 %. The CMRR of 1 % was relatively easy to realize, which also supports this assumption. The finesse of each of the cavity was about 230, which should be on the same order as, or smaller than, the finesse of the cavities used in the full-scale interferometers. Also the optics for the full-scale detectors will have higher optical quality than those used in this experiment. Thus it seems that one can expect to have the optical CMRR around 1 % in full-scale interferometer. On the other hand, further experimental study for the large optics for the full-scale detectors has to be made, since the results were obtained only in the small optics with the beam size only less than 1 mm; any non-uniformity in the mirror coating for large area would change the result in a large detector.

10.2 Geometrical Asymmetry

For the geometrical asymmetries due to the misalignment of the mirrors to the laser beam, we could not make the quantitative measurement. However, on the assumption that the modal analysis presented in this paper is correct, the requirement for the alignment of the mirrors which would be put by the degradation of CMRR will not be as severe as the one put by the power-recycling requirements.

For example, if we require that the CMRR limited by the geometrical asymmetries should be 10^{-2}, the same order as the optical CMRR, the requirements for the misalignment parameters are:

$$\left(\frac{a_x}{w_0}\right)^2 < 10^{-2} \tag{10.1}$$

$$\left(\frac{\alpha_x}{\alpha_0}\right)^2 < 10^{-2}, \tag{10.2}$$

where w_0, α_0, a_x, and α_x are the waist size of the cavity, the divergence angle, and the misalignment parameters corresponding to the lateral displacement and the angular rotation of the modes. For example, in the TAMA300 interferometer, the beam parameters are w_0 =8.5 mm and α_0=40 μm. From Eqs. 10.1 and 10.2, the allowable misalignment angle of each of the mirrors is on the order of several μrad. This requirement is not as severe as the one coming from the power-recycling factor requirements [40, 47], thus an interferometer with the automatic alignment control system will realize this requirement.

However, the analyses presented here are the simplest ones. A more detailed analyses are required to discuss the geometrical asymmetries such as the mismatching and the roughness of the surface of the mirrors.

10.3 Servo Asymmetry

In the full-scale detectors, any asymmetries in the servo system have to be carefully avoided, because such asymmetries will potentially degrade the CMRR even though the interferometer is optically symmetric. The servo asymmetry factor is proportional to the difference of the control gains for the two arms; for example, Equation 8.24 is the representation specific to this experiment. Even though the optics and the servo design of the interferometer are symmetric, some asymmetry may exist in the physical implementation of the servo system, *i.e.* the imbalance in the actuators of the mirrors. Let us see the simplest case (Fig.10.1). To simplify the problem, only the two degrees of freedom, *i.e.* δL_- and δL_+ are considered here. As the noise source, only the frequency noise is taken into account. Suppose that the signal extraction is completely

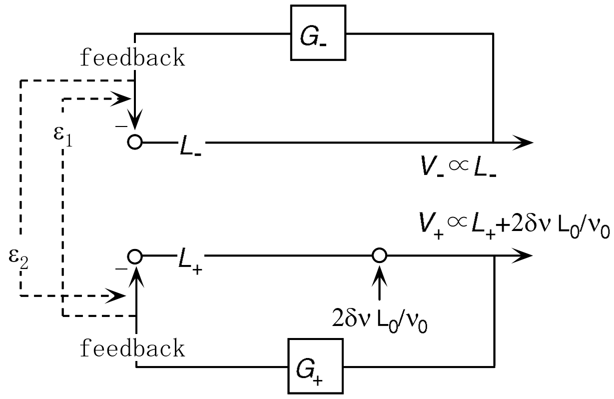

Figure 10.1: *The simplest system with the servo asymmetry.*

symmetric. In such system, the error signals are written by:

$$V_- \propto \delta L_- \tag{10.3}$$

$$V_+ \propto \delta L_+ + 2\delta\nu\frac{L_0}{\nu_0} \tag{10.4}$$

where $\delta L_\pm$ represents the differential and common variation of the cavity lengths. There are control asymmetries, so the feedback signals have the contamination terms:

$$G_-\delta L_- + \epsilon_1 G_+ \left(\delta L_+ + 2\delta\nu L_0/\nu_0\right) \tag{10.5}$$

$$G_+ \left(\delta L_+ + 2\delta\nu L_0/\nu_0\right) + \epsilon_2 G_- \delta L_-, \tag{10.6}$$

where $G_\pm$ are the mechanical control gain for the common and the differential displacement and $\epsilon_n\,(n = 1, 2)$ represent the imbalances in the servo system. Assuming that the imbalances are much smaller than unity, the above equations are solved as

$$V_- \propto -\epsilon_1\delta\nu\frac{L_0}{\nu_0}\frac{G_+}{(1+G_+)(1+G_-)} \tag{10.7}$$

to the first order of ϵ_n. One can see that the imbalance in the servo actuator directly couples to the frequency noise to contaminate the signal of the differential displacement. It would be possible to match the coupling of the actuators in 1 % accuracy, thus the CMRR of 10^{-2} is a reasonable assumption for the servo asymmetry [48] if the control system is well-designed. Moreover, it is apparent that the servo asymmetry is minimized by minimizing the control gain for the common-mode motion: The common mode motion should be compensated by the frequency of the laser as long as it is possible [1].

10.4 Frequency Noise and CMRR

As shown in the preceding discussions, one can expect to have a total CMRR on the order of or less than 1 % even in a full-scale detector. This will relax the requirement for the frequency noise of the laser used in the detector. For example, in the TAMA300 detector, the noise level of the interferometer must be less than 3×10^{-21} in strain with a 300 Hz bandwidth, which corresponds to $5 \times 10^{-20}\,\mathrm{m}/\sqrt{\mathrm{Hz}}$ displacement sensitivity. Considering the length of the cavity (300 m) and the frequency of Nd:YAG laser (about 300 THz), the requirement for the frequency noise of the laser used in the TAMA detector is

$$\delta\nu_{\mathrm{stab}} < 5 \times 10^{-6}\,\mathrm{Hz}/\sqrt{\mathrm{Hz}}\,, \tag{10.8}$$

if the CMRR is 1 %. This requirement is thought to be feasible.

10.5 Electronics

In this experiment the noise of the driver circuit for the actuators was close to the FPM noise level between 100 and 1 kHz. A more careful design of the actuator system, *i.e.* the optimal coupling and the minimum noise current, are needed for the actuator of the full-scale detectors.

In the experiment, the measured noise level of the driver was roughly -140 $\mathrm{dBv}/\sqrt{\mathrm{Hz}}$, which corresponded to the order of $100\,\mathrm{pA}/\sqrt{\mathrm{Hz}}$. From the technological point of view, the smallest noise possible would be the order of $10\,\mathrm{pA}/\sqrt{\mathrm{Hz}}$ which is limited by the thermal noise of the resistors. Also, the coupling of the actuator represented by Eq. 9.28 was larger than required. From the resonant frequencies of the suspension (1.2 and 1.5 Hz) and the maximum current which the driver was able to supply (about

[1] This is the basis of the design of the common-mode control of the TAMA300 interferometer. The mechanical gain of the common-mode control should be minimized to avoid the potential contamination of the common mode signal to the gravitational wave signal due to the mechanical imbalances.

$40\,\mathrm{mA}_{\mathrm{p-p}}$), Eq. 9.28 indicates that the actuator could make the testmass move as large as $600\,\mu\mathrm{m}_{\mathrm{p-p}}$. Since the motion of the mirrors which had to be compensated were several tens microns at their maximum, it is apparent that the coupling of the actuator was at least 10 times larger than required, which made the effect of the current noise larger. In the large-scale interferometers, the coupling of the actuators for the mechanical control has to be optimized so that the amplitude of the motions of the mirrors can just be compensated by the actuators. Only the electronics with the minimum current noise and the minimum coupling will satisfy the crucial requirement for the noise and the dynamic range of the actuator for the full-scale interferometers [49][2].

[2] After this study has been finished, actuator system for the TAMA300 interferometer was carefully designed. The noise level of the actuator was measured to be 30 $\mathrm{pA}/\sqrt{\mathrm{Hz}}$ for each coil, with the dynamic range of 50 $\mu\mathrm{m}_{\mathrm{p-p}}$ for the differential displacement. The displacement noise level is still about factor three larger than the full sensitivity of the TAMA interferometer (5×10^{-20} $\mathrm{m}/\sqrt{\mathrm{Hz}}$), therefore the compensation of the displacement by other means in the low frequency range is being studied.

11. Summary and Conclusion

We have developed a 3-m Fabry-Perot-Michelson interferometer in the campus of The University of Tokyo to experimentally investigate the optical recombination.

Optical recombination of the reflected beams from the two cavities on the beamsplitter was successfully demonstrated. The optical CMRR of $2 \sim 3 \times 10^{-3}$ was observed, which showed that it is possible to optically reduce the effect of the common-mode noise even in the all-suspended interferometer. This was the first example of the optically recombined, all-suspended interferometer with the Fabry-Perot cavities in the arms[16].

As the result of the detailed analysis of the interferometer, noise sources which limited the strain sensitivity were identified in almost all of the frequency range of our interest. The displacement noise level of the interferometer reached $2 \times 10^{-17}\mathrm{m}/\sqrt{\mathrm{Hz}}$ at 1kHz and $1 \times 10^{-17}\mathrm{m}/\sqrt{\mathrm{Hz}}$ at the noise floor between 2kHz and 10kHz, which was limited by the shot noise of the light in the Michelson fringe detection system. The frequency stabilization and the good optical CMRR of $2 \sim 3 \times 10^{-3}$ suppressed the frequency noise level smaller than the shot-noise limited sensitivity of the Michelson fringe detection in the kilohertz range.

We have observed that the servo asymmetry degraded the optical CMRR between 400 and 1 kHz. However, an appropriate design of the servo system would make the servo asymmetry smaller than the optical one.

Though the dependence of CMRR on the alignment was not measured quantitatively, the dependence itself was observed during the operation of the interferometer. The requirements for the alignment of the mirrors put by geometrical asymmetry effect is not as severe as the ones put by other effects, so this will not a problem.

The results obtained in this paper became the bases of many of the research and development work on all-suspended FPM interferometer in Japan. Also, the analyses and the considerations for the servo system, modal approach, and the electronics were fed back to and are being applied to the design and fabrication works for the TAMA300 interferometer.

A. Modal Expansion of the Misaligned Beam

The detailed calculations about the modal expansion of the misaligned beam are shown here. For clarity, some of the equations which are presented in Chap. 5 appear again in this chapter.

A.1 Lateral Displacement

The two coordinate systems, (x, y, z) and (x', y', z'), are related to each other by a small parallel displacement a_x:

$$(x', y', z') = (x - a_x, y, z). \tag{A.1}$$

A set of Hermite-Gaussian fields in (x, y, z) coordinate system are defined by Eqs. 5.2 and 5.3. Let us consider an Hermite-Gaussian beam on the z' axis, which is represented by $\{U'_{lm+}\}$ (Fig. 5.5). We can expand the beam U'_{lm} by the set $\{U_{lm}\}$ to the second order of the displacement as

$$\begin{aligned}
U_{lm+}(x', y', z') &= U_{lm+}(x - a_x, y, z) \\
&\simeq U_{lm+}(x, y, z) - \frac{d}{dx}U_{lm+}(x, y, z)a_x + \frac{1}{2}\frac{d^2}{dx^2}U_{lm+}(x, y, z)a_x^2 \\
&\equiv \sum_{pq} < pq + |lm+' > U_{pq+} \\
&\simeq \iint \left[U_{lm+} + \frac{d}{dx}U_{lm+}a_x + \frac{1}{2}\frac{d^2}{dx^2}U_{lm+}a_x^2\right] U^*_{pq+} dxdy
\end{aligned} \tag{A.2}$$

After carrying out the above expansion, we obtain the expression for the laterally misaligned fundamental mode as

$$P_x(a_x) * U_{00+}(x, y, z) \equiv U_{00+}(x - a_x, y, z)$$

$$
\begin{aligned}
&= U_{00+}(x,y,z)\left[1 - e^{i\eta(z)}\left(-2\frac{x}{w(z)}\frac{a_x}{w_0} + \frac{w_0}{w(z)}\left(\frac{a_x}{w_0}\right)^2\right)\right. \\
&\quad \left. +2e^{2i\eta(z)}\left(\frac{x}{w(z)}\frac{a_x}{w_0}\right)^2 + O\left(a_x^3/w_0^3\right)\right] \\
&= \left[1 - \frac{1}{2}\left(\frac{a_x}{w_0}\right)^2\right]U_{00+} + \frac{a_x}{w_0}U_{10+} + \frac{1}{\sqrt{2}}\left(\frac{a_x}{w_0}\right)^2 U_{20+} \\
&\quad +O\left(a_x^3/w_0^3\right) \qquad \text{(A.3)}
\end{aligned}
$$

where P_x denotes the parallel transport operator. In the same way the expression for the first off-axis mode is obtained as

$$
\begin{aligned}
P_x(a_x) * U_{10+}(x,y,z) &\equiv U_{10+}(x-a_x,y,z) \\
&= \left[1 - \frac{3}{2}\left(\frac{a_x}{w_0}\right)^2\right]U_{10+} - \frac{a_x}{w_0}U_{00+} + \sqrt{2}\frac{a_x}{w_0}U_{20+} \\
&\quad +\sqrt{\frac{3}{2}}\left(\frac{a_x}{w_0}\right)^2 U'_{30+} + O\left(a_x^3/w_0^3\right). \qquad \text{(A.4)}
\end{aligned}
$$

A.2 Angular Tilt

The two coordinate systems are related to each other as

$$
\begin{pmatrix} x' \\ z' \end{pmatrix} = \begin{pmatrix} \cos\alpha_x & -\sin\alpha_x \\ \sin\alpha_x & \cos\alpha_x \end{pmatrix}\begin{pmatrix} x \\ z \end{pmatrix} \qquad \text{(A.5)}
$$

$$
y' = y. \qquad \text{(A.6)}
$$

In the same way as the parallel displacement, we can expand the beam by the Hermite-Gaussian modes of the tilted coordinates to the second order of the perturbation. For the fundamental mode, we obtain

$$
\begin{aligned}
R_x(\alpha_x) * U_{00+}(x,y,z) &\equiv U_{00+}(x\cos\alpha_x - z\sin\alpha_x, y, z\cos\alpha_x + x\sin\alpha_x) \\
&= \left\{1 - \frac{\alpha_x^2}{2}\left[\frac{1}{\alpha_0^2} - \frac{1}{2} - \frac{\alpha_0^2}{8}\left(1 + i\frac{z}{z_0}\right)\left(1 + 3i\frac{z}{z_0}\right)\right]\right\}U_{00+} \\
&\quad -i\alpha_x\left[\left(\frac{1}{\alpha_0} + \frac{i\alpha_0}{2}\frac{z}{z_0}\right)U_{10+} + \frac{\sqrt{2}}{8}\alpha_0\left(1 - i\frac{z}{z_0}\right)\left(\sqrt{3}U_{30+} + U_{12+}\right)\right] \\
&\quad +O\left(\alpha_x^2/\alpha_0^2\right) \times (l + m \geq 2 \ \text{off–axis terms}), \qquad \text{(A.7)}
\end{aligned}
$$

where R_x is the rotation operator and α_0 is the far-field divergence angle of the beam. For the first off-axis mode, we obtain

$$\begin{aligned}
R_x(\alpha_x) * U_{10+}(x,y,z) \quad &\equiv \quad U_{10+}(x\cos\alpha_x - z\sin\alpha_x, y, z\cos\alpha_x + x\sin\alpha_x) \\
&= \quad \left\{1 - \alpha_x^2\left[\frac{3}{2\alpha_0^2} - 1 - i\frac{3}{4}\frac{z}{z_0}\alpha_0^2 e^{2i\eta(z)}\left(1 - i\frac{3}{2}\frac{z}{z_0}\right)\right]\right\} U_{10+} \\
&\quad -i\alpha_x\left\{\left[\frac{1}{\alpha_0} - \frac{\alpha_0}{2}\left(1 + i\frac{z}{z_0}\right)\right] U_{00+}\right. \\
&\quad + \left[\frac{\sqrt{2}}{\alpha_0} - \frac{\alpha_0\sqrt{2}}{8}\left(1 - 7i\frac{z}{z_0}\right)\right] U_{20+} + \frac{\sqrt{2}\alpha_0}{8}\left(1 + i\frac{z}{z_0}\right) U_{02+} \\
&\quad \left. + \frac{\alpha_0}{4}\left(1 - i\frac{z}{z_0}\right) U_{22+} + \frac{\sqrt{6}\alpha_0}{4}\left(1 - i\frac{z}{z_0}\right) U_{40+}\right\} \\
&\quad + O\left(\alpha_x^2/\alpha_0^2\right) \times (l + m \geq 2 \ \text{off--axis terms}). \qquad \text{(A.8)}
\end{aligned}$$

(For the exact expansion coefficients of the second order perturbation, see Ref. 40.) Equations A.3, A.4, A.7, and A.8 are simplified under some approximations which we will discuss later.

A.2.1 Simplification of the Expressions

To simplify the expressions for the misaligned beam, we will make some assumptions. Under these assumptions, it is possible to neglect the second or higher-order off-axis modes.

Small-Divergence-Angle Approximation

In the most of the laser beams and the resonators, the divergence angle is very small [1]. Therefore α_x^2/α_0^2 terms are the leading terms of the second order perturbation in Eqs. A.7 and A.8. We can neglect other terms such as $\alpha_x^2\alpha_0^2$ and α_x^2.

The divergence angle is so small that we can neglect some of the first order perturbation terms. When the following condition is satisfied,

$$\left(\frac{\alpha_x}{\alpha_0}\right)^2 >> \alpha_x, \alpha_x\alpha_0, \qquad \text{(A.9)}$$

[1]For example, the divergence angle of the arm cavity of the 3-m FPM interferometer we have developed is about 4×10^{-4}rad. In TAMA-300 interferometer, α_0 is equal to 4×10^{-5}rad.

we can neglect such terms as $\alpha_x \alpha_0$ and α_x. Thus we obtain the equations

$$\begin{aligned} R_x(\alpha_x) * U_{00+}(x,y,z) &\simeq \left[1 - \frac{1}{2}\left(\frac{\alpha_x}{\alpha_0}\right)^2\right] U_{00+} - i\frac{\alpha_x}{\alpha_0} U_{10+} \\ &\quad + O\left(\alpha_x^2/\alpha_0^2\right) \times (l+m \geq 2 \text{ off–axis terms}), \quad \text{(A.10)} \\ R_x(\alpha_x) * U_{10+}(x,y,z) &\simeq \left[1 - \frac{3}{2}\left(\frac{\alpha_x}{\alpha_0}\right)^2\right] U_{10+} - i\frac{\alpha_x}{\alpha_0}\left[U_{00+} + \sqrt{2} U_{20+}\right] \\ &\quad + O\left(\alpha_x^2/\alpha_0^2\right) \times (l+m \geq 3 \text{ off–axis terms}), \quad \text{(A.11)} \end{aligned}$$

for the angular tilt.

We have to clarify the extent of the condition expressed in Eq. A.9. It is deformed into the following form:

$$\left(\frac{\alpha_x}{\alpha_0}\right)^2 >> \alpha_0^2. \quad \text{(A.12)}$$

As an example, we use the beam parameters of TAMA-300 interferometer. Since the waist radius of the arm cavity of TAMA-300 interferometer is 4×10^{-5}, the right side of the above inequality is 1.6×10^{-9}. We have seen (Eqs. A.7 and A.8) that $(\alpha_x/\alpha_0)^2$ is the order of the power which is transferred from one mode to others. Thus, Eq. A.9 says that the power which is "lost" from one mode by the misalignment is much larger than 1.6ppb. The loss of 1.6ppb can be neglected compared with the loss of the optics (absorption and the diffraction), therefore practically we can always assume that Eq. A.9 is satisfied.

Assumption About the Input Beam

We assume that the input beam which illuminates the interferometer is the fundamental Gaussian beam. From Eqs. A.3 and A.10, one can see that the misaligned fundamental mode has the first order coupling to the first off-axis mode and the second order couplings to the second or higher off-axis modes. Therefore the field in the interferometer has a 0-th order coupling to the fundamental mode, the first order to the first off-axis mode, and the second order to the second or higher off-axis modes:

$$E = O(1)U_{00} + O(a/w_0, \alpha/\alpha_0)U_{l+m=1} + O(a^2/w_0^2, \alpha^2/\alpha_x^2)U_{l+m\geq 2}. \quad \text{(A.13)}$$

The optical power of the field in the interferometer is second order for the first off-axis mode and the fourth order for the second or higher modes. Thus, for the optical power calculation, we can neglect the second and higher order modes. To the second order perturbation, all of the optical power is carried by the fundamental and the first off-axis mode.

To summarize, for the optical power calculation, as far as the input beam is the fundamental mode and the conditions $1 >> \frac{a_x}{w_0}$ and $1 >> \frac{\alpha_x}{\alpha_0} >> \alpha_0$ are satisfied, we can simplify Eqs. A.3, A.4, A.10, and A.11 to the following form:

$$
\begin{aligned}
P_x(a_x) * U_{00+}(x,y,z) &\simeq \left[1 - \frac{1}{2}\left(\frac{a_x}{w_0}\right)^2\right] U_{00+} + \frac{a_x}{w_0} U_{10+} && \text{(A.14)} \\
P_x(a_x) * U_{10+}(x,y,z) &\simeq \left[1 - \frac{3}{2}\left(\frac{a_x}{w_0}\right)^2\right] U_{10+} - \frac{a_x}{w_0} U_{00+} && \text{(A.15)} \\
R_x(\alpha_x) * U_{00+}(x,y,z) &\simeq \left[1 - \frac{1}{2}\left(\frac{\alpha_x}{\alpha_0}\right)^2\right] U_{00+} - i\frac{\alpha_x}{\alpha_0} U_{10+} && \text{(A.16)} \\
R_x(\alpha_x) * U_{10+}(x,y,z) &\simeq \left[1 - \frac{3}{2}\left(\frac{\alpha_x}{\alpha_0}\right)^2\right] U_{10+} - i\frac{\alpha_x}{\alpha_0} U_{00+} && \text{(A.17)}
\end{aligned}
$$

We can neglect the higher order modes than U_{10}.

A.3 Misalignments and the Mode Structure

Generally, the mode structure of the laser beam is not conserved when the beam propagates through the optical components. For example, when the optical components are misaligned, the off-axis modes appear in the optical system. The mode transformation is described by the ABCD matrix (Refs. 22, Ref. 32, etc.). In this section, the relation between the ABCD matrix formulation and the modal expansion will be shown.

A paraxial Hermite-Gaussian field is completely characterized by the waist radius w, the waist position (x, z), the angle between the the z axis and the optical axis α, and the order number n in the xz coordinate system. An Hermite-Gaussian field is transformed to another beam with another set of parameters by a system described by an ABCD matrix (Fig. A.1). The parameters are transformed from $(w_0, x = a_{x0}, z = d_0, \alpha_x = \alpha_{x0})$ to $(w_1, a_{x1}, d_1, \alpha_{x1})$. The order of the mode is not changed. It is well known (Refs. 22, Ref. 32, etc.) that the relations between the two set of parameters are written as

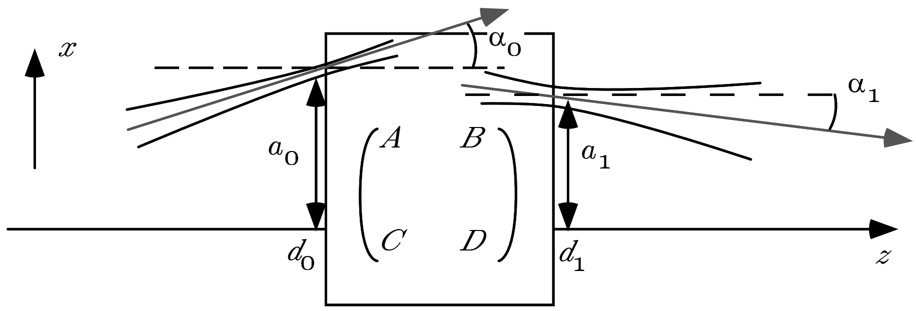

Figure A.1: *Beam transformation by a system described by a ABCD matrix*

follows:

$$\begin{pmatrix} a_{x1} \\ \alpha_{x1} \end{pmatrix} = \begin{pmatrix} A & B \\ C & D \end{pmatrix} \begin{pmatrix} a_{x0} \\ \alpha_{x0} \end{pmatrix} \tag{A.18}$$

$$i\frac{Kw_1^2}{2} = \frac{iAKw_0^2/2 + B}{iCKw_0^2/2 + D} \tag{A.19}$$

We can see the description of this system from another point of view. For convenience, we define here the two modes with the parameters $(w_0, x = 0, z = d_0, \alpha_x = 0)$ and $(w_1, x = 0, z = d_1, \alpha_x = 0)$ (no deviation from the z axis) as $U_{lm}(x, y, z)$ and $u_{lm}(x, y, z)$, respectively. Equations 5.31$\sim$ 5.36 indicates that the input field and the output field are the linear combinations of the fields $\{U_{lm}\}$ and $\{u_{lm}\}$. For the fundamental mode, we obtain

$$E_{\text{in}} = \left[1 - \frac{1}{2}\left(\frac{a_{x0}}{w_0}\right)^2 - \frac{1}{2}\left(\frac{\alpha_{x0}}{\alpha_0}\right)^2\right] U_{00+} + \left(\frac{a_{x0}}{w_0} - i\frac{\alpha_{x0}}{\alpha_0}\right) U_{10+} \tag{A.20}$$

$$E_{\text{out}} = \left[1 - \frac{1}{2}\left(\frac{a_{x1}}{w_1}\right)^2 - \frac{1}{2}\left(\frac{\alpha_{x1}}{\alpha_1}\right)^2\right] u_{00+} + \left(\frac{a_{x1}}{w_1} - i\frac{\alpha_{x0}}{\alpha_1}\right) u_{10+} \tag{A.21}$$

where α_0 and α_1 are the divergence angle of the input and output beam, respectively. The cross term which is proportional to $ia_{xn}\alpha_{xn} (n = 0, 1)$ was neglected. We can say that U_{00+} and U_{10+} are transformed into u_{00+} and u_{10+} respectively, because the order-number is not changed by the ABCD system.

When the following equation is satisfied,

$$\det \begin{pmatrix} A & B \\ C & D \end{pmatrix} = 1 \tag{A.22}$$

it is shown by using Eqs. A.18 and A.19 that the ratio of the power of the fundamental and first off-axis mode is conserved before and after the matrix:

$$\left(\frac{a_{x0}}{w_0}\right)^2 + \left(\frac{\alpha_{x0}}{\alpha_0}\right)^2 = \left(\frac{a_{x1}}{w_1}\right)^2 + \left(\frac{\alpha_{x1}}{\alpha_1}\right)^2 . \tag{A.23}$$

For the system which comprises the thin lenses, thin mirrors and the free space propagators, it is easily shown that the determinant of the ABCD matrix is equal to the unity.

The Gouy-phase shift is related to the transformation of the factor of the off-axis modes. When the difference of the phase between the fundamental and first off-axis mode due to the Gouy-phase shift is η_0 in the ABCD system, the amplitude of the first off-axis modes are related to each other as

$$\left(\frac{a_{x1}}{w_1}\right) - i\left(\frac{\alpha_{x1}}{\alpha_1}\right) = e^{i\eta_0}\left[\left(\frac{a_{x0}}{w_0}\right) - i\left(\frac{\alpha_{x0}}{\alpha_0}\right)\right] . \tag{A.24}$$

It is difficult to show that this relation is true in the arbitrary ABCD system in which the determinant of the matrix is equal to unity, because the ABCD matrix is a kind of black box and it has no information about the phase. However, again for the system with the thin lenses, thin mirrors and the free-space propagators, the above relation is always valid.

For the propagation of the first off-axis mode, we obtain the same result as the fundamental mode.

B. Circuits

The circuits used in the experiment are shown.

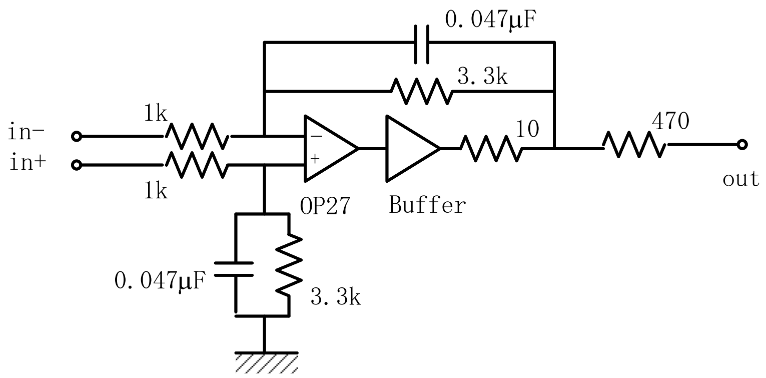

Figure B.1: *Wideband (1kHz) coil driver, which is used for the cavity locking servo. Two of the four coils for one mirror are sequentially connected and driven by one driver.*

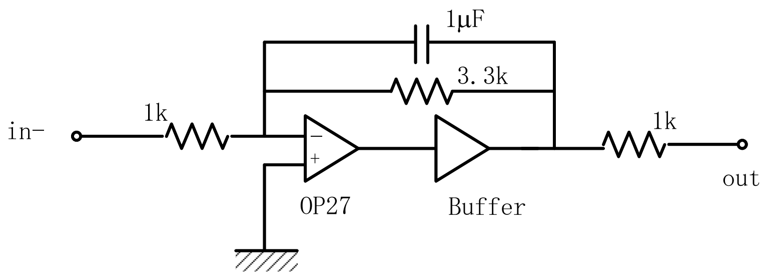

Figure B.2: *Narrowband (48Hz) coil driver, which is used for the DC control of the cavity for the frequency stabilization. Two of the four coils for one mirror are sequentially connected and driven by one driver.*

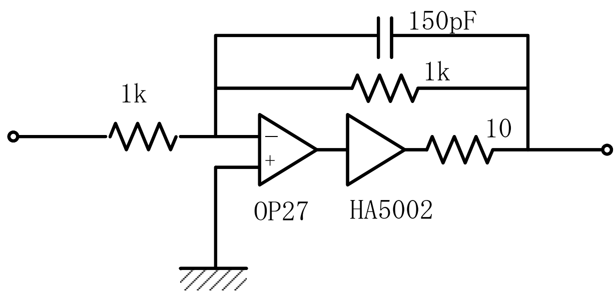

Figure B.3: *PZT driver for controlling the frequency of the laser.*

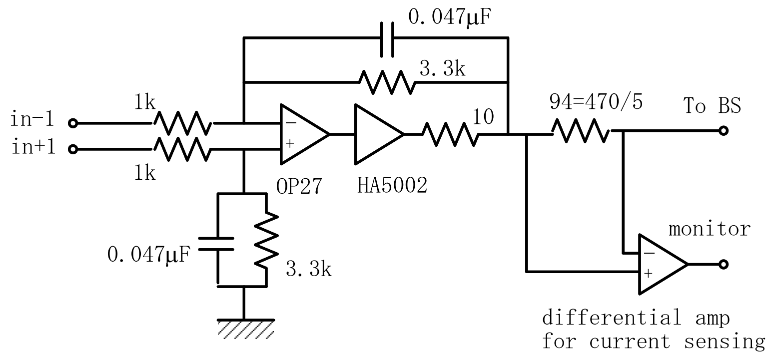

Figure B.4: *Coil driver for the beam splitter-control. Two of the four coils for BS are parallel-connected to one driver. For monitoring the feedback current, the voltage of the small resistance was used.*

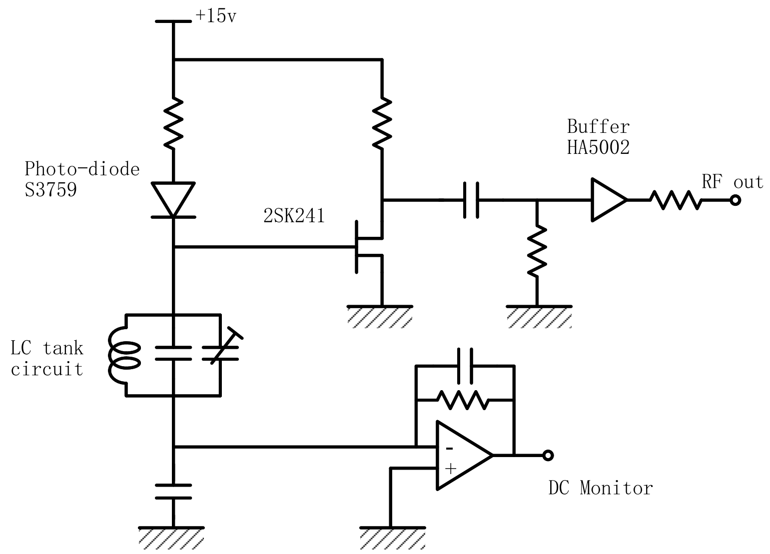

Figure B.5: *RF photo detector to detect the picked-off light from the arm cavities. This detector was used for the Pound-Drever-Hall detection of the cavity deviation from the resonance.*

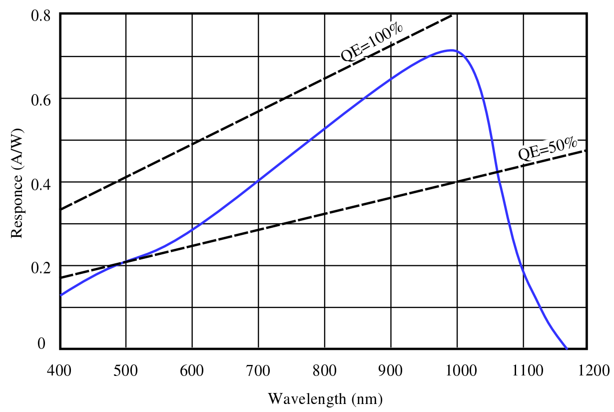

Figure B.6: *Response of the photo diode (S3759, Hamamatsu Photonics) used in the RF detector versus the wavelength. This plot is from the spec sheet of Hamamatsu Photonics.*

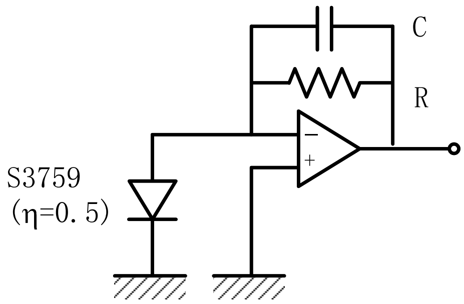

Figure B.7: *DC photo detector to detect the Michelson fringe. The feedback resistance R was 1.5kΩ and 2.19kΩ for PD1 and PD2, respectively.*

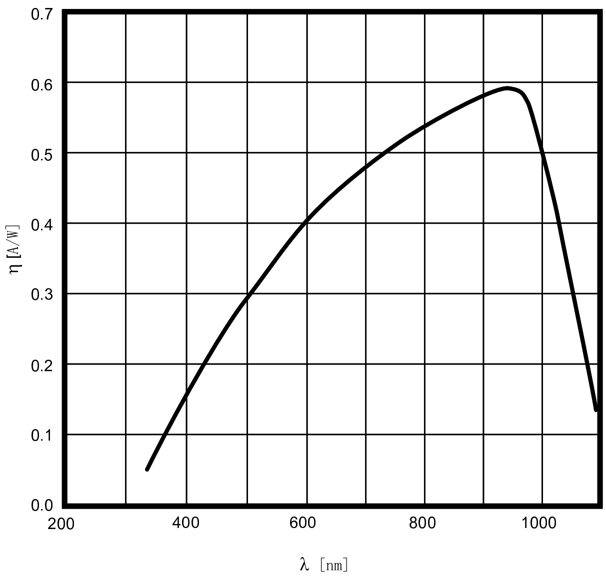

Figure B.8: *Efficiency of the photo diode (S1223-01, Hamamatsu) used in the DC detector versus the wavelength. This plot is from the spec sheet of Hamamatsu Photonics.*

References

1. R. A. Hulse and J. H. Taylor, Astrophys. J. **195** (1975) 51.

2. J. H. Taylor and J. M. Weisberg, Astrophys. J. **253** (1982) 908.

3. J. H. Taylor and J. M. Weisberg, Astrophys. J. **345** (1989) 434.

4. J. H. Taylor, A. Wolszczan, T. Damour, and J. M. Weisberg, Nature **355** (1992) 132.

5. T. Damour and J. H. Taylor, Phys. Rev. D **45** (1992) 1840.

6. Kip S. Thorne, in: Proc. Snowmass 94 Summer Study on Particle and Nuclear Astrophysics and Cosmology, (World Scientific, 1995) pp. 160–184.

7. R. Weiss, Quarterly Progress Report of the Research Laboratory of Electronics of the Massachusetts Institute of Technology **105** (1972) 54.

8. R. L. Forward, Phys. Rev. D **17** (1978) 379.

9. A. Abramovici, W. E. Althouse, R. W. P. Drever, Y. Gürsel, S. Kawamura, F. J. Raab, D. Shoemaker, L. Sievers, R. E. Spero, K. S. Thorne, R. E. Vogt, R. Weiss, S. E. Whitcomb and M. E. Zucker, Science **256** (1992) 325.

10. VIRGO the final conceptual design, unpublished (1992).

11. K. Danzmann, H. Lück, A. Rüdiger, R. Schilling, M. Schrempel, W. Winkler, J. Hough, G. P. Newton, N. A. Robertson, H. Ward, A. M. Campbell, J. E. Logan, D. I. Robertson, K. A. Strain, J. R. J. Bennett, V. Kose, M. Kühne, B. F. Schutz, D. Nicholson, J. Shuttleworth, H. Welling, P. Aufmuth, R. Rinkleff, A. Tünnermann, B. Willke, MPQ-Report **190**, 1994.

12. K. Tsubono, in: Proc. 1st Edoardo Amaldi Conference on Gravitational wave experiments, Frascati, Italy, June 1994 (World Scientific, 1995) pp. 112–114.

13. K. Kuroda *et al.*, in: Proc. International Conference on Gravitational waves: Sources and Detectors, Casina(Pisa), Italy, 1996 (World Scientific, Singapore, 1997) p100.

14. K. Tsubono and the TAMA collaboration, in: Proc. TAMA International Workshop on Gravitational Wave Detection, Saitama, Japan, 1996 (Universal Academy Press, 1997) pp. 183–191.

15. T. Nakamura, M. Sasaki, T. Tanaka, and K. S. Thorn, Astrophys. J. **487** (1997) 139.

16. K. Kawabe, S. Nagataki, M. Ando, K. Tochikubo, N. Mio and K. Tsubono, "Demonstration of a recombined Fabry-Perot-Michelson interferometer with suspended mirrors", App. Phys. B **62** (1996) 135–138.

17. Gravitational radiation, eds. N. Deruelle and T. Piran (North-Holland, Amsterdam, 1983).

18. A. Giazotto, Phys. Rep. **182** (1989) 365.

19. The detection of gravitational waves, ed. D. G. Blair (Cambridge University Press, Cambridge, 1991)

20. Juryoku-ha Antenna Gijutu Kentou-sho (in Japanese) (重力波アンテナ技術検討書–干渉計ハンドブック–), eds. M. Ohashi and N. Mio, (an internal document of the Japanese gravitational wave research group, 1992).

21. C. W. Misner, K. S. Thorne, and J. A. Wheeler, Gravitation (W. H. Freeman and Company, New York, 1973)

22. A. Siegman, LASERS (University Science Books, California, 1986).

23. R. W. P. Drever, in: Gravitational radiation, eds. N. Deruelle and T. Piran (North-Holland, Amsterdam, 1983) pp. 321–338.

24. D. Shoemaker, P. Fritschel, J. Giaime, N. Christensen and R. Weiss, Appl. Opt. **30** (1991) 3133.

25. P. Fritschel, D. Shoemaker and R. Weiss, Appl. Opt. **31** (1992) 1412.

26. A. Abramovici, W. Althouse, J. Camp, D. Durance, J. A. Giaime, A. Gillespie, S. Kawamura, A. Kuhnert, T. Lyons, F. J. Raab, R. L. Savage Jr., D. Shoemaker, L. Sievers, R. Spero, R. Vogt, R. Weiss, S. Whitcomb, M. Zucker, Phys. Lett. A **218** (1996) 157.

27. K. Tsubono, A. Araya, K. Kawabe, S. Moriwaki and N. Mio, Rev. Sci. Instrum. **64** (1993) 2237.

28. R. W. P. Drever, J. L. Hall, F. V. Kowalski, J. Hough, G. M. Ford, A. J. Munley and H. Ward, Appl. Phys. B **31** (1983) 97.

29. D. Shoemaker, R. Schilling, L. Schnupp, W. Winkler, K. Maischberger and A. Rüdiger, "Noise behavior of the Garching 30-m prototype gravitational-wave detector", Phys. Rev. D **38** (1988) 423–432.

30. A. Araya, K. Kawabe, T. Sato, N. Mio and K. Tsubono, "Highly sensitive wide-band seismometer using a laser interferometer", Rev. Sci. Instrum. **64** (1993) 1337.

31. S. Moriguchi *et al.* , Suugaku Koushiki III (in Japanese) (数学公式 III) (Iwanami, Tokyo, Japan 1969).

32. H. Kogelnik and T. Li, Proc. IEEE **54** (1966)1312.

33. J.Y. Vinet, VIRGO internal report PJT00 (1993).

34. M. W. Regehr, F. J. Raab, S. E. Whitcomb, Opt. Lett. **20** (1995) 1507.

35. A. Rüdiger, R. Schilling, L. Schnupp, W. Winkler, H. Billing, and K. Maischberger, Opt. Acta **28** (1981) 641–658.

36. D. Z. Anderson, Appl. Opt. **23** (1984) 2944–2949.

37. E. Morrison, B. J. Meers, D. I. Robertson, and H. Ward, Appl. Opt. **33** (1994) 5041–5049.

38. Y. Hefetz, N. Mavalvala, and D. Sigg, J. Opt. Soc. Am. B **14** (1997) 1597–1604.

39. N. M. Sampas and D. Z. Anderson, “Stabilization of Laser Beam Alignment to an Optical Resonator by Heterodyne Detection of Off-Axis Modes”, Appl. Opt. **29** (1990) 394–403.

40. K. Tochikubo, Master-Thesis, University of Tokyo(1996)

41. H. Billing, K. Maischberger, A. Rüdiger, R. Schilling, L. Schnupp and W. Winkler, J. Phys. E: Sci. Instrum. **12** (1979) 1043.

42. C. N. Man, D. Shoemaker, M. Pham Tu and D. Dewey, Phys. Lett. A **148** (1990) 8.

43. M. Ando, Master-Thesis, University of Tokyo(1996)

44. M. Ando, Ying Li, K. Kawabe, and K. Tsubono, in: Proc. TAMA International Workshop on Gravitational Wave Detection, Saitama, Japan, 1996 (Universal Academy Press, 1997) pp. 341–344.

45. M. Ando, K. Kawabe, and K. Tsubono, Phys. Lett. A **237** (1997) 13.

46. M. Ando, K. Arai, K. Kawabe, and K. Tsubono, “Demonstration of power recycling on a Fabry-Perot-type prototype gravitational wave detector”, Phys. Lett. A **248** (1998) 145.

47. K. Tochikubo, A. Sasaki, K. Kawabe, and K. Tsubono, in: Proc. TAMA International Workshop on Gravitational Wave Detection, Saitama, Japan, 1996 (Universal Academy Press, 1997) pp. 365–367.

48. K. Kawabe, in: Juryoku-ha wo Toraeru (in Japanese) (重力波をとらえる, 京大出版会, 京都, 1998), eds. T. Nakamura, N. Mio and M. Ohashi (Kyoto University Press, 1998) pp. 248–286.

49. K. Kawabe and the TAMA collaboration, in: Proc. TAMA International Workshop on Gravitational Wave Detection, Saitama, Japan, 1996 (Universal Academy Press, 1997) pp. 249–257.

Acknowledgements

First of all, I am indebted to Professor K. Tsubono for supporting the experiments and patiently encouraging me for years to write this thesis. Without his persistent support, this paper would not have been appear.

I am grateful to all the members of the TAMA project. I had many stimulating discussions with Professor S. Kawamura, Dr. A. Araya, S. Moriwaki and other people. Though those discussions are not reflected by this paper from the superficial point of view, they were helpful for me to develop the physical insight into many aspects of the interferometers. Especially I am grateful to Dr. M. Ohashi for interesting discussions while I was doing the experiments and for some practical advice while I was writing the thesis.

I am also grateful to A. Rüdiger for useful advice on the physics, and for improving the English presentations throughout this paper.

I must acknowledge the assistance in the experiments from M. Ando and K. Tochikubo. It is my pleasure to see that both of them are now taking important roles in the development of the TAMA300 detector.

I would like to thank to my parents for encouraging me to continue my study (私の研究を応援してくれた両親に感謝します). I also would like to express my greatest thanks to my family, Keiko and Hinako, for always supporting my study (最後に、私の研究生活を支えてくれた妻 桂子と娘 日菜子に対して、深く感謝します).